Quantitative Computational and Experimental Characterization of Functionalized Nanoparticles

Yung-Chen Wang

A dissertation

submitted in partial fulfillment of the

requirements for the degree of

Doctor of Philosophy

University of Washington

2017

Reading Committee:

David G. Castner, Chair

Donald R. Baer

Lara J. Gamble

Program Authorized to Offer Degree:

Department of Bioengineering

University of Washington

Abstract

Quantitative Computational and Experimental Characterization of Functionalized Nanoparticles

Yung-Chen Wang

Chair of the Supervisory Committee:
David G. Castner
Department of Bioengineering

Nanoparticles are widely used in many fields of science and can often be found in everyday commercial products. This widespread use of nanoparticles in our daily lives and the industry have raised several concerns regarding the safety and environmental impact of these nanoparticles. In the biomedical field, understanding how nanoparticles interact with the biological environment is crucial for public safety and advancing the development of nanomedicine. In this work, both computational and experimental methods were developed to aid the surface chemical characterization of functionalized nanoparticles.

The major experimental project focuses on controlling and probing the orientation of immobilized proteins on gold nanoparticles. Protein G B1, a protein that will selectively bind to the Fc region of IgG, was immobilized onto gold NPs (AuNPs) functionalized with oligo(ethylene glycol)-Maleimide (OEG-MEG) self-assembled monolayers (SAMs). The orientation of the protein can be controlled via a site-specific

maleimide-sulfhydryl reaction between the OEG-MEG SAMs and the cysteine amino acid in the protein. Utilizing site-specific chemistry and surface sensitive analysis techniques of X-ray photoelectron spectroscopy (XPS) and time-of-flight secondary ion mass spectrometry (ToF-SIMS), it was possible to both control and determine the orientation of immobilized Protein G B1on gold nanoparticles.

In addition to experimental analysis, robust computer simulations using the Simulation of Electron Spectra for Surface Analysis (SESSA) program were incorporated to aid the characterization of a wide variety of nanoparticles. It was demonstrated that SESSA can accurately simulate XPS spectra and peak intensities of nanoparticles and verify existing methods of calculating overlayer thickness of core-shell nanoparticles. Further, SESSA can be applied to assess the structure and thickness of various SAMs on both flat and nanoparticle surfaces by incorporating experimentally collected XPS and sum-frequency generation (SFG) results.

In another study, SESSA was applied to model citrate stabilized Au/Ag-core/shell nanoparticles with complex geometrical properties. The Au/Ag-core/shell NPs were polydispersed in size, non-spherical, and contained off-centered Au-cores. The NPs were characterized using XPS and scanning transmission electron microscopy (STEM) to determine the composition and morphology of the NPs. Simulating NPs with average dimensions and not accounting for the geometrical properties of the NPs resulted in significant underestimation of the gold intensity. Simulations based on the combined effect of NP non-sphericity and off-centered Au-core resulted in reduced effective Ag-shell thickness and provided simulated elemental compositions that matched the experimental XPS results.

TABLE OF CONTENTS

List of Figures xi

List of Tables xvi

Chapter 1. INTRODUCTION 1

1.1 GENERAL OVERVIEW 1

1.2 OBJECTIVE 3

Chapter 2. MATERIALS AND METHODS 7

2.1 SURFACE FUNCTIONALIZATION AND PROTEIN IMMOBILIZATION 7

2.1.1 SILICON SUBSTRATE PREPARATION 7

2.1.2 SELF-ASSEMBLED MONOLAYERS BASED SURFACE MODIFICATION 8

2.1.3 GOLD SUBSTRATE PREPARATION 9

2.1.4 SURFACE MODIFICATION OF FLAT GOLD SUBSTRATES 10

2.1.5 PROTEIN SYNTHESIS 11

2.2 GOLD NANOPARTICLE SYNTHESIS AND PROTEIN IMMOBILIZATION ... 12

2.2.1 GOLD NANOPARTICLE SYNTHESIS 12

2.2.2 SURFACE MODIFICATION OF GOLD NANOPARTICLES 14

2.2.3 PROTEIN IMMOBILIZATION ON GOLD NANOPARTICLES 15

2.3 EXPERIMENTAL CHARACTERIZATION TECHNIQUES 16

2.3.1 TRANSMISSION ELECTRON MICROSCOPY (TEM) 16

2.3.2 X-RAY PHOTOELECTRON SPECTRASCOPY (XPS) 17

2.3.3 TIME OF FLIGHT-SECONDARY ION MASS SPECTROMETRY 20

2.4 COMPUTATIONAL CHARACTERIZATION TECHNIQUES 22

2.4.1 SIMULATION OF ELECTRON SPECTRA FOR SURFACE ANALYSIS (SESSA) 22

2.4.2 PARTIAL INTENSITY AND MONTE CARLO CALCULATION IN SESSA 22

2.4.3 SESSA SIMULATION SETUP 25

2.4.4 PYTHON SCRIPT FOR SESSA SIMULATION AUTOMATION 26

Chapter 3. CONTROLLING AND PROBING THE ORIENTATION OF IMMOBILIZED PROTEIN G B1 MUTANTS VIA SITE SPECIFIC COVALENT ATTACHMENT TO OLIGO(ETHYLENE GLYCOL) FUNCTIONALIZED GOLD NANOPARTICLES 36

3.1 ABSTRACT 37

3.2 INTRODUCTION 38

3.3 MATERIALS AND METHODS 40

3.3.1 SUBSTRATE PREPARATION 40

3.3.2 PROTEIN SYNTHESIS 40

3.3.3 NANOPARTICLE SYNTHESIS AND SURFACE FUNCTIONALIZATION 41

3.3.4 PROTEIN IMMOBILIZATION ON GOLD NANOPARTICLES 41

3.3.5 TRANSMISSION ELECTRON MICROSCOPY 42

3.3.6 X-RAY PHOTOELECTRON SPECTROSCOPY 43

3.3.7 TIME OF FLIGHT-SECONDARY ION MASS SPECTROMETRY (TOF-SIMS) 43

3.4 RESULTS AND DISCUSSIONS 43

3.4.1 TEM ANALYSIS 43

3.4.2 XPS ANALYSIS OF NANOPARTICLE FUNCTIONALIZATION AND PROTEIN IMMOBILIZATION 44

3.4.3 TOF-SIMS PEAK RATIO ANALYSIS TO DETERMINE PROTEIN ORIENTATION 47

3.5 CONCLUSION 50

3.6 ACKNOWLEDGEMENT 51

Chapter 4. EVALUATING THE INTERNAL STRUCTURE OF CORE–SHELL NANOPARTICLES USING X-RAY PHOTOELECTRON INTENSITIES AND SIMULATED SPECTRA 52

4.1 ABSTRACT 53

4.2 INTRODUCTION 54

4.3 MATERIALS AND METHODS 56

4.3.1 SESSA 56

4.3.2 SHARD'S T (NP) FORMULA 58

4.3.3 EVALUATION OF THE T (NP) FORMULA 60

4.4 RESULTS AND DISCUSSIONS 61

4.4.1 EVALUATION OF THE T (NP) FORMULA 61

4.4.2 APPLICATION OF SESSA TO EXPERIMENTAL XPS DATA 65

4.4.3 SIMULATIONS OF SAMS WITH SESSA 2.0 66

4.4.4 FULL SPECTRAL COMPARISION BETWEEN SESSA AND EXPERIMENT 70

4.5 CONCLUSION 74

4.6 ACKNOWLEDGEMENT 75

Chapter 5. SIMULATION OF SELF-ASSEMBLED MONOLAYERS OF DODECANE-, CARBOXYLIC ACID-, AND CARBOXYLIC ACID TERMINATED OLIGO(ETHYLENE GLYCOL)- THIOLS ON FLAT AND NANOPARTICLE SURFACES 76

5.1 ABSTRACT 77

5.2 INTRODUCTION 78

5.3 MATERIALS AND METHODS 79

5.3.1 SUBSTRATE PREPARATION 79

5.3.2 FLAT GOLD SURFACE FUNCTIONALIZATION 80

5.3.3 NANOPARTICLE SYNTHESIS AND FUNCTIONALIZATION 81

5.3.4 SIMULATION OF ELECTRON SPECTRA FOR SURFACE ANALYSIS 82

5.3.5 TRANSMISSION ELECTRON MICROSCOPY 83

5.3.6 X-RAY PHOTOELECTRON SPECTROSCOPY 84

5.3.7 ATOMIC FORCE MICROSCOPY 84

5.3.8 SUM FREQUENCY GENERATION 85

5.4 RESULTS AND DISCUSSIONS 86

5.4.1 TEM ANALYSIS 86

5.4.2 AFM CHARACTERIZATION OF THE FLAT GOLD SUBSTRATE 87

5.4.3 SFG CHARACTERIZATION OF FUNCTIONALIZED FLAT GOLD 88

5.4.4 XPS CHARACTERIZATION OF FUNCTIONALIZED FLAT GOLD AND GOLD NANOPARTICLES 89

5.4.5 SESSA SIMULATION OF FUNCTIONALIZED FLAT GOLD SURFACES

93

5.4.6 SESSA SIMULATION OF FUNCTIONALIZED GOLD NANOPARTICLES 99

5.5 CONCLUSION 102

5.6 ACKNOWLEDGEMENT 103

Chapter 6. QUANTIFYING THE IMPACT OF NANOPARTICLE COATINGS AND NON-UNIFORMITIES ON XPS ANALYSIS: GOLD/SILVER CORE-SHELL NANOPARTICLES 104

6.1 ABSTRACT 105

6.2 INTRODUCTION 106

6.3 MATERIALS AND METHODS 108

6.3.1 MATERIALS 108

6.3.2 SCANNING TRASMISSION ELECTRON MICROSCOPY (STEM) 109

6.3.3 X-RAY PHOTOELECTRON SPECTROSCOPY (XPS) 109

6.3.4 SIMULATION OF ELECTRON SPECTRA FOR SURFACE ANALYSIS (SESSA) SIMULATION OF AU/AG-CORE SHELL NPS 110

6.4 RESULTS AND DISCUSSIONS 111

6.4.1 NANOPARTICLE CHARACTERIZATION 111

6.4.2 XPS ANALYSIS 113

6.4.3 SESSA SIMULATIONS 114

6.5 CONCLUSION 120

6.6 ACKNOWLEDGEMENT 121

Chapter 7. CONCLUSIONS AND FUTURE WORK 123

7.1 CONCLUSIONS 123

7.2 FUTURE DIRECTION 124

APPENDIX 126

APPENDIX A. USE OF XPS TO QUANTIFY THICKNESS OF COATINGS ON NANOPARTICLES 127

Appendix A.1 ABSTRACT 128

APPENDIX B. VERSAILLES PROJECT ON ADVANCED MATERIALS AND STANDARDS INTERLABORATORY STUDY ON MEASURING THE THICKNESS AND CHEMISTRY OF NANOPARTICLE COATINGS USING XPS AND LEIS 129

Appendix B.1 ABSTRACT 131

APPENDIX C. A TECHNIQUE FOR CALCULATION OF SHELL THICKNESSES FOR CORE-SHELL-SHELL NANOPARTICLES FROM XPS DATA 132

Appendix C.1 ABSTRACT 133

APPENDIX D. PYTHON SCRIPT FOR SESSA SIMULATION AUTOMATION 134

Appendix D.1 BACKGROUND 134

Appendix D.2 APPROACH 135

Appendix D.3 SCRIPT FOR GENERATING SESSION FILES 136

Appendix D.4 SCRIPT FOR SESSA AUTOMATION AND CAPTURING RESULTS 141

REFERENCES 144

LIST OF FIGURES

Figure 2.1. (a) Structure of the WT Protein G B1. The black spheres highlight the relative location of the amino acid C- and N-terminus. The color assignment is based on the secondary structure of the protein. (b) In addition to the showing the structure of the Protein G B1, the location of the cysteine point mutations are highlighted (red: T11C, green: E42C, yellow: T49C, blue: V21C, brown: D36C.) 12

Figure 3.1. (a) and (b) shows TEM bright field images of AuNPs synthesized using the citrate reduction method. The distribution of nanoparticle diameter is shown in (c). It was determined using ImageJ's particle analysis algorithm that the AuNPs had were mostly monodispersed and had an average diameter of 12.9 ± 0.9nm. (d) The ratio of major-axis and minor-axis of the AuNPs were calculated to determine their sphericity. The average AuNPs were overall spherical with a major-axis to minor axis ratio of 1.1. 44

Figure 3.2. Comparison of secondary ion peak ratios of reacted (C4H2NO2S-, m/z 127.98) and unreacted (C4H2NO2-, m/z 96.01) maleimide rings. 47

Figure 3.3. (a) Amino acids that are asymmetrically distributed in Protein G B1 are highlighted. The amino acids are selected based on their relative distribution: asparagine (Asn) and leucine/isoleucine (Leu/Ile) near the C-terminus, methionine (Met) and tyrosine (Tyr) near the N-terminus, and phenylalanine (Phe) and tryptophan (Trp) near the center of Protein G B1. (b) The location of the cysteine point mutations are highlighted (red: T11C, green: E42C, yellow: T49C, blue: V21C, brown: D36C.) Figure produced using Visual Molecular Dynamics (VMD).. 48

Figure 3.4. Overview comparison of ToF-SIMS amino acid peak ratios from different regions of the protein. V21C and T49C mutants are categorized as N-terminus side mutants as they are physically closer to the N-terminus end while T11C and E42C are categorized as C-terminus side mutants as they are closer physically closer to the C-terminus end. (a) Ratio of the sum of C-terminus amino acid peaks (Asn, Leu

and Ile) to the N-terminus amino acid peaks (Met and Tyr) for the Protein G B1 cysteine mutants. (b) Ratio of the sum of center amino acid peaks (Phe and Trp) to the C-terminus amino acid peaks. (c) Ratio of the sum of center amino acid peaks (Phe and Trp) to the N-terminus amino acid peaks. *p < 0.05..... 49

Figure 4.1. To scale representation of the four CS systems used for the evaluation of the T(NP) formula. The definitions of the core radius R and the shell thickness T are displayed in the bottom left corner. The actual size depends on the chosen shell material as all dimensions are given in units of L1,a, the attenuation length of shell photoelectrons within the shell. For both model systems, the values of L1,a are listed at the bottom. In all four cases I−IV, the shell thickness T is depicted with a constant thickness of $5L_{1,a}$, while the simulations were conducted for values ranging from $0.1L_{1,a}$ to $5L_{1,a}$. The core radii for cases I−IV are, respectively: I: R =$32L_{1,a}$; II: R =$8L_{1,a}$; III: R = $L_{1,a}$; IV: R = $0.5L_{1,a}$..... 62

Figure 4.2. T_{NP} plotted against T_{SESSA} for the Be/Au and the Pd/Al2O3 NP systems of Figure 4.1. T_{NP} was calculated according to eq 4.2 using the normalized intensity ratio ASESSA obtained from a simulation conducted with the shell thickness TSESSA. Every red dot corresponds to a simulation at a different shell thickness, ranging from $0.1L_{1,a}$ to $5L_{1,a}$. For each material system, the plots on the left side were conducted with the SLA, whereas the plots on the right side depict simulations with elastic scattering. The roman numerals correspond to the numerals in Figure 4.1 63

Figure 4.3. Comparison of normalized intensities of the C 1s, Au 4f, O 1s, and S 2p peaks determined by XPS and simulations conducted for different CH_2 shell thicknesses and the presence and absence of a hydrocarbon surface contamination with SESSA 2.0 68

Figure 4.4. Contributions to the sum-of-squares difference for each case depicted in Figure 4.3 and the total sum-of-squares difference $\sum X^2$..... 70

Figure 4.5. Experimental, simulated, and transmission-corrected spectra of $C_{16}COOH$ SAMs on 14 nm gold NPs at an emission angle of 0° relative to the surface normal and the resultant approximation of the transmission function. (a) Comparison of

experimental and simulated spectra, both normalized to the C 1s peak. Since SESSA does not account for the transmission function of the experimental setup, the spectra do not match. (b) Comparison of the transmission-corrected experimental spectrum and the simulated spectrum. By fitting a second-degree polynomial to the transmission function and dividing the experimental spectrum by this function, very good agreement is obtained with the experimental spectrum. (c) Display of the transmission function obtained by comparing elemental compositions together with the second-order polynomial fit for the binding-energy range between −800 and −150 eV and by dividing the experimental spectrum by the simulated spectrum. 72

Figure 4.6. Comparison of transmission-corrected, experimental data for SAMs on flat gold and SAMs on gold NPs with the corresponding simulations. Also, the simulated spectrum of a single gold NP is shown. The clear difference in background shapes between the flat geometry and the NP is apparent. In contrast, the single gold NP model correctly predicts the peak-intensity ratio but exhibits a significantly different background shape. The subfigures (a), (b), and (c) are schematic representations of the simulated morphologies: (a) Powder-like arrangement of CS particles; (b) a SAM layer located on a gold substrate; (c) a single CS nanoparticle on an infinite substrate. 73

Figure 5.1. (a) and (b) shows TEM bright field images of AuNPs synthesized using the citrate reduction method. The distribution of nanoparticle diameter is shown in (c). It was determined using ImageJ's particle analysis algorithm that the AuNPs had were mostly monodispersed and had an average diameter of 12.9 ± 0.9nm. (d) The ratio of major-axis and minor-axis of the AuNPs were calculated to determine their sphericity. The average AuNPs were overall spherical with a major-axis to minor axis ratio of 1.1. 86

Figure 5.2. Representative AFM image of flat gold substrates used for SAMs functionalization in this study. The gold substrates had an average height of 2.05 nm and an average surface area of 1.0061 μm2 in an analysis area of 1.0 μm X 1.0 μm. 87

Figure 5.3. Comparison of SFG C-H region spectra of the dodecanethiol (C11), COOH, and OEG-COOH SAMs. 88
Figure 5.4. ARXPS high-resolution C1s analysis of OEG-COOH SAM functionalized flat gold surfaces with sample tilted at angles of 0°, 60°, and 75.5°. To quantify the chemical states of the carbon species in the SAMs, the high-resolution C1s spectra was fit with C-C/C-H at 284.5 eV, C-O at 286.1 eV, and O-C=O at 288.1 eV. The quantified concentrations of the carbon species are provided. 92
Figure 5.5. (a) The molecular structure of the OEG-COOH thiol. (b) A SESSA model of the OEG-SAMs with well-defined layer by layer structure with no intermixing between each layer. (c) A SESSA model that describes a potential structure of the OEG-COOH SAMs with the COOH headgroup intermixing with the OEG chains. 97
Figure 6.1. (a & b) STEM images of Au/Ag-core/shell nanoparticles. (c) Distribution of Au/Ag-core/shell nanoparticle diameter with a bin width of 1 nm and a mean diameter of 20.5 ± 2.4 nm (n = 76 particles). (d) Distribution of Au-core Ag shell nanoparticle major-axis/minor-axis ratio with a bin width of 0.05 and a mean ratio of 1.14 ± 0.1 (n = 76 particles). 111
Figure 6.2. Cross sectional schematic of an average, ideal Au/Ag core/shell nanoparticle. The mean for the measured Au-core diameter and Ag-shell thickness was 7.4 ± 0.9 nm and 6.4 ± 2.3 nm (52 particles), respectively. Whole particle diameter derived from the manually measured mean core diameter and shell thickness (20.2 nm) matches closely to the whole particle diameter measured using ImageJ's particle analysis algorithm (20.5 ± 2.4 nm). Figure not to scale. . 112
Figure 6.3. Comparison of experimental XPS result and SESSA simulation of the composition for Au/Ag-core/shell nanoparticles with varying sodium citrate thickness ranging from 0.6 nm to 1.0 nm for the one-wash (a) and two-wash (b) samples. The sum root mean square deviation (ΣRMSD) indicates the simulated elemental composition (%) for all elements compared to the experimental XPS result. 115

Figure 6.4. (a) STEM images of Au/Ag-core/shell nanoparticles containing non-centered cores as highlighted by red arrows. (b) Distribution of the distance of gold core off-center relative to the whole Au/Ag-core/shell nanoparticle with bin width of 1 nm and mean distance of 2.2 ± 1.3 nm (n = 70 particles). 117
Figure 6.5. Comparison of experimental XPS and SESSA simulated Au atomic % for varying Ag-shell thicknesses and Au-core diameters. The apparent ΔAg-shell thickness and ΔAu-core thickness are relative to the average particle dimensions. (a) One centrifuge wash. (b) Two centrifuge wash. The red dot on both panels indicates the average dimensions of the Au-core and Ag-shell determined by STEM. 118
Figure 6.6. Schematic illustration of the Ag-shell thickness normalization using: (a) the experimentally measured Ag-shell thickness distribution from STEM analysis, (b) only the non-circularity of the Au/Ag-core shell NPs and assuming the Au-core is located in the center of the particle, and (c) only the degree of off-centered for the Au-core while assuming the particle is perfectly circular. 119
Figure 6.7. Comparison of experimental XPS results and SESSA simulations for the (a) one-wash and (b) two-wash Au/Ag-core/shell NPs based on the average STEM dimension, circularity normalized, off-centered Au-core normalized, and the STEM Ag-shell normalized Ag-shell distribution. By including the impacts of both non-circularity and off center cores based on the STEM distributions, the model matches the experimental data and the off-centered cores were found to have the greatest impact. 120
Figure D.1. Excel template for generating SESSA session files for layered nanoparticles. It is possible to define various common parameters such as layer composition, thickness, density, and instrumentation parameters. If the user wishes to generate multiple files by varying the thickness and density information of certain layers, user can simply set the upper and lower boundary for those layers.136

LIST OF TABLES

Table 2.1. Summary and abbreviation of alkanethiols 10
Table 2.2. Abbreviation of the five cysteine mutants 11
Table 3.1. Abbreviation of the five cysteine mutants 41
Table 3.2. XPS elemental composition of unfunctionalized, OEG-MEG functionalized, and immobilized Protein G B1 WT, T11C, V21C, D36C, E42C, andT49C on AuNPs. The process of the OEG-MEG functionalization and protein immobilization can be determined by monitoring the N 1s signal and the attenuation of the Au 4f signal. (n.d. = not detected) 46
Table 4.1. Minimum and maximum diameters of the Be/Au and Pd/Al_2O_3 CS NPs for each core radius, according to figure 1. The minimum and maximum values depend on the shell thickness, which ranged from $0.1L_{1,a}$ to $5L_{1,a}$ 61
Table 4.2. Normalized Intensities of the C 1s, Au 4f, O 1s, and S 2p Peaks Determined by XPS Measurements and Simulations with SESSA 1.3[110] and SESSA 2.0 with and without a Surface Hydrocarbon Contamination Layer for an Emission Angle of 0° Relative to the Surface Normal. 69
Table 5.1. Summary and abbreviation of alkanethiols 80
Table 5.2. XPS elemental composition of SAMs functionalized flat gold and AuNPs by the axis of the analyzer lens along with surface normal of the Si wafer substrate. The dodecanethiol functionalized AuNPs were not analyzed due to difficulties during sample preparation. (n.d. = not detected) 90
Table 5.3. Comparison of experimental XPS result and SESSA simulation of dodecanethiol functionalized flat gold surface with varying amount of hydrocarbon contamination. The sum root mean square deviation (ΣRMSD) value indicates the simulated elemental composition (%) for all elements compared to the experimental XPS result. 94
Table 5.4. Comparison of experimental XPS result and SESSA simulation of COOH thiol functionalized flat gold surface with varying amount of hydrocarbon

contamination. The ΣRMSD value indicates the simulated elemental composition (%) for all elements compared to the experimental XPS result. 95
Table 5.5. ΣRMSD value of between the experimental XPS result and SESSA simulation of COOH thiol functionalized flat gold surface by varying both the density of the SAMs and the thickness of the hydrocarbon contamination layer. The ΣRMSD value indicates the simulated elemental composition (%) for all elements compared to the experimental XPS result. 96
Table 5.6. ΣRMSD value of between the layer by layer model simulated by SESSA and the experimental XPS result of OEG-COOH SAMs on flat gold. The thickness of hydrocarbon contamination layer and the density of the OEG layer was adjusted to fit the SESSA model to the experimental result. The literature density of the OEG layer (~ 1.20E23) is highlighted. 98
Table 5.7. ΣRMSD value of between the intermixing model simulated by SESSA and the experimental XPS result of OEG-COOH SAMs on flat gold. The OEG layer and the COOH layer are intermixed. The estimated density of the mixed OEG layer (1.15E23) is highlighted. 99
Table 5.8. SESSA simulated result of COOH SAMs functionalized AuNPs using either the packing density of SAMs on flat gold surfaces and a model of 70% SAMs packing density. The thickness of hydrocarbon layer was varied to probe potential contamination. 100
Table 5.9. ΣRMSD value of between the layer by layer model simulated by SESSA and the experimental XPS result of OEG-COOH SAMs on AuNPs. The thickness of hydrocarbon contamination layer and the density of the OEG layer was adjusted to fit the SESSA model to the experimental result. The literature density of the OEG layer (~ 1.20E23) is highlighted. 102
Table 5.10.SESSA simulated result of OEG-COOH SAMs functionalized AuNPs using either the packing density of SAMs on flat gold surfaces and a model of 70% SAMs packing density. The thickness of hydrocarbon layer was varied to probe potential contamination. 102

Table 6.1. XPS determined atomic composition of Au/Ag core-shell nanoparticles deposited onto silicon wafer substrates. Average values and standard deviations are reported for six replicate analyses of the one- and two-wash samples. Only one analysis is reported for the no-wash sample (see text for details). 114

ACKNOWLEDGEMENTS

I would like to first thank my advisor and committee chair, Prof. David Castner, for his amazing mentorship. Thank you for supporting and providing the resources for my graduate study. Your passion and positive attitude for research meant a lot for me and kept me motivated.

I would like to thank my dissertation committee, which consists of Prof. David Castner, Dr. Donald Baer, Prof. Lara Gamble, Prof. Buddy Ratner, and Prof. Charlie Campbell. Thank you for your guidance and support.

I would like to thank the entire NESAC/BIO group for being such great colleagues. I want to thank all the staff members of NESAC/BIO, specifically Dr. Daniel Graham and Gerry Hammer for their training and advising on ToF-SIMS and XPS instruments. I want to thank the post-doctoral researchers, Dr. Ali Rafati, Dr. Julia Kokesch-Himmelreich, and Dr. Adam Taylor for their advice and support. I want to thank the outstanding graduate students in the group, including Dr. Blake Bluestein, Dr. Elisa Harrison, Michael Newton for their friendship and assistance. It was an honor and pleasure working with all of you.

I want to thank the many collaborators at NIST, NPL, PNNL, and TU Wien. Specifically, I want to thank Maksymilian Chudzicki for his patience and support on the SESSA software.

I also want to thank my good friends Dr. Blake Bluestein, Bob Lamm, Jason Stevens, Jonathan Tsui, and Dr. David Younger. Thank you for always being there when I'm in need and all the wonderful memories. I don't say this enough but I'm lucky and grateful to have you all as my friend.

Last and most importantly, I want to thank my family for their unconditional love and support. It is obvious but I still want to say it. I would have never gone this far without you all.

This work was supported by NSF GRFP (DGE-1256082) and NESAC/BIO (NIH P41 EB002027).

Chapter 1. INTRODUCTION

1.1 GENERAL OVERVIEW

The field of nanotechnology has been a major focus of the scientific community and has become integrated into our daily lives. The capability of manipulating structures and molecules at the nanoscale has enabled the rapid development in both the microelectronics industry and biomedical science. One major contribution of nanotechnology in the biomedical science is the development of nanoparticles. In general, nanoparticles are defined as particles with a diameter ranging from 1 to 100 nm. One obvious advantage of particles in the nanometer regime is the potential application of utilizing their small size to deliver drugs to previously hard to reach regions of the body, such as passing through the blood-brain barrier.[1] Additional advantages of nanoparticle based delivery include prolonged circulation time, controlled-release, and site-specific drug delivery.[2] For instance, inert and non-toxic gold nanoparticles are often used for applications such as diagnostic tools or drug delivery vehicles.[3,4] Both metallic and organic polymeric nanoparticles have been successfully applied in various clinically approved applications, including vaccinations, cancer therapies, and treatments of infectious diseases.[5] Aside from their clinical applications, an extensive study published by the Woodrow Wilson International Center in 2015 listed thousands of everyday products such as cosmetics, clothing, and sunscreens that also contain engineered nanoparticles.[6] The widespread use of nanoparticles in our daily lives and the industry also raised several concerns regarding the safe and ethical use of these nanoparticles. As the use of many engineered nanoparticles is still in its infancy, the United States Environmental Protection Agency (EPA) suggests that the long term biological and environmental impacts of these nanoparticles must be carefully studied and monitored.[7]

Nonetheless, the development of nanoparticle applications in the biomedical field has been fruitful. The various commercial products available for the treatments of cancer and diagnostic devices continue to grow. However, compared to the vast amount of literature on potential therapeutic or diagnostic use of nanoparticles for

medicine, products that can reach the state of safe and effective use are very limited. Nanoparticles, due to their small size and high reactivity, are prone to contamination or losing their functional properties. It is not uncommon to find contradicting results in the literature on in vivo and in vitro nanoparticle toxicity, highlighting the inability to reproduce previous results.[8,9] The properties of the nanoparticle can be altered through the various stages of synthesis, functionalization, storage, and handling. Often, slight changes in the properties of the nanoparticles can only be identified with highly sophisticated instruments that a regular research lab might not have access to.[10] For instance, methods that can provide quantitative information of the biomolecular interface of nanoparticles, such as the thickness and composition of surface coatings are scarce or not easily accessible. Current available technologies often involve expensive biochemical assays and can only provide qualitative information.[11] Hence, there is increasing concerns about the underreporting and the lack of detailed characterization of nanoparticles for biomedical applications.[12]

To understand nanoparticle behavior in a biological environment, one must carefully characterize the properties of the nanoparticle. Basic physical properties such as the size, shape, and surface charge all play important roles in the biological response of the nanoparticles.[13,14] Conventional techniques such as transmission electron microscopy (TEM), scanning electron microscopy (SEM), atomic force microscopy (AFM), and dynamic light scattering (DLS) can all be applied to determine the size and shape distribution of nanoparticles.[15] The surface charge of the particle can be readily measured with the well-established zeta potential measurement through Laser Doppler electrophoresis.[16]

The surface, rather than the bulk of the nanoparticle, will dictate the biological responses such as circulation time, immunogenic response, and toxicity. Upon the introduction of nanoparticles into blood and tissues, proteins will adsorb immediately onto the surface of the nanoparticle, forming a protein corona.[17] The surface chemical and physical properties of the nanoparticle will often dictate the type and amount of adsorbed proteins. The body's immune system and cells will now no longer "see" the nanoparticle, but rather the protein corona adsorbed onto the nanoparticles. The composition of the protein corona plays critical role in determining the circulation time

and the method of clearance of these nanoparticles.[17] Moreover, it is rare to introduce nanoparticles directly without some form of surface modification. To achieve the diagnostic or therapeutic goal, nanoparticles are often engineered to carry drugs or recognition components for target-specific nanoparticle delivery. Compounds such as monoclonal antibodies,[18] small molecules,[19] and sugars[20] have been designed and immobilized onto the surface of nanoparticles to achieve targeted drug delivery and reducing off-target side effects. The coverage and density of the immobilized or functionalized compounds needs to be carefully characterized as they directly impact the efficacy of the nanoparticle. Naturally, the addition of these compounds or drugs can also affect the formation of protein corona on the nanoparticle. Therefore, researchers must carefully control and characterize these surface modifications.

A recent review by Baer et al. discussed the wide variety of methods available for gathering surface chemical information from nanomaterials and nanoparticles.[10] For example, to determine the surface chemical composition of the nanoparticles, techniques such as X-ray photoelectron spectroscopy (XPS) and time-of-flight secondary ion mass spectrometry (ToF-SIMS) can provide surface-sensitive information about the composition of the nanoparticles. Other techniques commonly used to characterize nanomaterials include Fourier transform infrared spectroscopy (FTIR), Raman spectroscopy, and nuclear magnetic resonance (NMR). Although these techniques can provide useful information about the bulk composition and identify the presence of functional groups, they lack the sensitivity to identify the surface properties of nanomaterials.

1.2 OBJECTIVE

The overall objective of this work is to develop versatile methods for the surface chemical analysis of nanoparticles. This work aims to utilize a multi-technique characterization approach to systematically characterize a variety of nanoparticle systems and provide solutions to challenging problems such as overlayer thickness calculations and protein immobilization techniques. Aside from experimental analysis, robust computer simulations using the Simulation of Electron Spectra for Surface Analysis (SESSA) program were incorporated to aid the characterization of

nanoparticles. From simple model systems of self-assembled monolayer functionalized gold nanoparticles to complex biomolecule immobilizations, this work will provide the field with a greater understanding of protein-nanoparticle interactions and methods of quantitative nanoparticle characterizations using surface analysis techniques and computer simulations.

Specific Aim 1: Controlling and probing the orientation of immobilized Protein G B1 mutants via site specific covalent attachment onto oligo(ethylene glycol) functionalized gold nanoparticles.

Hypothesis: It is possible to control the orientation of immobilized Protein G B1 mutants on gold nanoparticles and determine the orientation of immobilized protein.

Approach: Protein G B1 was covalently immobilized onto gold nanoparticles via functionalized alkanethiol based self-assembled monolayer (SAMs). The orientation of the protein was controlled by introducing a site-specific amino acid mutant into the protein. Utilizing the surface sensitivity and the limited sampling depth of ToF-SIMS, the orientation of the immobilized Protein G was determined by the unique secondary ion signal originating from the amino acids at opposite ends of the protein.

Specific Aim 2: Evaluating the internal structure of core–shell nanoparticles using X-ray photoelectron intensities and simulated spectra.[21] (J. Phys. Chem. C, 2015. **119**, 17687-17696.)

Hypothesis: SESSA Version 2.0 can be used to directly and accurately simulate XPS spectra and peak intensities of nanoparticles and verify existing methods of calculating overlayer thickness of core-shell nanoparticles.

Approach: A general-purpose geometry package PENEGEOM was incorporated into SESSA Version 2.0 for direct simulation of multi-layered nanoparticles using user defined parameters. Accurate XPS intensity and spectra can be obtained by correcting the simulated result using the transmission function of the XPS instrument used to analyze the experimental spectra.

Specific Aim 3: Simulation of self-assembled monolayers of dodecane-, carboxylic acid-, and carboxylic acid terminated oligo(ethylene glycol)- thiols on flat and nanoparticle surfaces.

Hypothesis: SESSA can be used to generate accurate models of various SAMs on both flat and nanoparticle surfaces by incorporating experimentally collected XPS results.

Approach: An accurate model of the each SAMs can be computed with SESSA by combining experimental XPS peak intensities and experimentally characterized structural information in the literature. Variables such as the thickness of adventitious carbon and structure of each sub-layer of the SAMs can then be determined by matching the simulated and experimental result.

Specific Aim 4: Quantifying the Impact of Nanoparticle Coatings and Non-uniformities on XPS Analysis: Gold/silver Core-shell Nanoparticles.[22] (Anal. Chem, 2016. **88**, 3917-3925)

Hypothesis: In combination with experimental analysis, SESSA can be used to model multi-layer nanoparticles with complex geometrical properties.

Approach: SESSA was applied to model citrate stabilized Au/Ag-core/shell nanoparticles. A quantitative model of the Au/Ag-core/shell nanoparticles was built in SESSA based on experimental XPS and scanning transmission electron microscopy (STEM) measurements. The impact of the non-spherical nanoparticles and off-centered Au-core can be corrected by using quantitiative STEM measurements and intensity normalization.

Appendix: The appendix discusses three other published collaborative works related the characterization of nanoparticles. In addition, the script written in Python for the automation of SESSA simulation is discussed (appendix D). Below is the overview of the other published studies:

Appendix A: Use of XPS to Quantify Thickness of Coatings on Nanoparticles.

This study discusses methods of calculating overlayer coating thickness on nanoparticles by combining XPS results with TEM or other measurements of size. For full text, see ref.[23].

Appendix B: Versailles Project on Advanced Materials and Standards Interlaboratory Study on Measuring the Thickness and Chemistry of Nanoparticle Coatings Using XPS and LEIS.

This study discusses a large scale interlaboratory project aimed to study the measurement of shell thickness and chemistry of nanoparticle coatings using different XPS and LEIS instruments. For full text, see ref.[24].

Appendix C: A technique for calculation of shell thicknesses for core-shell-shell nanoparticles from XPS data.

This study discusses a method of calculating shell thicknesses for core-shell-shell nanoparticles using XPS data without the need of numerical simulation or advanced knowledge. For full text, see ref.[25].

Chapter 2. MATERIALS AND METHODS

CHAPTER OVERVIEW

This section of the thesis will provide information about the materials and reagents used in the following chapters. In addition, the fundamental theory and background behind the major analytical instruments along with the experimental conditions will also be provided. This section aims to provide a detailed background and rational for the experimental protocol for those who are interested in repeating the experiments. Note that not all of the instrumentation parameters in the following chapters will be mentioned. Some of those characterizations experiments took place in other laboratories and the details of the instrumentations will be provided in the appropriate chapters.

2.1 SURFACE FUNCTIONALIZATION AND PROTEIN IMMOBILIZATION

2.1.1 SILICON SUBSTRATE PREPARATION

Silicon (Si) substrates were used as the base layer for gold substrate preparation and sample preparation for gold nanoparticles (AuNPs) analyzed in ultra-high vacuum instruments.

For both applications, silicon substrates were prepared from standard 100mm diameter Si wafers (Silicon Valley Microelectronics, Santa Clara, CA), with a thickness of 525 +/- 25 um. The Si wafers were diced into 1.1 cm^2 squares using the Disco DAD 321 Wafer Dicing Saw in the Washington Nanofabrication Facility (WNF). The diced Si wafers then undergoes a cleaning protocol which consists of an overnight wash in filtered and deionized water (18.2 MΩ) (EMD Millipore, Billerica, MA), followed by two 15-minutes washes in methylene chloride, two 15-minutes washes in acetone, and two 15-minutes washes in methanol. The solvent washes were performed under constant sonication to

ensure the removal of residual contaminates that were deposited onto the Si wafer during the dicing process. The cleaned Si wafers were then placed in a dedicated wafer holder, sealed with foil and stored under air at room temperature.

2.1.2 SELF-ASSEMBLED MONOLAYERS BASED SURFACE MODIFICATION

Gold served as the substrate for self-assembled monolayers (SAMs) functionalization and protein immobilization chemistries. The SAMs used in this thesis work are all alkanethiols based, which contain a long hydrophobic alkane chain terminated with a thiol group. The thiol chemisorbs to the gold surface and in combination with the van der Waals interactions of the hydrocarbon chains results in the formation of a stable monolayer structure over the gold surface. Though researchers have been taking advantage of these strong thiol-sulfur interactions for many decades, the exact mechanism on the atomic structure of the interface wasn't unraveled till recently.[26] Experimental and theoretical evidence concludes that the strong covalent interaction at the gold-sulfur interface requires the formation of a deprotonated sulfhydryl group (thiyl radical RS•). The mechanism holds true for gold nanoparticles if we assume a crystallographic model, in which gold nanocrystal's surface is composed of (111) and (100) facets.[27] These facets can be treated as locally flat surfaces that will behave very similarly to an actual flat surface. Though the gold-sulfur interaction remains similar, the complication arises when one considers how the assembly of SAMs will be affected by multifaceted surfaces which expose crystalline edges and corner sites. Though dependent on the chain length of the alkanethiol, early experimental investigations have shown that SAMs on gold nanoparticles are at least as ordered as SAMs on flat surfaces.[28–30] A more recent scanning tunneling microscopy (STM) investigation on the ligand packing of alkanethiols concluded that the SAMs adopts a slightly relaxed formation (reduced density) to

compensate for the high-energy defects and particle curvature while retaining order.[31]

For the past 40 years, SAMs have attracted considerable interest for surface modifications for a few reasons: First, they are easy to prepare. A typical SAMs can form well-defined, consistent layer within minutes to hours.[32,33] Second, by manipulating the functional headgroup of the SAMs, it is possible to readily modify surfaces such as gold (thiol) or silicon (silane). Third, SAM functionalized surfaces can serve as a well-defined building block to attach additional molecules to the surface.[34–36] These properties enables SAMs to serve as a great way to control surface chemistries for a wide variety of applications such as sensing, catalysis, and surface modifications.[37]

In chapter 3, SAMs are used to both stabilize AuNPs in solution and serve as a functional building block for protein immobilization. In another study, spectral simulation models based on a series of alkanethiol SAMs with different functional headgroups were constructed to investigate the structural properties of the SAMs on both flat gold surfaces and AuNPs.

2.1.3 GOLD SUBSTRATE PREPARATION

Compared to AuNPs, the protocol for surface functionalization, modification, and protein immobilization of flat gold surfaces is considerably easier and was therefore used to verify surface chemistries prior to nanoparticle based experiments. Gold substrates were prepared from the diced and cleaned Si substrates discussed in the previous section. A 5 nm titanium (Ti) adhesion layer followed by a 30 nm Au layer was deposited on top of the Si substrates using the electron beam vapor deposition technique. The Ti adhesion layer improves the bonding between the Au overlayer and the Si substrate, enhancing the physical stability of the gold layer. The deposition was conducted in the WNF using the CHA Industries EVAP (Fremont, CA). The Ti and Au layers were deposited using deposition rates of 2.0 Å and 5.0 Å per second respectively. The

rate and thickness of the metal deposition process were optimized to ensure an even and smooth coverage of the Au layer. The deposition process was monitored by a quartz crystal microbalance within the deposition chamber. After deposition, the Au substrates were backfilled with nitrogen gas, sealed, and stored away from light exposure.

2.1.4 SURFACE MODIFICATION OF FLAT GOLD SUBSTRATES

As discussed earlier, alkanethiol based SAMs were used to functionalize the flat gold substrates in this study. A summary of the alkanethiols used in this dissertation and the abbreviation used to describe them is provided in Table 2.1. Both the dodecanethiol and COOH thiol were purchased from Asemblon (Seattle, WA). Both the OEG-COOH thiol and OEG-MEG thiol were purchased from Prochimia (Sopot, Poland).

A 20mL glass scintillation vial was rinsed with pure 200 proof (Decon Laboratories, King of Prussia, PA) and then dried in air. The gold substrate was placed inside the cleaned scintillation vial and submerged in ~3mL with either 1mM (OEG-MEG thiol) or 100uM (all other thiols) solution of the target alkanethiol in pure ethanol. The glass vial was then backfilled with nitrogen, sealed, and stored away from light for 36 hours to allow the self-assembly process to go to completion. After self-assembly, the gold substrate was removed, rinsed with ethanol for 15 seconds and then dried using nitrogen gas.

Table 2.1. Summary and abbreviation of alkanethiols

Chemical structure	**Alkanethiol abbreviation**
HS-C11-CH3	dodecanethiol
HS-C11-COOH	COOH thiol
HS-C11-EG4-O-CH2-COOH	OEG-COOH thiol
OH-(EG)6-C11-S-S-C11-(EG)6-OCH2-CONH-Maleimide	OEG-MEG disulfide

2.1.5 PROTEIN SYNTHESIS

Protein G is a multi-domain protein that can bind to the Fc portion of a variety of mammalian immunoglobulin G (IgG) species, leaving the Fab sites available for antigen binding.[38,39] The IgG binding domain of Protein G, Protein G B1, is a 56 amino acid protein that can form a unique folded structure without disulfide cross-links or tight ligand binding.[40] Protein G B1 is well-characterized[41–45] and has been shown to be stable in the vacuum environment when immobilized.[46–48] Therefore, it was chosen as the target protein for studying controlled immobilization on surfaces.

The key covalent chemistry used in this study to achieve controlled protein immobilization is the maleimide-sulfhydryl reaction. The native Protein G B1 wild type (WT) does not contain a free sulfur group (cysteine) for the maleimide reaction. However, a cysteine point mutation can be introduced to achieve the specific maleimide-cysteine coupling between the surface and the protein. Our lab has previously investigated the maleimide-cysteine based protein immobilization chemistries on flat gold substrates extensively.[46,48]

Table 2.2. Abbreviation of the five cysteine mutants

Wild type amino acid	**Location**	**Cysteine mutant abbreviation**
Threonine	11	T11C
Valine	21	V21C
Asparatic-acid	36	D36C
Glutamic-acid	42	E42C
Threonine	49	T49C

All wild type (WT) and cysteine mutant protein G B1 samples used in this study were synthesized by the Institute for Protein Design at the University of Washington. A total of five cysteine mutants were investigated in this study (Table 2.2). The structure of Protein G B1 WT and the relative location of the cysteine mutants is shown in Figure 2.1. The locations of the cysteine mutants

were strategically chosen based on the location, synthesis condition, and predicted binding site of protein G B1 to the IgG antibody. Note that mutants are located near or on the loops between secondary structures in order to main the structural integrity of the protein (Figure 2.1.b). Further, the mutants were distributed around the protein to enable a range of orientation control.

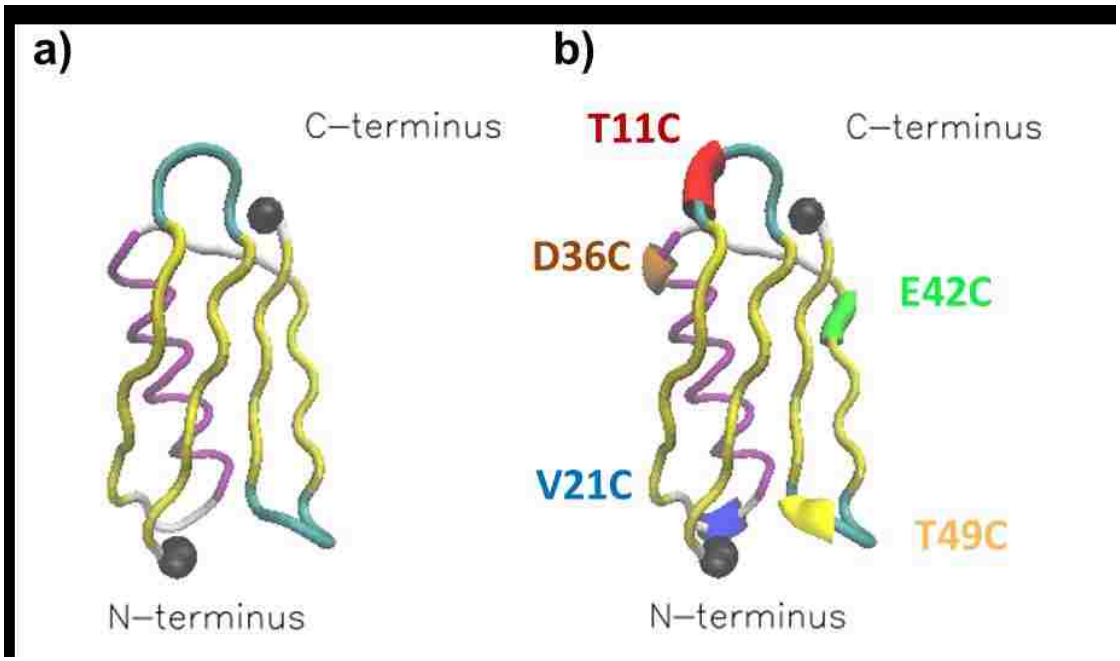

Figure 2.1. (a) Structure of the WT Protein G B1. The black spheres highlight the relative location of the amino acid C- and N-terminus. The color assignment is based on the secondary structure of the protein. (b) In addition to the showing the structure of the Protein G B1, the location of the cysteine point mutations are highlighted (red: T11C, green: E42C, yellow: T49C, blue: V21C, brown: D36C.)

2.2 GOLD NANOPARTICLE SYNTHESIS AND PROTEIN IMMOBILIZATION

2.2.1 GOLD NANOPARTICLE SYNTHESIS

The AuNPs were synthesized using the citrate reduction method, which was first proposed by Turkevich et al.[49] and further developed by Frens.[50] The citrate reduction method gained its popularity as it can rapidly synthesize AuNPs ranging in size from 10 to 120 nm and uses non-toxic reagents to produce biocompatible sodium citrate-stabilized AuNPs using only basic laboratory

equipment. 14nm and 40nm diameter AuNPs were synthesized and used for most experiments related to AuNPs in this thesis work. In general, the size of the AuNP can be tuned by adjusting the ratio of the reducing agent (sodium citrate) and the gold salt. Extensive literature review can be found in regards to the mechanism of the citrate reduction based AuNP synthesis.[51,52]

Prior to the synthesis of AuNPs, the glassware must undergo aqua regia cleaning. Aqua regia is a 1:3 molar ratio mixture of nitric acid and hydrochloric acid. The goal of the aqua regia cleaning is to remove potential residual gold on the glassware from the previous synthesis. Due to the hazardous nature of strong acids, one must take proper precautions and wear appropriate personal protective equipment before handling aqua regia.

Often, a large volume of AuNPs were synthesized at a time (up to 1 liter). Required glassware includes round bottom flask and a reflux condenser system. Reagents used includes sodium citrate tribasic dehydrate (Sigma-Aldrich, St. Louis, MO) and gold (III) chloride hydrate (99.999%) (Sigma-Aldrich, St. Louis, MO). For synthesizing 1 liter of AuNPs, first prepare 0.01% (w/v) of Au solution (i.e. 100mg of gold chloride dissolved in 1 liter of DI H_2O). Transfer the Au solution to the round bottom flask and heat to 100°C while stirring under the reflux system. While the Au solution is heating, prepare the sodium citrate stock by dissolving 285mg of sodium citrate in 25mL of DI H_2O (40mM). As the temperature of the Au solution reaches 100°C, the sodium citrate solution is quickly added into the round bottom flask. The amount of sodium citrate added will depend on the desired size of the AuNPs. For 13nm AuNPs, add a 2.5% volume of the gold solution (25mL of the sodium citrate stock). For 40nm AuNPs, add a 1% volume of the gold solution (10mL of the sodium citrate stock). It is crucial to add the sodium citrate solution as fast as possible and directly into the gold solution to ensure monodispersed growth of the AuNPs. After adding the sodium citrate solution, maintain the temperature at 100°C for 20 minutes. The gold solution should quickly change color from transparent to dark red or light

purple within minutes of the sodium citrate addition. After 20 minutes, the AuNP solution is removed from the reflux system. Let the AuNP solution sit at room temperature to cool, followed by nitrogen gas backfill. The AuNPs can then be sealed, foiled, and stored in the refrigerator at 4°C.

2.2.2 SURFACE MODIFICATION OF GOLD NANOPARTICLES

The protocol for alkanethiol based SAMs surface modification of AuNPs is similar to the process of modifying flat gold substrates, with the addition of several purifications steps. Unlike flat gold films, AuNPs take considerably more effort to handle as they are suspended in solution rather than a film attached to a bulk substrate.

In this work, AuNPs were functionalized with the SAMs described in Table 2.1. For consistency, AuNPs were functionalized with the same concentration of thiol throughout the study unless otherwise mentioned (100uM).

To prepare thiol functionalized AuNPs, the desired amount of AuNPs prepared from the previous section was first transferred to a glass container. Thiols dissolved in pure ethanol were then added to a AuNP solution to achieve the final concentration of 100uM. Under stirring, the AuNP containing glassware was sealed and foiled to prevent exposure from light, then left to assemble for 36 hours. After 36 hours, the thiol functionalized AuNPs were sonicated for 30 seconds and subsequently transferred into centrifuge tubes. To purify the AuNPs and remove excess thiols from the AuNP solution, the AuNPs were subjected to centrifugation at 9,000 rpm for 30 minutes. The pellet of the concentrated AuNPs in the bottom of the centrifuge tube was collected, followed by another round of 9,000 rpm centrifugation for 30 minutes on the supernatant solution to collect the remaining AuNPs. To break up the AuNP pellet before each resuspension, the pellet was vortexed for 30 seconds and sonicated for 1 minute. The collected concentrated AuNPs were then transferred to small 1.5mL Eppendorf tubes and re-suspended with 1mL of DI H_2O. These AuNPs were then centrifuged at 12,000

rpm for 40 minutes. The supernatant was carefully removed and fresh 1mL of DI H_2O was added to re-suspend the AuNPs. The AuNPs were vortexed for 30 seconds and centrifuged again for 12,000 rpm at 40 minutes. After removing the supernatant and backfilling with nitrogen gas, and the concentrated AuNPs were ready for further chemical modifications or analysis.

2.2.3 PROTEIN IMMOBILIZATION ON GOLD NANOPARTICLES

As discussed earlier, maleimide-sulfhydryl immobilization chemistry is based on the bonding of the maleimide group with free sulfur groups. AuNPs functionalized with OEG-MEG SAMs can react with cysteine mutants of Protein G B1. Protein G B1 WT does not contain a cysteine amino acid, but a cysteine mutant version of the Protein G B1 can be selectively introduced to achieve site-specific maleimide-cysteine coupling.

The PEG-MEG functionalized AuNPs were incubated with 1mg/mL of a Protein G B1-cysteine mutant in PBS overnight at room temperature on a shaker shaking at 200 rpm. To remove excess proteins in solution or proteins that are loosely bound to the surface of AuNPs, a series of purification protocols is required. After the overnight incubation with protein, the AuNPs were purified using three rounds of 12,000 rpm/40 minutes centrifugation-resuspension cycles using PBS. To break up the AuNP pellet before each resuspension, the pellet was vortexed for 30 seconds and sonicated for 1 minute. After the third rinsing cycle, the AuNP solution was transferred to a 1000kDa dialysis tube (SpectrumLabs, Rancho Dominquez, CA). The 1000kD molecular weight cut-off dialysis tubing was chosen for purification as it is common to use molecular weight cut-off tubing that is more than 100 times larger than the target molecule (Protein G B1 WT and its mutants all have molecular weights of ~6kDa).

Dialysis against DI H_2O was performed for two 2-hour rinse cycles and one overnight rinse under constant stirring. After the overnight dialysis, the AuNP solution was retrieved and purified by centrifugation using 12,000 rpm for 40

minutes. After removing the supernatant and backfilling with nitrogen gas, and the concentrated AuNPs were ready for further chemical modifications or analysis.

2.3 EXPERIMENTAL CHARACTERIZATION TECHNIQUES

2.3.1 TRANSMISSION ELECTRON MICROSCOPY (TEM)

TEM is a part of the electron microscopy family and is commonly used for characterizing the morphology of nanomaterials. Electron microscopy, in contrast to conventional light microscopy, utilizes electrons to provide illumination and the generation of visual images of small samples. Due to the short wavelength of electrons, images produced by electron microscope can easily reach nanometer resolution, making them an ideal tool for analyzing nanomaterials.[53] TEM, as the name implies, captures the electrons transmitted through the sample to generate images. In general, TEM captures the contrast of the sample, which is caused by the differences in the composition and thickness of the sample. High-resolution TEM images are ideal for the characterization of AuNPs in this thesis work as they can provide information about the size and shape of the nanoparticles. The images captured using TEM were analyzed using ImageJ's (National Institutes of Health, USA) Particle Analysis algorithm. In ImageJ, a threshold was first applied to the TEM brightfield image to remove background noise, leaving a binary image containing only the nanoparticles and background. Classic watershed was then applied to the image to separate nanoparticles that are adjacent to each other. This process prevents the Particle Analysis algorithm from counting multiple nanoparticles in a close proximity as one nanoparticle. Lastly, the Particle Analysis algorithm was applied to determine the size and circularity of each nanoparticle. Notably, aggregated nanoparticles were removed manually from the analysis region.

TEM analysis was conducted using the Tecnai G2 F20 TEM (FEI, Hillsboro, Oregon) at the University of Washington Molecular Analysis Facility (MAF). Brightfield images of the AuNPs were taken at magnifications between X180k-X245k using a 200kV electron source.

The AuNP sample for the TEM analysis was prepared by drying AuNPs directly onto a carbon-supported TEM grid (Ted Pella, Redding, CA). First, a slightly concentrated AuNP solution was produced by centrifuging 1.5mL of AuNPs under 12,000 rpm for 20 minutes. After removing the supernatant, the AuNPs were resuspended using 0.5mL mixture of 50:50 ethanol and DI H_2O. Ethanol solution was used to accelerate the drying process to prevent particle aggregation. The AuNP mixture was then sonicated for five minutes to ensure the AuNPs are finely dispersed to prevent aggregation as they dry on the TEM grid. A fresh TEM grid was placed on a foil followed by depositing 1uL of the AuNP mixture onto the center of the TEM grid. After 1uL solution of the AuNP dried on the TEM grid, this process was repeated ten times to ensure a good coverage of AuNPs on the TEM grid. While waiting for the AuNP to dry between each deposition, the AuNP solution was placed into the sonicator to prevent particle aggregation.

2.3.2 X-RAY PHOTOELECTRON SPECTRASCOPY (XPS)

XPS is a quantitative surface analysis technique that can provide information about the sample's elemental composition and chemical states. XPS can identify all elements of a sample except for hydrogen and helium with a sensitivity of 0.1 atomic %. The ability for XPS to differentiate between elements is based on the photo-electric effect that was established by Albert Einstein,[54] for which he was awarded the 1921 Noble Prize in Physics. The photoelectric effect describes one of the many interactions between light and matter. When a light source with sufficient energy strikes an atom, the energy from the light is absorbed and the energy can be dissipated through the ejection of core or

valence electrons of the atom (photoelectrons). As the energy of the light source (often X-ray) is known and the kinetic energy of the ejected photoelectrons can be measured, one can readily calculate the binding energy of that specific photoelectron before it was released. This relationship can be described in the following basic XPS equation:

$$BE = hv - KE \qquad (2.1)$$

Here, BE stands for binding energy, hv is the energy of the photon (h = Planck constant and v = frequency of incident light), and KE is the kinetic energy of the photoelectron. The binding energies are elemental specific and can be affected by the local environment of the sample such as chemical bonds and degree of oxidation. Calculating the binding energy of the photoelectrons thus provide information of the sample's elemental composition and chemical states. Note that this basic XPS equation does not account for the work function, which is the energy required for the electron to escape into the vacuum level from the Fermi level, and the charge compensation with insulating samples from the electron flood gun. Even though X-rays can penetrate deeply into the sample (ums), the photoelectrons generated through typically X-ray excitation (i.e., Al and Mg Kα x-rays) can only travel around 5 - 10nm without losing energy.[55] In other words, XPS analysis will only capture the photoelectrons emerging from the top 10nm of the sample, making it a surface sensitive technique. For characterizing nanoparticles, XPS can provide crucial information about the overlayer of the NPs due to its sampling depth.

The XPS analysis mentioned in this thesis work were done using three different instruments, including the Surface Science Instrument S-Probe (Mountain View, CA), Kratos AXIS Ultra DLD (Kratos, Manchester, England), and the PHI Quantera (Physical Electronics, Chanhassen, MN).

The S-probe was used for studying SAMs functionalized flat gold surfaces, AuNPs and also protein immobilized AuNPs. The S-probe is equipped with a monochromatized Al Kα X-ray source (*hv* = 1486.6eV). The nominal

photoelectron take-off angle was 0˚ (the angle between the substrate surface normal and the axis of the analyzer). For each set of sample, spectra were collected from three different regions of 800 μm X 800 μm spot size, including a survey scan from 0-1100 eV (4 scans, 0.4eV step size). For AuNPs functionalized with alkanethiol SAMs, detailed S 2p (32 scans, 0.4eV step size) and high-resolution C 1s (16 scans, 0.2eV resolution) and Au 4f (4 scans, 0.2eV step size) scans were also collected. When nitrogen species such as the maleimide group of a SAMs or proteins are present on the sample, detailed N 1s scans are also collected (15 scans, 0.4eV step size). The pass energy for the survey and detail scans was 150 eV. For quantitative XPS analysis, the HAWK Data Analysis software (Service Physics, Bend, OR) was used to determine the elemental composition by manually selecting the peaks using a linear background subtraction method. The peak areas were quantified using the relative sensitivity factors provided by the instrument manufacturer. The wide scans were carefully screened to identify potential contaminants. For sample preparation, AuNPs were deposited onto clean Si substrates and let dry in vacuum desiccator. Usually 35uL of the AuNP solution was deposited at a time until a confluent layer is formed on the Si wafer to prevent the signal from the Si substrate being detected during the XPS analysis.

The Kratos Ultra DLD was used for studying peptide coated AuNPs in Appendix B. Similar to the S-probe, the Kratos XPS is equipped with a monochromatized Al Kα X-ray source. The hybrid mode was used for analysis where photoelectrons are collected from a wide range of take-off angles. This approach increases the detected signal for quantitative analysis. The nominal photoelectron take-off angle was 0˚. For each set of sample, spectra were collected from three different regions of 300 μm X 700 μm spot size. The survey scans were taken between 0-1200eV (1 scan, 1eV step size) followed high resolution S 2p (8 scans, 0.1eV step size), C 1s (8 scans, 0.1eV step size), and Au 4f (1 scan, 0.1 eV step size). The high-resolution C 1s spectra were collected

at 0.1 eV/Step for 32 scans with a dwell time of 300 ms and pass energy of 20eV. The peak areas were quantified using the relative sensitivity factors provided by the instrument manufacturer. The AuNP sample preparation for Kratos XPS analysis was identical to the sample preparations used for S-probe analysis.

The PHI Quantera was used to characterize Au/Ag core/shell nanoparticles in chapter 5. The characterization took place at the Pacific Northwest National Laboratory (PNNL). The detailed instrumentation parameters and the sample preparations are described in chapter 5.

2.3.3 TIME OF FLIGHT-SECONDARY ION MASS SPECTROMETRY

Time of flight-secondary ion mass spectrometry (ToF-SIMS) is a label-free and highly sensitive mass spectrometry technique often used in the field of surface analysis. ToF-SIMS utilizes the bombardment of high energy primary ions to sputter away surface molecules of a sample. Secondary ions generated through the impact of primary ions are analyzed with a time-of-flight analyzer to determine their mass. Similar to other mass spectrometry techniques, the composition of the sample can be determined by analyzing the ejected molecular ions or fragmented secondary ions. The sampling depth of static SIMS is limited to the uppermost ~2 nm which makes it a surface sensitive technique.[56] It is important to note that most ejected molecules or atoms from the surface are neutral, and only the charged secondary ions are collected in SIMS analysis.[55] Compared to XPS analysis, SIMS is only a semi-quantitative technique as the generation of the secondary ions is highly dependent on the local environment and the type of primary ion used (known as the matrix effect). Quantification is further complicated by instrumentation drift and the lack of understanding in the mechanism of the ionization process.[57] However, quantification for two-component systems based on peak ratios are often possible with the proper understanding of the sample and the analysis techniques.[58] Further, the matrix

effect is typically not as pronounced in organic systems investigated in this work compared to inorganic systems.[59]

In this thesis work, ToF-SIMS serves as a way to verify the functionalization and chemical reactions on AuNPs. Further, the limited sampling depth of ToF-SIMS can be utilized to probe the orientation of immobilized proteins. Previous studies have thoroughly investigated the secondary ions generated by the natural amino acids and have identified the unique secondary ion peaks for each amino acid.[60,61] Therefore, it is possible to determine the orientation of immobilized protein by taking advantage of the asymmetrical distribution of amino acids in a protein. For example, if one side of a protein contains more lysine, one would expect a higher lysine amino acid signal when that side of the protein is facing towards the primary ion source. Point mutation or isotopic labeling can also be introduced to assist in identifying the orientation of the protein.[48]

A ToF-SIMS V-100 (Ion-ToF, Munster, Germany) instrument was used to characterize both functionalized AuNPs and protein immobilized AuNPs in chapter 3. For alkanethiol SAMs functionalized AuNP samples, the measurements were taken using 25keV Bi^+ primary ion source with a current of ~0.15pA under 45° incident angle. For AuNP containing immobilized proteins, the measurements were taken using the Bi^{3+} ion source. For each sample, five high mass resolution spectra were acquired from different 100 μm X 100 μm regions both polarities. For all acquisitions, the total ion dose was kept below the static limit (10^{12} ions/cm^2) to prevent extensive disruption of the surface layer which can introduce signal from the deep layer of the sample as well as damaged proteins and SAMs. For all samples, the mass resolution at m/z 27 (positive) and m/z 25 (negative) typically was around 5000 ($m/\Delta m$). The acquired data were analyzed using the Ion-ToF measurement explorer software. For positive spectra, the masses were mass calibrated using the CH_3^+, $C_2H_3^+$, and $C_3H_5^+$ secondary ions. For negative spectra, the masses were mass calibrated using the CH^-, OH^-, and

C_2H^- secondary ions. AuNP samples were analyzed by XPS prior to ToF-SIMS analysis using the same sample because XPS is considered a non-destructive technique for most sample types.[55]

2.4 COMPUTATIONAL CHARACTERIZATION TECHNIQUES

2.4.1 SIMULATION OF ELECTRON SPECTRA FOR SURFACE ANALYSIS (SESSA)

The National Institute of Standards and Technology (NIST) Database for the Simulation of Electron Spectra for Surface Analysis (SESSA) is a simulation software for generating XPS or Auger electron spectroscopy spectra.[62] A SESSA user can define customized sample geometries including flat layered films, islands, spheres, and layered spheres. For the case of XPS, the photoelectron spectrum is generated using a Monte Carlo (MC) algorithm while taking considerations into the specified experimental conditions.[63] The intensity of the photoelectrons is calculated by simulating a number of electron trajectories that mimic the physics of the electron transport. To improve the speed of simulation, the electron trajectories are simulated from the analyzer and traced back in reverse to the sample origin. Using this trajectory reversal method, only trajectories that will contribute to the intensity of that specific electron energy are simulated.[63] Instrumentation conditions such as the type of X-ray source and geometrical configuration of the source and analyzer can be readily adjusted. SESSA is also capable of simulations under conditions where elastic scattering of the electrons is neglected (i.e., the straight line approximation (SLA)).

2.4.2 PARTIAL INTENSITY AND MONTE CARLO CALCULATION IN SESSA

Here, a brief overview of how SESSA calculates X-ray photoelectron intensities through MC simulation is provided. Readers interested in the detailed

explanation and theory behind the calculation should referred to the manual and publication written by the SESSA developers.[62,63]

Before simulations begin in SESSA, the expert system retrieves all necessary parameters from databases based on the user's specifications. These specifications include parameters related to the sample composition, sample roughness (relative surface area), X-ray source, and detector. SESSA retrieves other appropriate parameters including inelastic mean free path (IMFP), elastic-scattering cross sections, photoionization cross sections, photoionization asymmetry parameters, photoelectron line shapes, chemical shifts information, etc.

The electron-solid interaction in SESSA is based on the partial intensity approach.[64,65] The term partial intensity is the number of electrons arriving at the detector after undergoing a given number of inelastic collisions *n* in the solid between the point of generation and escape from the sample surface. This trajectory reversal MC simulation process was achieved by simulating an infinitely small acceptance angle of the analyzer by employing a symmetry property of the Boltzmann kinetic equation.[66] Equation 2.1 describes equation for calculating the partial intensity $C_n(\vec{\Omega}_{i,}\vec{\Omega}_e)$ of electrons experiencing multiple elastic scattering events.

$$C_n(\vec{\Omega}_{i,}\vec{\Omega}_e) = DAFTN_a \int_{\Delta\Omega}\int_{4\pi}\int_0^{\infty} \phi_x(z,\vec{\Omega}_{i,}\vec{\Omega}_e)c_0(z) \times \phi_{e,n}(z,\vec{\Omega}_{x,}\vec{\Omega}_e)\, dz\, d\vec{\Omega}_x\, d\vec{\Omega}_e \qquad (2.2)$$

The terms *D, A, F, T,* and N_a denote for detector efficiency, area of analysis, flux of the source radiation, spectrometer transmission, and atomic density respectively. It is important to note that D, F, and T are assigned a value of 1 in the current version of SESSA. This, the user must account for such instrumental parameters such as the actual transmission function when comparing SESSA generated partial intensity values to the experimental results. The term $\Delta\Omega$ in the integral accounts for the solid angle of acceptance of the analyzer, which can be defined by the user. The term $\phi_x(z,\vec{\Omega}_{i,}\vec{\Omega}_e)$ accounts for

the excitation depth distribution function (at a depth of *z*). For XPS analysis, this term can be replaced by the photoionization cross section and taken outside of the depth integral. The term $c_0(z)$ denotes the atomic fraction of an element at a given depth *z*. The term $\phi_{e,n}(z,\vec{\Omega}_x,\vec{\Omega}_e)$ represents the emission depth distribution function, which is the probability for electron to escape from a given depth *z* after experiencing a given number *n* of inelastic collisions. The calculation is integrated over depth *z*, emission directions of the signal electrons during excitation $d\vec{\Omega}_x$ and emission directions after emission from the surface $d\vec{\Omega}_e$. Beyond equation 2.2, additional simplifying assumptions related to excitation depth distribution, emission depth distribution, and the angular dependence of the excitation depth is applied. The detailed discussion and rational behind these calculation is beyond the scope of this thesis and interested readers should refer to the SESSA manual.[63]

Finally, MC simulation is applied by SESSA to simulate a large set of trajectories. The distribution of path lengths can be obtained by making a histogram of the lengths of the trajectories. After a sufficient number of trajectories are obtained, the partial intensity $C_n(\vec{\Omega}_i,\vec{\Omega}_e)$ can be calculated as:

$$C_n(\vec{\Omega}_i,\vec{\Omega}_e) = \frac{1}{N_{traj}} \sum_{j=0}^{N_{traj}} \sum_{k=0}^{N_k} (\Delta C_n)_{k,j}(\vec{\Omega}_i,\vec{\Omega}_e) \qquad (2.3)$$

The number of trajectories N_{traj} is determined by the convergence factor which can be modified by the user. N_k is the number of steps per trajectory, which depends on the IMFP and the order of partial intensities. Trajectories are generated until the fractional change of the sum of all considered partial intensities is below the convergence factor. SESSA developers suggest that a convergence factor of 0.01 is suitable for many applications.

2.4.3 SESSA SIMULATION SETUP

The previous version of SESSA (V1.3) was not suitable for directly simulating nanoparticles as it did not have the capability of simulating layered spherical samples. The previous attempt of using SESSA V1.3 to simulate nanoparticles requires a complex and tedious geometrical transformation and calculations.[67] The current version of SESSA (V2.0) on the other hand can directly simulate layered-nanoparticles, enabling rapid simulations of NPs containing overlayers such as alkanethiol SAMs or core-shell nanoparticles. In this thesis work, all simulations are performed on the new SESSA (V2.0) unless otherwise mentioned.

SESSA was used to simulate various SAMs functionalized flat gold surfaces and AuNPs in chapter 4, chapter 5, appendix A and as well as the Au/Ag-core/shell nanoparticles in chapter 6. For simulation of flat surfaces with multiple layers, such as the case of SAMs, the user first define the number of layers, followed by assigning the appropriate composition, thickness, and density of each layer. This process is similar for simulating spectra for nanoparticle. For nanoparticle, the nanoparticle's size and number of overlayers are defined. For both flat surface and nanoparticles, the user then selects the peaks that they want to simulate. Next, the instrumentation conditions were selected to match the experimental XPS instrumentation used. The parameters include the type of X-ray source, the angle of the source and analyzer axis relative to the sample normal, and the analyzer lens acceptance angle. After simulation, SESSA provides the intensity of selected photoelectron peaks. These intensities are provided as the area under the curve in counts and can be transformed into atomic % by using the manufacture provided sensitivity factors which the simulation is based on and the instrumental transmission function. Many different types of simulations were performed in this thesis work using different sample

parameters. Therefore, the specific information regarding the simulation conditions will be provided in the subsequent chapters.

2.4.4 PYTHON SCRIPT FOR SESSA SIMULATION AUTOMATION

Though one can input the sample parameters through the graphical user interface (GUI), this process becomes extremely repetitive and time consuming when hundreds or thousands of simulation parameters need to be varied. A user must input the desired nanoparticle composition, instrumentation parameters, and simulation conditions for each analysis. On the other hand, the software is capable of receiving user inputs through a command line interface (CLI), in which the aforementioned sample composition and instrumentation parameters can be written into a text document in a command line fashion. However, the user still needs to construct the CLI file individually for each type of sample or simulation conditions. The current method of producing these CLI files remains repetitive and time consuming. Therefore, Python scripts were developed to assist the generation of CLI files and to automatically run simulations on SESSA without user supervision. More detail about the Python script and SESSA simulation automation can is provided in appendix D.

Chapter 3. CONTROLLING AND PROBING THE ORIENTATION OF IMMOBILIZED PROTEIN G B1 MUTANTS VIA SITE SPECIFIC COVALENT ATTACHMENT TO OLIGO(ETHYLENE GLYCOL) FUNCTIONALIZED GOLD NANOPARTICLES

Yung-Chen Wang[a] and David G. Castner*[a,b]

[a]National ESCA & Surface Analysis Center for Biomedical Problems, Department of Bioengineering, Box 351653, University of Washington, Seattle, WA 98195-1653 USA

[b]National ESCA & Surface Analysis Center for Biomedical Problems, Department of Chemical Engineering, Box 351653, University of Washington, Seattle, WA 98195-1653 USA

*Corresponding Author

David Castner

University of Washington

Department of Bioengineering and Chemical Engineering

Box 351653

Seattle, WA 98195

1-206-543-8094 (phone)

1-206-221-7451 (fax)

castner@uw.edu (e-mail)

3.1 ABSTRACT

Nanoparticles (NPs) have been widely used in many fields of science due to their unique physical properties. While many applications of NPs such as imaging probes or drug carriers often require the conjugation of proteins or biomolecules, the surface interactions between NPs and biomolecules remains underexplored. For example, the immobilization of immunoglobulin G (IgG) onto nanoparticle surfaces is critical for the development of many immunosensors and drug delivery nanocarriers. Notably, the orientation of the immobilized IgG can have significant impact on the clinical outcomes of these carriers by impacting its biostability and efficacy.

In this work, Protein G B1, a protein that will selectively bind to the Fc region of IgG, was immobilized onto gold NPs (AuNPs) functionalized with oligo(ethylene glycol)-Maleimide (OEG-MEG) self-assembled monolayers (SAMs). To control the orientation of the immobilized protein, we utilized site-specific maleimide-sulfhydryl reaction between the OEG-MEG SAMs and the cysteine amino acid in the protein. We use the surface sensitive analysis techniques of X-ray photoelectron spectroscopy (XPS) and time of flight-secondary ion mass spectrometry (ToF-SIMS) to characterize the immobilization of Protein G B1. The surface modification and protein immobilization was characterized using XPS. Further, by utilizing the high surface sensitivity and shallow sampling depth of ToF-SIMS (~2nm), it was possible to determine the orientation of immobilized Protein G B1 of slightly larger diameter (~4nm) by comparing the secondary ion signal of the asymmetrically distributed amino acids in the protein. Overall, site-specific maleimide-cysteine interaction and systematic surface characterization experiments enabled us to both control and probe the orientation of immobilized proteins on AuNPs.

3.2 INTRODUCTION

At the nanoscale, physical properties of materials often differ drastically compared to their bulk form.[37] Due to the nanoparticles (NPs) unique physical and chemical properties, NPs ranging from the sizes of 1 to 100nm have been widely used in many branches of science and industries.[68–71] For instance, non-toxic gold NPs (AuNPs) are a common candidate for drug carriers or imaging probes as they can be readily synthesized and can potentially penetrate hard-to-reach tissues such as passing the blood brain barrier for treatment of brain diseases.[69,72] Previous studies aimed at elucidating the relationship between NPs and their physiochemical properties have concluded that size, shape, and surface functionalization of NPs all play important roles in determining their toxicity and circulation time in biological systems.[13,14] Surface functionalization of AuNPs using SAMs has been effective in stabilizing particles in solution and modulating surface properties.[73] While much has been done investigating the relationship of the physical properties of NPs and their biological effects, NPs are often conjugated with other molecules to improve circulation life time, target specificity, or imaging modalities.[74] Antibody-conjugated NPs are often linked to other imaging probes and have shown great potential for the detection of metastatic cancer cells with a variety of imaging techniques such as magnetic resonance imaging (MRI), positron emission tomography (PET), and optical imaging.[75–77]

For many NP applications, the immobilization of immunoglobulin G (IgG) onto their surfaces is critical for the development of effective biosensors and drug delivery systems. To improve the efficacy of immobilized IgG on various surfaces, a great deal of research has focused on developing strategies to control the orientation of the immobilized antibodies. The ideal orientation for antigen binding to the Fab region would be the tail-on formation, leaving the Fab region freely exposed to the surrounding solution and the Fc region attached to the surface. In contrast to passive adsorption or uncontrolled covalent chemistries (e.g., carbodiimide and NHS ester), which often results in random or unfavorable antibody orientation, well-controlled antibody orientation can improve antigen binding and sensitivity.[78] Common strategies for achieving controlled orientation includes utilizing disulfide bond at the Fc region,[79–81]

nucleotide binding,[82,83] electrostatic based immobilization,[84,85] and Protein A or G based Fc region binding.[86–88]

Two recent reviews discusses the various techniques available for studying the orientation of immobilized antibody such as atomic force microscopy (AFM), Fourier transform infrared reflection spectroscopy (FTIR), spectroscopic ellipsometry, and time of flight-secondary ion mass spectrometry (ToF-SIMS).[89,90] These techniques are effective for studying orientation of molecules on flat surfaces but not all are applicable for studying orientation of molecules on nanoparticles. FTIR and spectroscopic ellipsometry for example cannot determine the orientation of molecules on nanoparticle surface because the molecules are isotropically orientated with respect to the analysis source.

In this study, Protein G B1,[40] a small IgG binding protein part of Protein G was immobilized onto AuNPs. The orientation of immobilized Protein G B1 on AuNPs was controlled via the maleimide-sulfhydryl reaction. The native Protein G B1 wild type (WT) does not contain a free sulfur group (cysteine) for the maleimide reaction. However, a cysteine point mutation can be introduced to achieve the specific maleimide-cysteine coupling between the NP and the protein. AuNPs in this study were functionalized with maleimide-oligo(ethylene glycol) (MEG-OEG) self-assembled monolayers (SAMs) to provide the maleimide group for the maleimide-cysteine reaction.

To characterize the immobilization process and probe the orientation of Protein G B1, surface sensitive analysis techniques X-ray photoelectron spectroscopy (XPS) and ToF-SIMS were employed. XPS is a well-established and commonly used technique for investigating surface functionalization by SAMs and protein adsorption by providing atomic composition of the sample.[91] The orientation of the immobilized protein can be determined using ToF-SIMS, which provides surface sensitive information about the composition of molecules of the uppermost ~2 nm of the sample.[92] Our group has demonstrated the effectiveness of utilizing both XPS and ToF-SIMS to characterize Protein G B1 on a variety of SAMs functionalized flat Au surfaces.[46–48,93]

In this work, we demonstrate the capability to control the orientation of immobilized Protein G B1 through site-specific maleimide-cysteine coupling on SAMs functionalized AuNPs. This work demonstrates an effective method for site-specific

Protein G B1 immobilization onto AuNPs and provides a base platform for future orientation IgG with controlled immobilization. In addition, the systematic characterization experiments in this study provide detailed information about protein-nanoparticle interactions and further our understanding of the complex protein-NP interface.

3.3 MATERIALS AND METHODS

3.3.1 SUBSTRATE PREPARATION

Small silicon (Si) wafers were used as substrate for AuNP samples in XPS and ToF-SIMS analysis. Si substrates were prepared from standard 100mm diameter wafers (Silicon Valley Microelectronics, Santa Clara, CA), with a thickness of 525 ± 25um. The Si wafers were diced into 1.1 cm^2 squares using the Disco DAD 321 Wafer Dicing Saw in the Washington Nanofabrication Facility (WNF). The diced Si wafers then undergoes a cleaning protocol which consists of an overnight wash in filtered and deionized (DI) water (18.2 MΩ) (EMD Millipore, Billerica, MA), followed by two 15-minutes washes in methylene chloride, two 15-minutes washes in acetone, and two 15-minutes washes in methanol. The cleaned Si wafers were then placed in a dedicated wafer holder, sealed with foil and stored under air at room temperature.

3.3.2 PROTEIN SYNTHESIS

All WT and cysteine mutant protein G B1 samples used in this study were synthesized by the Institute for Protein Design at the University of Washington (Seattle, WA). A total of five cysteine mutants were investigated in this study (Table 3.1). The locations of the cysteine mutants were strategically chosen based on the location, synthesis condition, and predicted binding site of protein G B1 to the IgG antibody. Proteins were expressed in E. coli and purified using a GE Healthcare ÄKTA Pure M anion exchange chromatographer (Pittsburgh, PA).

Table 3.1. Abbreviation of the five cysteine mutants

Wild type amino acid	**Location**	**Cysteine mutant abbreviation**
Threonine	11	T11C
Valine	21	V21C
Asparatic-acid	36	D36C
Glutamic-acid	42	E42C
Threonine	49	T49C

3.3.3 NANOPARTICLE SYNTHESIS AND SURFACE FUNCTIONALIZATION

Briefly, 13nm AuNPs were synthesized using the citrate reduction method adopted from Frens' study,[50] in which the size of the AuNPs can be readily tuned by adjusting the ratio between of gold and sodium citrate during particle synthesis. Prior to the synthesis of AuNPs, all glassware was cleaned using aqua regia to remove potential residual gold on the glassware from the previous synthesis. Reagents used includes sodium citrate tribasic dehydrate (Sigma-Aldrich, St. Louis, MO) and gold (III) chloride hydrate (99.999%) (Sigma-Aldrich, St. Louis, MO). AuNPs were prepared using 0.01% (w/v) of Au solution dissolved in DI water and 2.5% volume of the gold solution. Synthesized AuNPs were sealed and stored in the fridge at 4°C.

AuNPs were functionalized by 100uM of OEG-MEG disulfides (OH-$(EG)_6$-C11-S-S-C11-$(EG)_6$-OCH_2-CONH-Maleimide, Prochimia, Sopot, Poland) in DI water for 36 hours. The OEG-MEG functionalized AuNPs were sonicated for 30 seconds and subsequently purified using three rounds of 9,000 rpm/30 minutes centrifugation-resuspension method to remove excess thiol in solution. To break up the AuNP pellet before each resuspension, the pellet was vortexed for 30 seconds and sonicated for 1 minute.

3.3.4 PROTEIN IMMOBILIZATION ON GOLD NANOPARTICLES

AuNPs functionalized with the maleimide thiol were incubated with 1mg/mL of Protein G B1 WT and mutants in phosphate buffered saline (PBS) overnight at room

temperature on a shaker shaking at 200 rpm. To remove excess proteins in solution or proteins that are loosely bound to the surface of AuNPs, a series of purification protocols is required. After the overnight incubation with protein, the AuNPs were purified using three rounds of 12,000 rpm/40 minutes centrifugation-resuspension cycles using PBS. To break up the AuNP pellet before each resuspension, the pellet was vortexed for 30 seconds and sonicated for 1 minute. After the third rinsing cycle, the AuNP solution was transferred to a 1000kDa dialysis tube (SpectrumLabs, Rancho Dominquez, CA). Dialysis against DI H_2O was performed for two 2-hour rinse cycles and one overnight rinse under constant stirring. After the overnight dialysis, the AuNP solution was retrieved and purified by centrifugation using 12,000 rpm for 40 minutes. After removing the supernatant and backfilling with nitrogen gas, and the concentrated AuNPs were ready for XPS and ToF-SIMS analysis. For sample preparation, AuNPs were deposited onto clean silicon substrate and let dry in vacuum desiccator. Usually 10uL of the AuNP solution was deposited at a time until a confluent layer is formed on the Si wafer to prevent the signal from the substrate being detected during the XPS and ToF-SIMS analysis.

3.3.5 TRANSMISSION ELECTRON MICROSCOPY

The shape and size of the AuNPs were verified using TEM analysis. The AuNP sample for the TEM analysis was prepared by drying AuNPs directly onto a carbon-supported TEM grid (Ted Pella, Redding, CA). AuNP solution was produced by centrifuging 1.5mL of AuNPs under 12,000 rpm for 20 minutes. After removing the supernatant, the AuNPs were resuspended using 0.5mL mixture of 50:50 ethanol and DI H_2O. Ethanol solution was used to accelerate the drying process to prevent particle aggregation. TEM images were taken on FEI Tecnai G2 F20 TEM (FEI, Hillsboro, Oregon) operating with 200kV acceleration of the electron beam and 180kX-245kX magnification. All images were taken at a 2048 x 2048 pixel resolution using the bright field mode. The size and circularity of the AuNPs was analyzed from the TEM images using particle analysis algorithm in ImageJ (version 1.46d, National Institute of Health, USA).

3.3.6 X-RAY PHOTOELECTRON SPECTROSCOPY

XPS atomic composition data were collected on a Surface Science Instruments S-probe spectrometer equipped with a monochromatized Al Kα X-ray source (*hv* = 1486.6eV). For each sample, spectra were collected from three different regions with a 800 µm x 800 µm spot size, including survey scans from 0-1100 eV binding energy and detail scans (S 2p and N1s) to calculate the elemental composition and thickness approximation. The survey spectra were collected at 1 eV/Step for four scans with a dwell time of 100 ms. The detail S 2p and N 1s spectra were collected at 0.4 eV/Step with a dwell time of 100 ms for 32 and 16 scans respectively. The pass energy for the survey and detail scans was 150 eV. The S-probe data were processed using manufacturer provided sensitivity factors using the *Hawk Data Analysis* software.

3.3.7 TIME OF FLIGHT-SECONDARY ION MASS SPECTROMETRY (TOF-SIMS)

ToF-SIMS measurements were taken using the ION-ToF ToF-SIMS 5 instrument using Bi_3^+ primary ion source under 45° incident angle. For each sample, five high mass resolution positive ion spectra were acquired from different regions with a 100 µm x 100 µm size. For each spectrum acquisition, the total ion dose was below the static limit (10^{12} ions/cm^2) to prevent extensive disruption of the surface layer which can introduce signals from deeper in the sample as well as damage the proteins and SAMs. For all samples, the mass resolution at m/z 27 (positive) and m/z 25 (negative) typically was around 5000 (m/∆m). The acquired data were analyzed using the Ion-ToF measurement explorer software. For positive spectra, the masses were mass calibrated using the CH_3^+, $C_2H_3^+$, and $C_3H_5^+$ secondary ions. For negative spectra, the masses were mass calibrated using the CH^-, OH^-, and C_2H^- secondary ions.

3.4 RESULTS AND DISCUSSIONS

3.4.1 TEM ANALYSIS

TEM bright field image and particle analysis for the AuNPs is shown in Figure 5.1. Figure 3.1 (a) and (b) are representative bright field image of AuNPs synthesized

via citrate reduction. Image analysis using ImageJ shows that the AuNPs are monodispersed with average diameter of 13nm and a standard size deviation of 0.9nm (n= 2417 particles) (Figure 3.1(c)). The AuNPs are overall spherical with a major-axis to minor-axis ratio of 1.1 (Figure 3.1(c)). No batch-to-batch inconsistencies regarding the sphericity and size distribution of the particles were observed.

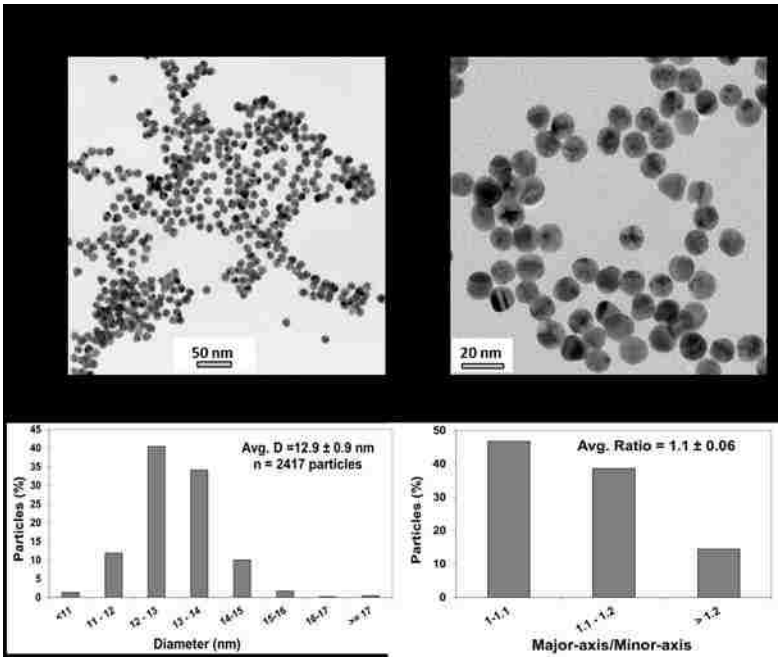

Figure 3.1. (a) and (b) shows TEM bright field images of AuNPs synthesized using the citrate reduction method. The distribution of nanoparticle diameter is shown in (c). It was determined using ImageJ's particle analysis algorithm that the AuNPs had were mostly monodispersed and had an average diameter of 12.9 ± 0.9nm. (d) The ratio of major-axis and minor-axis of the AuNPs were calculated to determine their sphericity. The average AuNPs were overall spherical with a major-axis to minor axis ratio of 1.1.

3.4.2 XPS ANALYSIS OF NANOPARTICLE FUNCTIONALIZATION AND PROTEIN IMMOBILIZATION

XPS was used to characterize the OEG-MEG SAMs functionalized AuNPs and the subsequent protein immobilization process. We hypothesized that the orientation of immobilized Protein G B1 can be controlled by the site-specific cysteine-maleimide coupling. Further, by utilizing the anti-fouling properties of OEG chains, the amount of nonspecific protein adsorption can be minimized.[94–96]

Table 3.2 provides the elemental composition of unfunctionalized (as synthesized), OEG-MEG functionalized, and Protein G B1 WT/mutants immobilized AuNPs. For citrate stabilized AuNPs (unfunctionalized), gold signal from the AuNPs and the carbon, oxygen and sodium signals from the sodium citrate layer were detected. After OEG-MEG SAMs functionalization, nitrogen (2.0 atomic %) and sulfur (1.5 atomic %) signals were observed as expected. The gold signal from the underlying AuNPs was attenuated after the SAM formation (46.7 to 15.7 atomic %). After incubation with Protein G B1 WT and purifications, we found a slight increase in the nitrogen signal (2.0 ± 0.7 to 3.7 ± 1.6 atomic %). As discussed earlier, Protein G B1 WT does not contain the necessary cysteine amino acid for the maleimide-sulfhydryl reaction with the OEG-MEG SAMs. This increase in nitrogen signal is likely due to nonspecific adsorption of the WT protein. This result is similar to previous results for Protein G B1 WT adsorption onto OEG-MEG SAM functionalized flat Au surfaces.[46] It is further possible that the edge and corner atoms present in AuNPs can also have an impact on the assembly of the OEG-MEG SAMs, leading to a different microenvironment favoring protein adsorption.[13]

Table 3.2. XPS elemental composition of unfunctionalized, OEG-MEG functionalized, and immobilized Protein G B1 WT, T11C, V21C, D36C, E42C, andT49C on AuNPs. The process of the OEG-MEG functionalization and protein immobilization can be determined by monitoring the N 1s signal and the attenuation of the Au 4f signal. (n.d. = not detected)

	XPS atomic %					
AuNPs sample	C 1s	O 1s	N 1s	S 2p	Au 4f	Na 1s
Unfunctionalized	34.6 ± 4.3	15.1 ± 4.4	n.d.	n.d.	46.7 ± 6.3	3.2 ± 1.5
OEG-MEG	59.5 ± 1.6	21.4 ± 1.0	2.0 ± 0.7	1.5 ± 0.5	15.7 ± 1.2	n.d.
OEG-MEG + WT	65.0 ± 4.5	23.3 ± 2.8	3.7 ± 1.6	0.8 ± 0.7	7.2 ± 4.0	n.d.
OEG-MEG + T11C	64.1 ± 1.4	22.4 ± 1.3	7.1 ± 0.6	0.6 ± 0.3	5.8 ± 2.2	n.d.
OEG-MEG + V21C	65.0 ± 1.5	23.1 ± 1.3	6.5 ± 0.7	0.8 ± 0.3	4.6 ± 1.6	n.d.
OEG-MEG + D36C	66.3 ± 0.4	20.4 ± 0.5	5.8 ± 0.5	1.0 ± 0.2	6.5 ± 0.4	n.d.
OEG-MEG + E42C	61.7 ± 0.9	22.6 ± 0.7	8.2 ± 0.4	1.0 ± 0.4	6.5 ± 0.4	n.d.
OEG-MEG + T49C	61.4 ± 1.4	22.4 ± 1.5	7.1 ± 0.3	1.0 ± 0.2	8.1 ± 0.2	n.d.

Compared to WT protein, all cysteine containing mutants resulted in a further increase of the nitrogen signal to 6-8 atomic %. This increase in nitrogen signal can be explained by the immobilization of mutant proteins through the site-specific maleimide-cysteine. Interestingly, the degree of the increased protein immobilization is not identical for all mutants. The small differences in nitrogen concentration for the different mutants could be due to the different locations of the cysteine mutant. Although the location of all cysteine mutants were strategically chosen to minimize disturbance to Protein G B1 structure, the introduction of the cysteine amino acid can still impact the protein structure and alter its nonspecific adsorption. It is also possible that the different locations of the cysteine are not equally accessible for the maleimide-cysteine reaction. Nonetheless, the XPS results show that all Protein G B1 cysteine mutants can be successfully immobilized onto the AuNPs through a maleimide-cysteine coupling. The specificity of the maleimide-cysteine coupling was also demonstrated by the Protein G WT control, which exhibited a significantly smaller increase in the nitrogen signal.

3.4.3 TOF-SIMS PEAK RATIO ANALYSIS TO DETERMINE PROTEIN ORIENTATION

ToF-SIMS can directly evaluate the cysteine-maleimide chemistry by monitoring the ratio of secondary ions originated from reacted ($C_4H_2NO_2S^-$, m/z 127.98) and unreacted ($C_4H_2NO_2^-$, m/z 96.01) maleimide rings.[93] Figure 3.2 shows the comparison of reacted to unreacted maleimide groups for the OEG-MEG functionalized AuNPs and two mutant proteins. Both V21C and T11C immobilized AuNPs shows higher ratios of reacted to unreacted maleimide groups, which is consistent with our XPS finding of a maleimide-cysteine based immobilization.

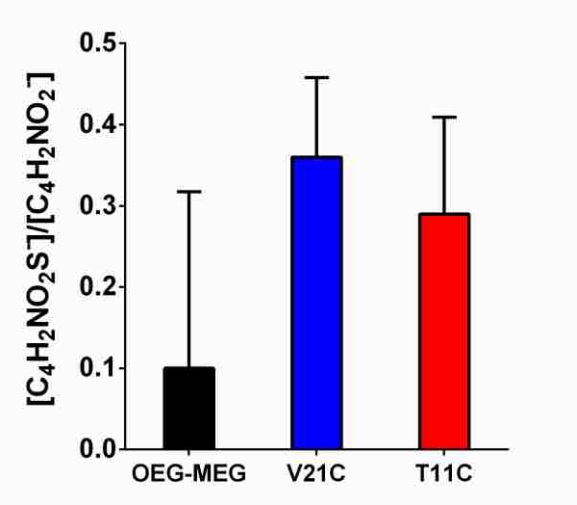

Figure 3.2. Comparison of secondary ion peak ratios of reacted (C4H2NO2S-, m/z 127.98) and unreacted (C4H2NO2-, m/z 96.01) maleimide rings.

Utilizing the high surface sensitivity of ToF-SIMS (~2nm sampling depth), it was possible to determine the orientation of immobilized protein G B1 (~4nm in length) by comparing the ratio of secondary ion intensities originating from opposite ends of the protein. This technique was previously used to identify the orientation and conformation of various protein films and Protein G B1 on SAMs modified flat substrates.[46,47] Figure 3.3(a) shows the amino acids that are asymmetrically distributed around the protein. These amino acids are grouped by their asymmetrically distributed location in Protein G B1: asparagine (Asn), leucine (Leu) and isoleucine (Ile) near the C-terminus, methionine (Met) and tyrosine (Tyr) near the N-terminus, and phenylalanine (Phe) and tryptophan (Trp) near the center. The structure of Protein G B1 WT and the relative location of the

cysteine mutants are shown in Figure 3.3(b). The mutants were distributed around the protein to enable a wide range of orientation control. Though a total of five different mutants were prepared, the ToF-SIMS data for the D36C protein has not been collected yet. The list of amino acid specific ion fragments used to calculate the peak intensity ratio for the identification of protein orientation was described previously.[97] The specific amino acid fragment used in this study and their corresponding mass is: Asn ($C_3H_6NO_2^+$ m/z 88.04, $C_4H_4NO_2^+$ m/z 98.02), Leu/Ile ($C_5H_{12}N^+$ m/z 86.09), Met ($C_2H_5S^+$ m/z 61.01, $C_4H_{10}NS^+$ m/z 104.05), Tyr ($C_3H_3O^+$ m/z 55.01, $C_7H_7O^+$ m/z 107.04), Phe ($C_8H_{10}N^+$ m/z 120.08, $C_9H_8O^+$ m/z 132.06), Trp (C_9H_8N m/z 130.06, $C_{10}H_{11}N_2^+$ m/z 159.09, $C_{11}H_8NO^+$ m/z 170.06).

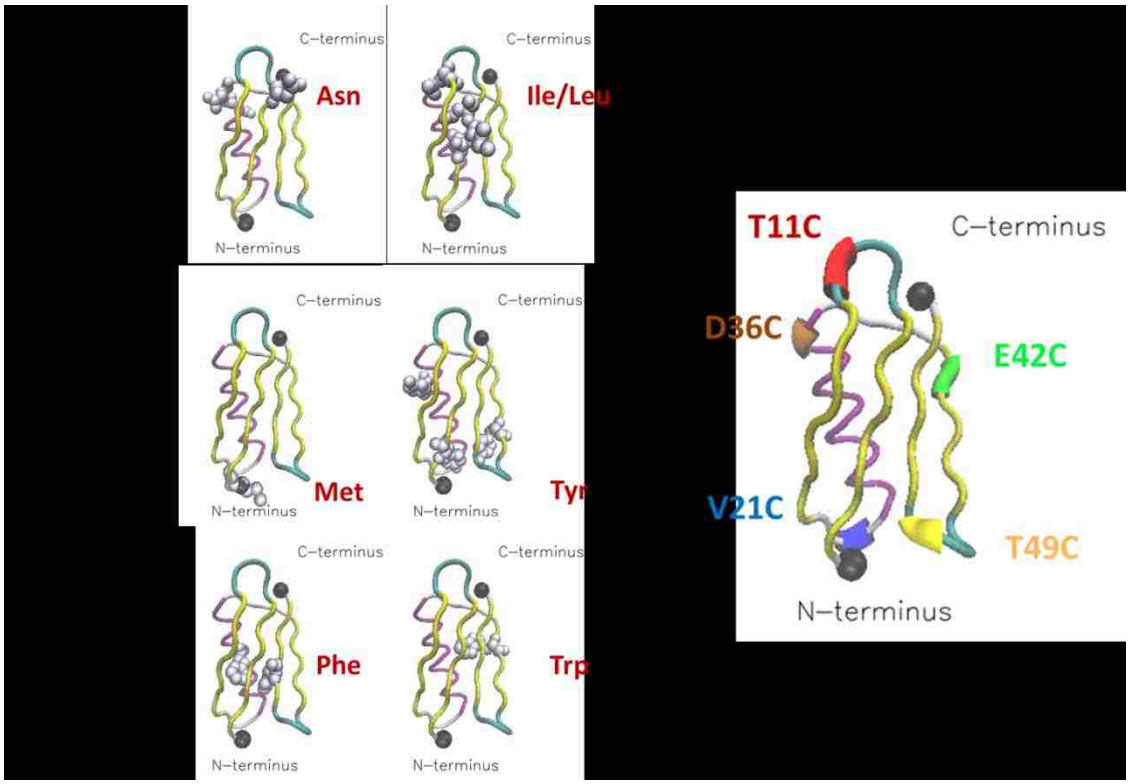

Figure 3.3. (a) Amino acids that are asymmetrically distributed in Protein G B1 are highlighted. The amino acids are selected based on their relative distribution: asparagine (Asn) and leucine/isoleucine (Leu/Ile) near the C-terminus, methionine (Met) and tyrosine (Tyr) near the N-terminus, and phenylalanine (Phe) and tryptophan (Trp) near the center of Protein G B1. (b) The location of the cysteine point mutations are highlighted (red: T11C, green: E42C, yellow: T49C, blue: V21C, brown: D36C.) Figure produced using Visual Molecular Dynamics (VMD).

Figure 3.4 summarizes the ToF-SIMS peak ratio comparisons of the asymmetrically distributed amino acids. Ideally, N-terminus side mutant proteins (V21C and T49C) will be immobilized onto the OEG-MEG functionalized AuNP surface with the N-terminus side facing towards the particle. This will preferentially expose the amino acids on the C-terminus side of the protein towards the incoming primary ion beam. The opposite result can be expected for C-terminus side mutant proteins (T11C and E42C) in which the N-terminus portion of the protein is exposed. The ToF-SIMS peak ratio analysis indeed show a higher ratio between the sum of intensity between C-terminus amino acids peaks and N-terminus amino acids peaks for N-terminus side mutants (figure 3.4(a)), indicating orientation control was achieved. This finding in which T11C and V21C mutants located at the opposite of the protein results in opposite protein orientation is consistent with previous results for OEG-MEG functionalized flat gold surfaces.[46,48]

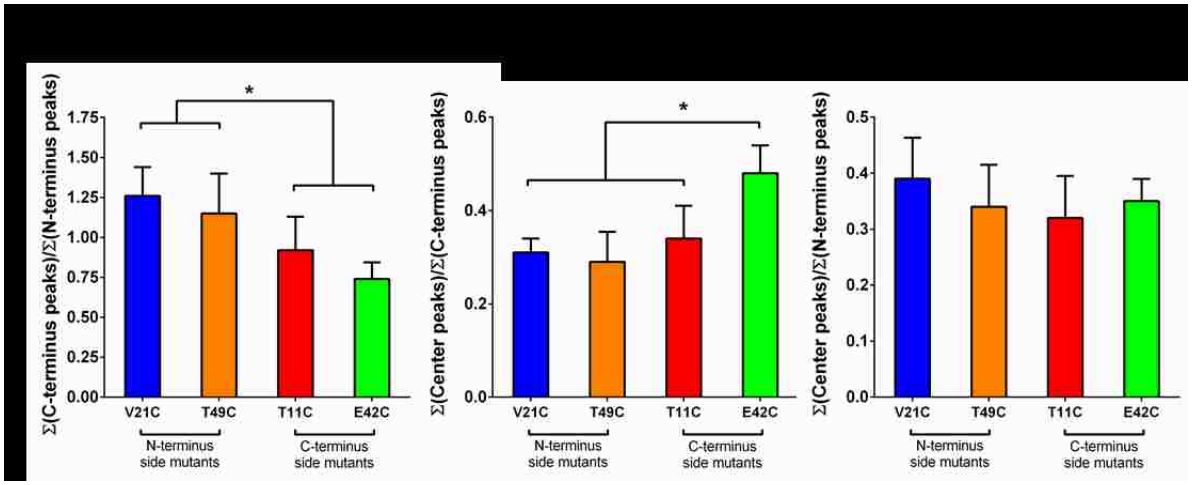

Figure 3.4. Overview comparison of ToF-SIMS amino acid peak ratios from different regions of the protein. V21C and T49C mutants are categorized as N-terminus side mutants as they are physically closer to the N-terminus end while T11C and E42C are categorized as C-terminus side mutants as they are closer physically closer to the C-terminus end. (a) Ratio of the sum of C-terminus amino acid peaks (Asn, Leu and Ile) to the N-terminus amino acid peaks (Met and Tyr) for the Protein G B1 cysteine mutants. (b) Ratio of the sum of center amino acid peaks (Phe and Trp) to the C-terminus amino acid peaks. (c) Ratio of the sum of center amino acid peaks (Phe and Trp) to the N-terminus amino acid peaks. *$p < 0.05$

It is important to note that we are making an ideal assumption that the immobilized protein will retain their orientation after the immobilization. Though previous

studies have shown that OEG functionalized flat gold surfaces can help retain protein structure upon adsorption and prevent nonspecific protein adsorption,[98] whether this property will translate onto AuNPs requires additional research. We therefore investigated another possible protein orientation in which the protein attaches not to one of the terminus ends, but rather in a side-on orientation. In figure 3.3(b), we show the ToF-SIMS peak ratio between C-terminus amino acids and center amino acids. V21C, T49C, and T11C were found to have similar peak ratio indicating no preferential side-on orientation. Interestingly, mutant E42 exhibited a higher ratio of center versus C-terminus peaks, indicating a preferential side-on orientation. Though we categorize E42 as a C-terminus side mutant, it is, compared to other mutants, closer to the middle of the protein with respect to the terminuses. The higher ratio of center over the C-terminus peaks can indeed be explained by the relative location of the E42 mutant. The E42 mutant is closer to the C-terminus end, which results in relatively low intensity of C-terminus amino acid peaks. This ultimately leads to the higher center over C-terminus amino acid peak ratio. One would therefore expect to see the opposite trend when comparing the ratio of center peaks against N-terminus peaks. However, figure 3.4(c) shows that all mutants exhibited comparable ratio. Thus, it is unclear whether a side-on orientation is preferentially adopted by the E42C mutant protein.

3.5 CONCLUSION

In this study, the surface functionalization and immobilization of protein G B1 onto AuNPs were characterized using XPS and ToF-SIMS. We demonstrated the capability of probing the orientation of immobilized Protein G B1 using ToF-SIMS analysis by asymmetrically distributed amino acids and controlling the orientation of protein G B1 on AuNPs using the site-specific maleimide-cysteine coupling. Some nonspecific protein adsorption was observed for the Protein G B1 WT which does not contain a cysteine amino acid. We demonstrated that N-terminus side V21C and T49C mutants displayed a preferential orientation with the C-terminus of the immobilized protein pointing away from the AuNPs. In contrast, C-terminus side T11C and E42C mutants preferentially orient the N-terminus side of immobilized protein away from the

AuNPs. Overall, the findings of this study provide valuable information for understanding AuNP surface modifications, protein-AuNPs interactions, and a platform for the future work related to the controlled IgG immobilization onto AuNPs functionalized with Protein G B1.

3.6 ACKNOWLEDGEMENT

Y.-C. Wang and D.G. Castner gratefully acknowledge the support from National Institutes of Health grant EB-002027 to NESAC/BIO from the National Institute of Biomedical Imaging and Bioengineering. Part of this work was conducted at the Molecular Analysis Facility, a National Nanotechnology Coordinated Infrastructure site at the University of Washington that is supported in part by the National Science Foundation (grant ECC-1542101), the University of Washington, the Molecular Engineering & Sciences Institute, and the Clean Energy Institute. Recombinant protein G B1 used in this work was obtained from the Institute for Protein Design, University of Washington, Seattle, WA. Y.-C. Wang was supported by the National Science Foundation Graduate Research Fellowship Program under Grant No. DGE-1256082.

Chapter 4. EVALUATING THE INTERNAL STRUCTURE OF CORE–SHELL NANOPARTICLES USING X-RAY PHOTOELECTRON INTENSITIES AND SIMULATED SPECTRA

Maksymilian Chudzicki,[a] Wolfgang S.M. Werner,[a]* Alex Shard,[b] Yung-Chen Wang[c] and David G. Castner[c,d], Cedric J. Powell[e]

[a]Technische Universität Wien, Institut für Angewandte Physik, Wiedner Hauptstraβe 8-10, A-1040 Vienna, Austria

[b]National Physical Laboratory, Hampton Road, Teddington, Middlesex TW11 0LW, U.K.

[c]National ESCA & Surface Analysis Center for Biomedical Problems, Department of Bioengineering, Box 351653, University of Washington, Seattle, WA 98195-1653 USA

[d]National ESCA & Surface Analysis Center for Biomedical Problems, Department of Chemical Engineering, Box 351653, University of Washington, Seattle, WA 98195-1653 USA

[e]Materials Measurement Science Division, National Institute of Standards and Technology, Gaithersburg, Maryland 20899-8370, United States

*Corresponding Author
Wolfgang S.M. Werner
Technische Universität Wien
Institut für Angewandte Physik
Wiedner Hauptstraβe 8-10, A-1040
Vienna, Austria
werner@iap.tuwien.ac.at (e-mail)

4.1 ABSTRACT

The functionality of a new version of the National Institute of Standards and Technology Database for the Simulation of Electron Spectra for Surface Analysis (SESSA) (Werner, W. S. M.; et al. U.S. Department of Commerce/NIST: Gaithersburg, Maryland, 2014) has been extended by implementing a new geometry engine. The engine enables users to simulate Auger-electron spectra and X-ray photoelectron spectra for different predefined morphologies (planar, islands, spheres, multilayer core–shell particles). We compared shell thicknesses of core–shell nanoparticles derived from core–shell XPS peak intensities using Shard's method, which allows one to estimate shell thicknesses of core–shell nanoparticles, and a series of SESSA simulations for a wide range of nanoparticle dimensions. We obtained very good agreement of the shell thicknesses for cases where elastic scattering within the shell can be neglected, a result that is in accordance with the underlying assumptions of the Shard model. If elastic-scattering effects are important, there can be thickness uncertainties of up to 25%.

Experimental spectra of functionalized gold nanoparticles obtained by Techane et al. were analyzed with SESSA 2.0 both with respect to the relevant peak intensities as well as the spectral shape. Good agreement between experiment and theory was found for both cases. These results show that the single-sphere model for core–shell nanoparticles is valid when just using peak intensities, but more detailed modeling is needed to describe the inelastic background.

4.2 INTRODUCTION

X-ray photoelectron spectroscopy (XPS) is a powerful tool extensively used in surface analysis to study the chemical and physical properties of surfaces and interfaces.[55,99–102] As the field of nanotechnology has grown, increasingly engineered and functional nanomaterials are being synthesized and exploited in numerous applications, ranging from biomedical assays to optoelectronic devices. There is a consequent requirement to develop and refine procedures to precisely characterize nanostructures at the nanoscale.[10,102–107] XPS is in this regard a very powerful technique as it provides information not only on the composition but also on the chemistry, structure and size of the investigated system.[108–113]

The physical processes governing the electron-solid interaction in conventional XPS give rise to attenuation of electrons over distances of a few nanometers, which makes XPS suitable for the characterization of nanosized structures.[65] Thus, the signal will be affected by the morphology of the sample, which is a well-known fact since the early days of XPS when it was already used to study nanosized catalysts.[114–116] However, it is far from trivial to extract structural information from XPS spectra. Deriving universal, analytical expressions that directly connect the morphology of a system to peak intensities, or other features of an XPS spectrum, is a formidable task and can often only be achieved by applying various approximations for some special cases.[117–122] An example of such a direct translation of features of an XPS spectrum to morphological properties is provided by Shard,[123] who established a non-iterative, empirical algorithm to estimate the shell thickness of core-shell (CS) particles given the radius of the inner core, the attenuation lengths for photoelectrons in the overlayer and core materials, and the experimental XPS CS peak-intensity ratio.

Alternatively, the QUASES software package can be useful for nanomorphologies characterization by essentially comparing background subtracted spectra with a reference spectrum.[124] However, at present this is only possible for a limited number of pre-selected morphologies, similar to the earlier versions of SESSA. In the general case of arbitrary nanostructures for which universal models are presently not available, the process of data interpretation is greatly facilitated by simulation

software such as the National Institute of Standards and Technology database for the Simulation of Electron Spectra for Surface Analysis (SESSA), which can be used to simulate XPS spectra and peak intensities for samples with different nanomorphologies.[62,63] Moreover, employing simulation software provides insight by varying the parameters describing the nanomorphology and matching to features of experimental spectra. SESSA provides all physical quantities required to conduct simulations of Auger-electron- or XPS-spectra for a given sample using a highly efficient simulation engine operating in the reverse trajectory mode.[66] Simulations can be made for any photon energy below 30 keV and for any mixture of circularly and linearly polarized light, as defined by a user. The original version of SESSA provided the capability to simulate spectra for layered specimens with each layer having a given composition and thickness. The present version 2.0 of SESSA provides the capability for simulating spectra for various types of nanomorphologies (spheres, layered spheres and islands). In SESSA 2.0, the geometrical parts of the simulation are performed by the PENGEOM package, which constitutes a standalone package, distributed within the PENELOPE code system, for defining arbitrary morphologies and tracking of electron trajectories.[125]

In a recent work,[126] a developmental version of SESSA was used to investigate various systems of nanoparticles (NPs): periodically aligned monolayers of CS particles, dispersed sub-monolayer arrays, as well as powder-like assembles of CS particles. This work provided information on various features in angle-resolved XPS that arise with increasing periodicity of the investigated structures. Also, it was shown that dispersed powders (i.e. structures without long-range periodicity) of CS particles can be modeled by a single sphere.[126] Shard has described a simple method for calculating the shell thickness of CS nanoparticles (NPs),[123] which shall be referred to as the “T (NP) formula” within the present work. This method is based on the straight-line approximation (SLA), in which all signal electrons are assumed to follow rectilinear paths. This approach is a good approximation for materials with small atomic numbers where elastic-scattering effects can often be neglected.

We have used SESSA 2.0 to reproduce results from the T (NP) formula under the same experimental conditions and assumptions for two important cases: a beryllium

shell on a gold core and a palladium shell on an aluminum oxide core. The former case (beryllium with atomic number Z = 4) is a reasonable model system for a hydrocarbon layer, containing carbon (Z = 6) and hydrogen (Z = 1), while the latter case is a representation of a catalytic system. Such systems of strong scatterers on weak scatterers and vice versa often appear in nanotechnology in the form of catalysts or functionalized NPs, respectively. The simulations were repeated subsequently under physically more realistic conditions (e.g., taking into account elastic scattering and including contamination layers) to study the limitations of the T (NP) formula.

Techane et al.[110] have used SESSA Version 1.3 to simulate CS NPs made of a gold core with an organic shell, a self-assembled monolayer (SAM) of carboxylic acid thiol. As this version did not provide means to simulate spherical particles of any kind, Techane et al. modeled a CS nanoparticle (NP) by assembling it from a number of concentric cylinders. The process involved tedious modeling and is therefore not feasible for routine simulations. We have used SESSA Version 2.0 to model spherical, self-assembled monolayers (SAMs) attached to gold NPs. The new software provides a major improvement in terms of speed, efficiency and simplicity compared to the approach of Techane et al. with SESSA Version 1.3. The present analysis not only confirms the results of Techane et al.[110] but also gives excellent agreement for the shape of the inelastic background in survey XPS spectra after a transmission-function correction.

4.3 MATERIALS AND METHODS

4.3.1 SESSA

SESSA is a standard reference database distributed by the National Institute of Standards and Technology containing all data needed for quantitative simulations of XPS and Auger- electron spectra.[62,63] Data retrieval is based on a powerful expert system that queries the databases and provides the data to the user or the simulation engine for arbitrarily shaped geometrical configurations. The simulation engine is a particularly crucial part of SESSA as it enables the user to conduct batch simulations of arbitrarily shaped nanostructures.

The extensive capabilities of SESSA Version 2.0 for simulating various nanomorphologies are based on the PENGEOM package, a general-purpose geometry package that allows one to define quasi-arbitrary geometries using quadric surfaces. PENGEOM comes as a standalone part of the PENELOPE code system which is widely used for simulation of electron and photon transport processes.[125] Based on the information provided by the user, a geometry file is created by SESSA and internally passed to PENGEOM which initializes the geometry, stores it in memory and provides various functions for tracking the electron trajectory. The geometry definition is based on a simple syntax with which surfaces such as planes, spheres, hyperboloids etc. can be defined and subsequently used to delimit phases of a material. Existing phases can be further used as building blocks for larger structures.

The recently released version V2.0 does not yet provide the option to load externally defined geometry files; however, this feature will be implemented in the upcoming version V2.1. The possibility to simulate externally defined geometries further expands SESSA's application possibilities as it, for example, enables the simulation of XPS intensities of lithographically manufactured by XPS with hard X-rays. Currently the following morphologies are predefined and can be chosen: planar, roughness, islands, spheres and layered spheres. The planar and roughness morphologies are comprised of an arbitrary number of stratified layers placed on a semi-infinite substrate. The composition and thickness of each layer can be easily changed by the user and SESSA always provides estimates for all needed material properties. For the roughness morphology, an additional parameter is defined to account for the increase in relative surface area (RSA) of a rough surface compared to a perfectly planar specimen. The increase in signal intensity due to an increased surface area is accounted for with the RSA parameter. The island and sphere morphologies enable one to simulate structures placed on a layered sample as in the case of a planar morphology.

For islands, the simulated structure consists of a trapezoid with variable dimensions in x, y and z directions together with variable inclinations of the side-walls. In the case of spheres, the dimensions of the sphere and its composition can be varied. The layered-spheres morphology allows one to simulate a spherical particle consisting of an inner core with an arbitrary number of overlayers. The dimensions of the sphere

as well as the composition and thickness of each layer can be chosen by the user. All nanomorphologies are simulated as periodic arrays where the periods can be selected to represent isolated or dense assemblies of features. As shown in our prior work[126] and by Frydman et al.,[122] the surface of a dispersed powder of CS NP seen by a detector is equivalent to the surface of a single sphere and is independent of the viewing angle by the detector. Therefore, a simulation for a well-dispersed array of CS NPs yields the same ratio of photoelectron intensities from the core and the shell as from a bulk powder.

In order to minimize computation times and to enable faster processing of batch jobs, a highly efficient Monte Carlo code is employed, based on the trajectory-reversal method of Gries and Werner.[66] In contrast to conventional Monte Carlo codes where electrons are tracked on their trajectories from the source to the detector, the trajectory-reversal approach tracks electrons in the opposite direction, starting from the detector and following the trajectory back to the point of origin. Thus, all electrons contribute to the signal resulting in significantly decreased simulation times, typically in the range from seconds to several minutes, depending on the number of peaks to be simulated and the desired precision in the results.

4.3.2 SHARD'S T (NP) FORMULA

Shard[123] addressed the general problem of interpretation of XPS intensities of CS particles by establishing a simple and non-iterative procedure, the T (NP) formula, that enables one to directly convert peak-intensity ratios to shell thicknesses in two-component systems. Emphasis was put on CS particles as they constitute a particularly important field of research due to their many applications.[106,127–131]

The parameters in the T(NP) formula are A, the ratio of the XPS peak intensities from the shell and core materials, respectively, the radius R of the core, and the electron attenuation lengths L of the core and shell photoelectrons in each material. For normalization of the peak intensities I_i, calculated or experimentally determined intensities of the pure materials can be used and are written as $I_i\infty$. Following the notation in Shard's work, the subscript i = 1, 2 is used to identify photoelectrons arising

from the shell and core materials, respectively, giving the normalized peak-intensity ratio A as:

$$A = \frac{I_1 I_2^{\infty}}{I_2 I_1^{\infty}} \tag{4.1}$$

Shard's approach for obtaining an expression for the shell thickness of a CS NP was to make approximations for overlayer thicknesses of different limiting cases, such as planar samples, infinitesimally small particles (see eq. (4.1)), or macroscopic particles (see eq. (4.3)). The formula for calculation of nanoscopic CS particles was obtained by combining these limiting cases. The fit parameters α and β were determined by validating the results with numerical calculations, so that the validity of the resulting formula is ensured within the limits of the model and the relevant core radii and shell thicknesses. The resulting T (NP) formula is given by:

$$T_{NP}(A) = \frac{\frac{I_{R\to\infty} R}{R + \alpha} + \beta T_0}{1 + \beta} \tag{4.2}$$

$$T_{R\to\infty} = \frac{0.74 A^{3.6} \ln(A)\, B^{-0.9} + 4.2 A B^{-0.41}}{A^{3.6} + 8.9} \tag{4.3}$$

$$T_0 = R\left[(ABC + 1)^{1/3} - 1\right] \tag{4.4}$$

For a detailed explanation of the values α, β, B and C, the reader is referred to Shard's original work.[123] Equation (4.2) enables one to calculate the shell thickness of a CS NP given the (experimental) normalized intensity ratio, the attenuations lengths $L_{i,j}$ of the core and shell materials, as well as the core radius. Both the attenuation lengths and the pure elemental intensities I∞ needed to calculate the normalized intensity ratio A are easily retrieved using SESSA by running simulations or querying the expert system. Equation (4.2) applies to radii of NPs ranging from approximately 1 nm to 1 µm and provides shell thicknesses with a typical standard uncertainty of 4 %. This uncertainty is considerably smaller than the typical uncertainty of the attenuation lengths $L_{i,j}$, that are based on inelastic mean free paths with estimated uncertainties of about 10 %.[132]

4.3.3 EVALUATION OF THE T (NP) FORMULA

In order to evaluate the T (NP) formula, the following approach was adopted: For a given shell thickness, T_{SESSA}, core radius R, and material composition of the CS system, a simulation was conducted using SESSA, yielding a simulated value for the normalized intensity ratio, A_{SESSA}. Using this value for A_{SESSA} in eq. (4.2), together with the core radius R and the constants B and C, the calculated shell thickness TNP is obtained. In the ideal case T_{SESSA} and T_{NP} are equal, and a plot of TSESSA as a function of TNP yields a straight line with unity slope through the origin.

The T (NP) formula was used to investigate the two previously described model systems consisting of a weakly scattering beryllium shell on a gold core (system 1) and a palladium shell on an aluminum oxide core (system 2), respectively. The evaluation was conducted for four different core radii as displayed in figure 4.1. For each case, 50 simulations were conducted with varying shell thicknesses in the range from $0.1L_{1,a}$ to $5L_{1,a}$ in steps of $0.1L_{1,a}$.

The values of $L_{1,a}$ for systems 1 and 2 were 3.15 nm and 1.20 nm, respectively. $L_{1,a}$ also determines the size of the simulated CS NPs as T and R are given in units of L1,a. Since the overlayer thickness was varied table 1 displays the size ranges of the simulated CS systems. Figure 4.1 displays the four different CS particle systems used in the simulations. The figure is given to scale to emphasize the wide range of radii employed for the evaluation. The corresponding sizes for each material composition can be found in table 1. It is important to note that with a shell thickness of 5 $L_{1,a}$, the XPS intensity from the core will almost certainly be too weak to measure in practice. For this reason the T (NP) formula was only validated using the SLA up to ≈ 3 $L_{1,a}$ in the original work[123] but, because the formulation is accurate in at least some of the extremes of core radii and shell thicknesses, we may expect it to be valid over a wider range.

Table 4.1. Minimum and maximum diameters of the Be/Au and Pd/Al_2O_3 CS NPs for each core radius, according to figure 1. The minimum and maximum values depend on the shell thickness, which ranged from $0.1L_{1,a}$ to $5L_{1,a}$

Core radius R	**Be/Au**		**Pd/Al_2O_3**	
	min. diameter [nm]	*max. diameter* [nm]	*min. diameter* [nm]	*max. diameter* [nm]
$0.5L_{1,a}$	3.79	34.71	1.44	12.23
$1L_{1,a}$	6.94	37.86	2.65	14.43
$8L_{1,a}$	51.11	82.03	19.49	31.27
$32L_{1,a}$	202.55	233.47	77.22	89.01

4.4 RESULTS AND DISCUSSIONS

4.4.1 EVALUATION OF THE T (NP) FORMULA

Figure 4.2 displays the results of the evaluation in form of a plot displaying T_{NP} against T_{SESSA} for the Be/Au and Pd/Al_2O_3 CS NPs for cases **I**, **II**, **III** and **IV** of figure 1 and the range of shell thicknesses described above. The red dotted lines consist of 50 discrete points each corresponding to an independent simulation. Two sets of simulations were performed for each set of materials, core radii, and shell thicknesses, one accounting for elastic-scattering effects (b and d) and one with the SLA (a and c) where all electron trajectories follow rectilinear paths. Values of TSESSA and TNP were normalized to the appropriate value of $L_{1,a}$.

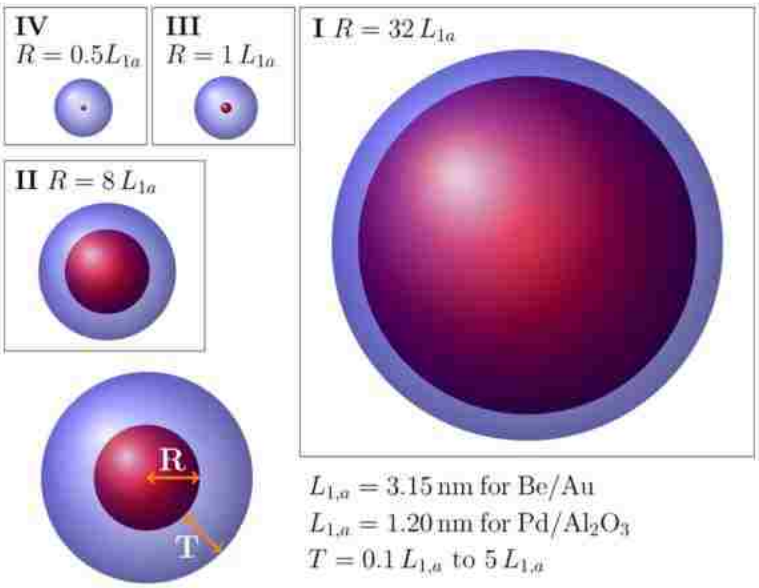

Figure 4.1. To scale representation of the four CS systems used for the evaluation of the T(NP) formula. The definitions of the core radius R and the shell thickness T are displayed in the bottom left corner. The actual size depends on the chosen shell material as all dimensions are given in units of L1,a, the attenuation length of shell photoelectrons within the shell. For both model systems, the values of L1,a are listed at the bottom. In all four cases I−IV, the shell thickness T is depicted with a constant thickness of $5L_{1,a}$, while the simulations were conducted for values ranging from $0.1L_{1,a}$ to $5L_{1,a}$. The core radii for cases I−IV are, respectively: I: R =$32L_{1,a}$; II: R =$8L_{1,a}$; III: R = $L_{1,a}$; IV: R = $0.5L_{1,a}$.

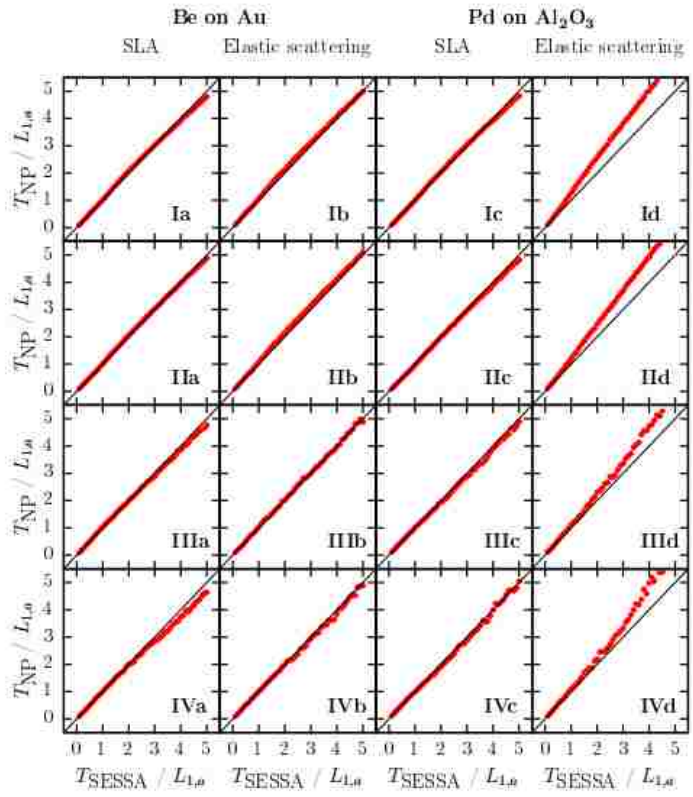

Figure 4.2. T_{NP} plotted against T_{SESSA} for the Be/Au and the Pd/Al2O3 NP systems of Figure 4.1. T_{NP} was calculated according to eq 4.2 using the normalized intensity ratio ASESSA obtained from a simulation conducted with the shell thickness TSESSA. Every red dot corresponds to a simulation at a different shell thickness, ranging from $0.1L_{1,a}$ to $5L_{1,a}$. For each material system, the plots on the left side were conducted with the SLA, whereas the plots on the right side depict simulations with elastic scattering. The roman numerals correspond to the numerals in Figure 4.1

As seen on the left side of figure 4.2, few significant deviations occurred between T_{NP} and T_{SESSA} for the Be/Au system, both when elastic scattering was accounted for and when the SLA was employed since the shell is a weakly scattering material. That is, most trajectories are close to rectilinear.

It should be stressed that the T (NP) formula is based on the SLA and does not account for elastic scattering. For the Be/Au model system, there is generally good correlation between T_{NP} and T_{SESSA}. Some small deviations, however, were found at relatively large shell thicknesses ($T/L1,a \geq 3$) and a core radius of $R = 0.5$ L1,a, as shown in panel **Iva** in figure 4.2. The deviations, however, appear at shell thicknesses which are beyond the limits of the T (NP) formula, which was established for shell thicknesses of approximately $T/L_{1,a} \leq 3$.[123]

For Pd/Al_2O_3 NPs the shell material has a high atomic number and stronger elastic-scattering effects are expected.[99]

Elastic scattering leads to deflections of photoelectrons emitted from the core material and therefore a lower core signal, thus resulting in an overestimate of the shell thickness using the T (NP) formula. A comparison between results of simulations conducted with and without the SLA in figure 4.2 shows this effect very convincingly.

The simulations denoted by **Ic** to **IVc** were carried out using the SLA and in this case there are no significant differences between T_{NP} and T_{SESSA}. The deviations from this ideal behavior due to elastic-scattering effects manifest themselves very clearly in the **Id** to **IVd** panels.

This effect can be explained by comparing the relative contributions of core and shell photoelectrons of two CS NPs with different radii but constant shell thickness, as shown in figure 4.1-**I** and 4.1-**IV**. For a very small core radius, the whole core contributes to the signal in equal measure. Also, the relative shell intensity is then much larger as the shell comprises most of the CS particle volume. However, given a large core radius with the same shell thickness, most of the core intensity originates from the region just beneath the shell. As a first approximation, the relative volume ratio of the core and shell regions contributing to the signal and the normalized intensity ratio A are both closer to unity than in the former case. The attenuation of the core signal due to elastic scattering has a larger impact on larger particles as the signal contribution from the core increases. This behavior is also reflected in eq. (4.3), which has a logarithmic contribution in A. The value of A, giving the shell-to-core ratio of photoelectron intensities, is large for small particles where the shell is dominant. Since the shell-to-core ratio A has a logarithmic contribution to the T (NP) formula, as seen in equations (4.2) and (4.3), the uncertainty in the calculated shell thickness will be large for small values of A, while for large values of A the uncertainty will be negligible. Thus, when A is close to unity, small changes in A have a large effect on its logarithm, leading to deviations at smaller shell thicknesses.

The Pd/Al_2O_3 material system was also studied with regard to the influence of a 0.15 nm carbonaceous contamination layer on the normalized intensity ratio and the predicted shell thickness. It was found that the results obtained with and without the thin

contamination layer were indistinguishable for all cases, meaning that the presence of a thin carbonaceous contamination layer does not affect the result obtained with the T (NP) formula, given that the contamination is the only carbonaceous compound of the CS system. Thicker contamination layers, which approach the electron attenuation length in thickness, will affect the accuracy of the T (NP) calculation. Such situations can be classed under the general case of core-shell-shell systems. These may be easily modelled using SESSA but significant modifications to the T (NP) approach are required to deal with such systems. As shown later in figure 4.3, such a contamination layer has a large influence on the normalized intensity ratio if carbon is present within the core or shell.

In summary the T (NP) formula performs very well on systems where applying the SLA is justified, such as gold NPs functionalized with alkanethiols. However, the method has relatively large uncertainties (up to 25 % in panels I**d** to I**Vd** of figure 4.2) in the shell thick- nesses of material systems comprised of a strongly scattering shell since the T (NP) formula is based upon the assumption of rectilinear electron trajectories.

4.4.2 APPLICATION OF SESSA TO EXPERIMENTAL XPS DATA

Self-assembled monolayers (SAMs) of alkanethiols on flat gold surfaces are a widely employed model system in nanotechnology due to their well-defined structure and surface properties. Numerous studies deal with the synthesis, characterization, thermodynamics, and reactivity of alkanethiols on flat gold surfaces but there are still many open questions regarding basic properties of SAMs on highly curved surfaces.[32,37,127,133–136]

Techane et al.[110] conducted a quantitative analysis of the SAM-layer thickness of 16-mercaptohexadecanoic acid ($C_{16}COOH$) on flat gold and on 14 nm diameter gold nanospheres using XPS for experimental measurements and SESSA Version 1.3 for simulations of the two systems. Since SESSA 1.3 did not provide means to simulate spherical particles directly, Techane et al. modeled a CS particle using nine concentric cylinders connected by flat, angled surfaces. These top surfaces, consisting of $C_{16}COOH$ overlayers attached to a semi-infinite gold substrate were simulated using SESSA 1.3. In order to get the correct peak intensities of the SAM on a gold NP,

geometric weighting factors were applied to each simulated surface to account for the different areas.

With SESSA Version 2.0, simulation of CS NPs with an arbitrary number of shells becomes a matter of defining the compositions, thicknesses, and atomic densities of each layer with the help of a user-friendly graphical user interface. The simplicity of this approach enables users without detailed expertise in modeling to investigate systems of different nanomorphologies on a routine basis. In the present work, SESSA 2.0 was employed to model the data of Techane et al.

4.4.3 SIMULATIONS OF SAMS WITH SESSA 2.0

Unlike a dense material, the atomic density of SAMs attached to highly curved surfaces decreases with the radius because of the spreading of the aliphatic chains. It should be noted that, on an atomic scale, gold NPs consist of (111) and (100) terraces and are therefore not perfectly spherical;[107,137] however, in the course of this work the 14 nm gold NPs were assumed to be perfectly spherical to facilitate the process of simulation with SESSA.

In Techane's model, the atomic density was assumed to be constant throughout the whole thickness of each concentric cylinder, since accounting for the changing density was not easily possible using their approach.[110] A decreased SAM density with radius of the gold NP could result in the enhanced mobility of the chains leading to defects and kinks in the structure of the SAM and a reduced thickness compared to the corresponding SAM on a planar substrate.

The goal of the work by Techane et al. was to obtain the best possible agreement between the experimentally derived and simulated normalized intensities by varying the thickness of the CH_2 groups and the relative surface area (RSA) parameter. This parameter accounts for the increase in surface area due to curvature or roughness of an otherwise planar surface and it was employed by Techane et al. as a second parameter to optimize results from their simulations.

In the work of Techane et al., satisfactory agreement between the simulated and experimental data required introduction of a CH_2-contamination layer. The signal contribution originating from this ubiquitous contamination layer significantly adds to the

carbon signal from the deeper buried CH_2 shells and was required for good agreement. The impact of the contamination layer on the carbon intensity was studied using SESSA by simply adding or removing an additional hydrocarbon layer on top of the SAM.

We assumed that the gold NPs were perfectly spherical and had a diameter of 14 nm. This choice is based on transmission electron microscopy measurements that gave a size distribution of 14 nm ± 1.5 nm and a circularity (ratio of the major axis to the minor axis of the particles) of 1.09 ± 0.06. 14 The surface density of the $C_{16}COOH$ chains was 0.214 nm^2/chain,[110] which amounts to approximately 2877 chains attached to the surface of a single 14 nm NP. The atomic density within each layer was calculated in a way that, multiplying it by the volume of the shell, gives the total number of atoms occupying the shell, e.g., 2877 sulfur atoms in the innermost shell or 3 × 2877 atoms in each CH_2 shell. This method ensures that the total number of atoms equals the number of chains times the number of atoms per chain.[110] The $C_{16}COOH$ chains were assumed to be immobile and perfectly aligned, so that the only degree of freedom is the tilting angle relative to the normal which could affect the effective thickness of the CH_2 groups. Since the total number of atoms attached to a NP is constant, the tilt of the SAM can be imitated by reducing the thickness of the CH_2 shells and accordingly increasing the atomic density within the shells.

Employing the same approach as Techane et al.,[110] a number of simulations with different CH_2 thicknesses was conducted to find the thickness that provided the best agreement with experimental XPS data. Figure 4.3 displays the normalized photoelectron intensities of each element from the SESSA simulation for CH_2 shell thicknesses ranging from 0.08 nm to 0.11 nm/CH_2 group together with the experimental data. We also show results for one case where the simulation was conducted without the hydrocarbon contamination layer in order to study the impact of this layer. There is generally good agreement between the experimental intensities and the simulated intensities when an additional contamination layer was included. The leftmost bar shows the simulated intensities when the hydrocarbon contamination layer was omitted.

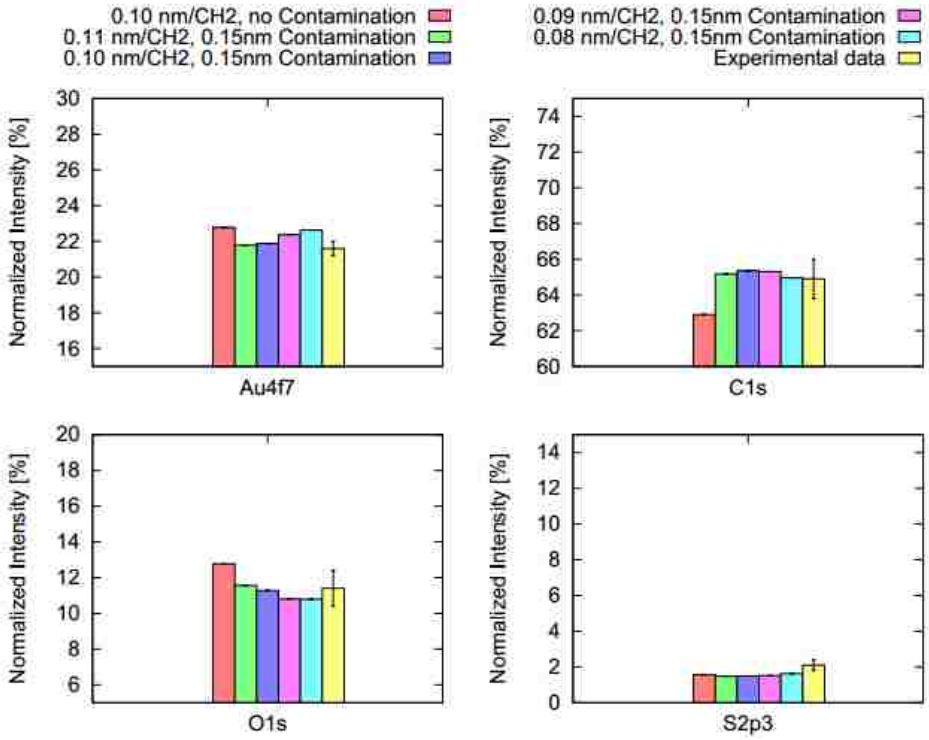

Figure 4.3. Comparison of normalized intensities of the C 1s, Au 4f, O 1s, and S 2p peaks determined by XPS and simulations conducted for different CH_2 shell thicknesses and the presence and absence of a hydrocarbon surface contamination with SESSA 2.0

This omission had a considerable impact on the gold, carbon and oxygen intensities, as they are significantly over- or under-estimated compared to the experiment. Considering the minimal effort to set up and run the simulations, this result shows the capability of SESSA 2.0 in facilitating the simulation of systems composed of NPs. The experimentally determined normalized intensities of the C1s, Au4f, O1s and S2p photoelectron peaks are listed in table 4.2 and compared with results obtained from SESSA 1.3 and SESSA 2.0 for an emission angle of 0◦ relative to the surface normal. To find the shell thickness with the best agreement between the experimentally determined atomic compositions $\%_{i,Experiment}$ and the simulated compositions $\%_{i,SESSA}$, the sum-of-squares difference, ΣX^2, shown in eq. (4.5) was calculated for each case:

$$\sum X^2 = \sum_{i=Au,C,O,S} (\%_{i,SESSA} - \%_{i,Experimental})^2 \qquad (4.5)$$

Figure 4.4 shows the total value for the sum-of-squares difference ΣX^2 and the contributions to ΣX^2 from each element for each CH_2-thickness shown in figure 4.3.

Based on this figure, it is clear that it is necessary to account for the CH_2 contamination layer to obtain results with satisfactory agreement with the experiment.

Compared with SESSA 1.3, the agreement with the experimental data for the carbon, gold and oxygen intensities is matched. The sulfur peak intensity simulated with SESSA 2.0, however, is slightly outside of the experimentally estimated standard deviation range. Based on the resulting sum-of-squares difference ΣX^2, displayed on the right side of figure 4.4, the CH_2-thickness of 0.10 nm and 0.11 nm per CH_2-group and a hydrocarbon contamination layer of 0.15 nm give the best agreement with the experiment. This corresponds to a total film thickness of 2.00 nm and 2.15 nm, respectively, which is close to Techane's result of 1.85 nm.

Table 4.2. Normalized Intensities of the C 1s, Au 4f, O 1s, and S 2p Peaks Determined by XPS Measurements and Simulations with SESSA 1.3[110] and SESSA 2.0 with and without a Surface Hydrocarbon Contamination Layer for an Emission Angle of 0° Relative to the Surface Normal.

		Normalized intensities (%)		
Photoelectron line	Experiment	SESSA 1.3 with cont. layer 0.09 nm/CH_2 group	SESSA 2.0 with cont. layer 0.11 nm/CH_2 group	SESSA 2.0 without cont. layer 0.11 nm/CH_2 group
C1s	64.9 ± 1.1	64.7	65.2	62.9
Au4f	21.6 ± 0.4	21.5	21.8	22.8
O1s	11.4 ± 1.1	11.8	11.6	12.8
S2p	2.1 ± 0.3	1.9	1.5	1.6

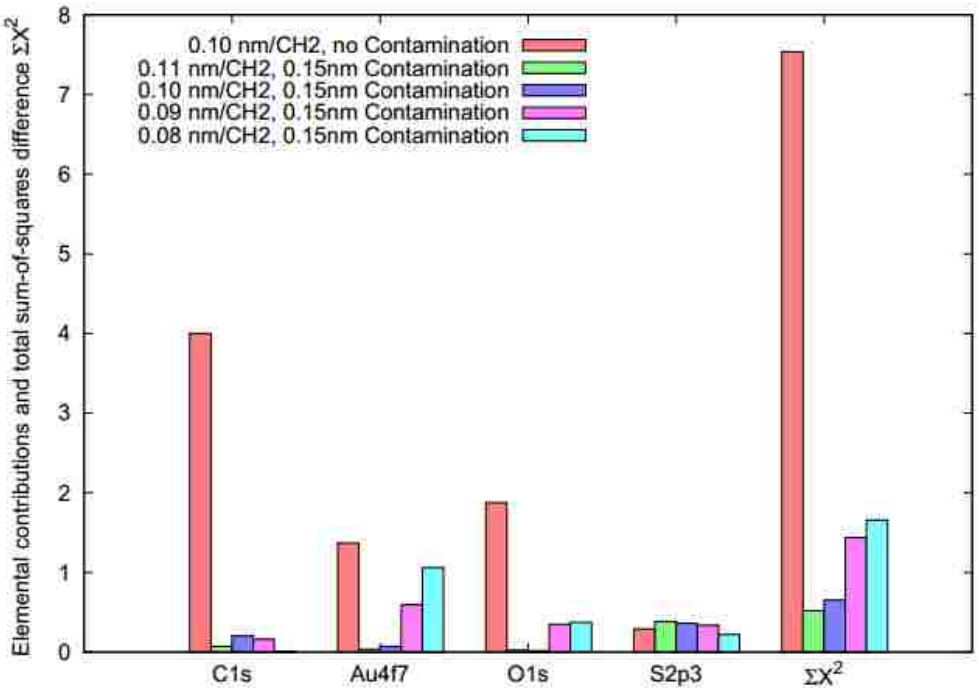

Figure 4.4. Contributions to the sum-of-squares difference for each case depicted in Figure 4.3 and the total sum-of-squares difference $\sum X^2$.

4.4.4 FULL SPECTRAL COMPARISION BETWEEN SESSA AND EXPERIMENT

With SESSA it is not only possible to simulate photoelectron peak intensities but also to simulate entire spectra. This feature of the software was used to conduct a full spectrum match between the measured and simulated spectra of the gold NP SAMs. The transmission function of the XPS apparatus used to record the spectra was estimated.

In contrast to all previously discussed cases where only the elastic (i.e. zero-loss) peak intensities were of interest, the inelastic background also needs to be correctly accounted for.

As shown in a previous work,[126] a single NP is a useful model system for dispersed powders and yields the same elastic-peak intensities. However, the inelastic background obtained from a single NP is significantly different from the inelastic background of a dispersed powder, and a more suitable morphology is needed to reproduce it correctly. Therefore, using external software a PENGEOM geometry of an array of dispersed CS particles resembling a powder was created and simulated with

SESSA to ensure the correct shape of the inelastic background. However, SESSA assumes a constant transmission function, so in order to compare the experimental and simulated spectra with each other, a transmission-function correction needs to be applied to the experimental data. The transmission function was estimated as follows: First, the normalized intensities of the C1s, O1s and Au4f peaks were determined using the experimental spectra.[110] Then, each atomic composition was normalized to the Au4f peak and divided by the transmission-corrected data provided by Techane et al. in the original paper.[110] The sulfur peak was omitted and corrected for since the provided data did not allow us to extract useful data for the minor sulfur peaks. Plotting these elemental ratios for each element gives three points that represent a crude approximation for the transmission function normalized to the Au4f7/2 binding energy of 84.0 eV. In order to validate this result, a second approach was adopted where the experimental and the simulated spectra were divided by one another, followed by fitting a second-order polynomial through the ratio data. The derived function is a crude approximation for the transmission function, given that the differences between the experimental and simulated spectra are most likely due to the energy dependence of the transmission function.

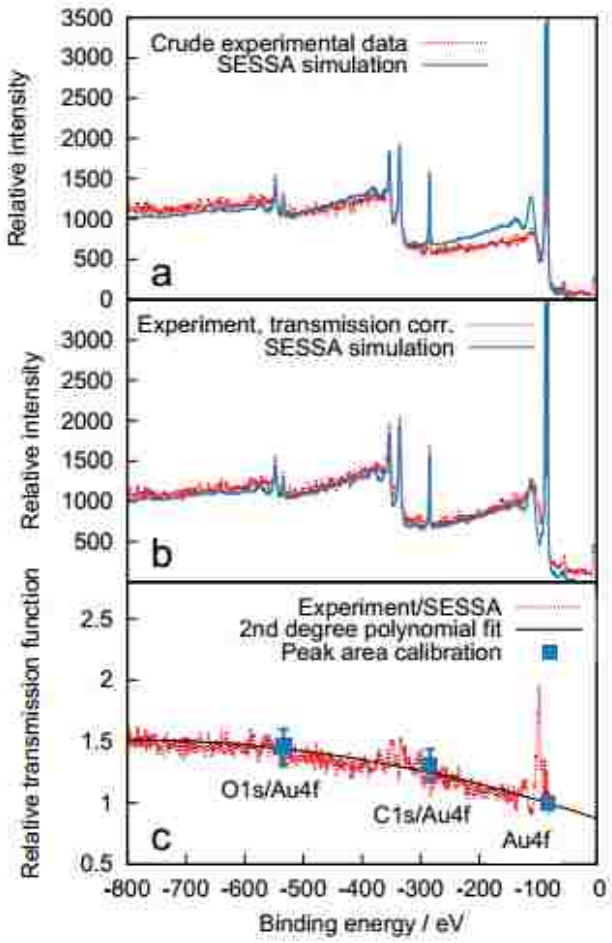

Figure 4.5. Experimental, simulated, and transmission-corrected spectra of $C_{16}COOH$ SAMs on 14 nm gold NPs at an emission angle of 0° relative to the surface normal and the resultant approximation of the transmission function. (a) Comparison of experimental and simulated spectra, both normalized to the C 1s peak. Since SESSA does not account for the transmission function of the experimental setup, the spectra do not match. (b) Comparison of the transmission-corrected experimental spectrum and the simulated spectrum. By fitting a second-degree polynomial to the transmission function and dividing the experimental spectrum by this function, very good agreement is obtained with the experimental spectrum. (c) Display of the transmission function obtained by comparing elemental compositions together with the second-order polynomial fit for the binding-energy range between −800 and −150 eV and by dividing the experimental spectrum by the simulated spectrum.

Figure 4.5.(a) shows the simulated and experimental spectra, where the simulation was normalized to the C1s peak of the experiment. When comparing these spectra the simulated spectrum appears to be skewed relative to the experimental spectrum. This skewness can be partially attributed to the transmission function of the XPS instrument used for the experiment.

Correcting the experimental spectrum for the transmission function yields the spectrum shown in figure 5b, which exhibits a nearly ideal agreement with the simulation. Also, as seen in figure 4.5.(c), the transmission function obtained by comparing the atomic compositions as well as simply dividing one spectrum by the another yields very similar results.

Having an approximate expression for the transmission makes it possible to directly compare the experimental and simulated spectra. Figure 4.6 shows experimental spectra for SAMs on gold NPs (figure 4.6.(a)), SAMs on flat gold (figure 4.6(b)), and the corresponding simulated spectra, all normalized to the Au4f peaks. For comparison a simulated spectrum of a single gold NP (figure 4.6.(c)) is displayed which exhibits a clearly different background shape.

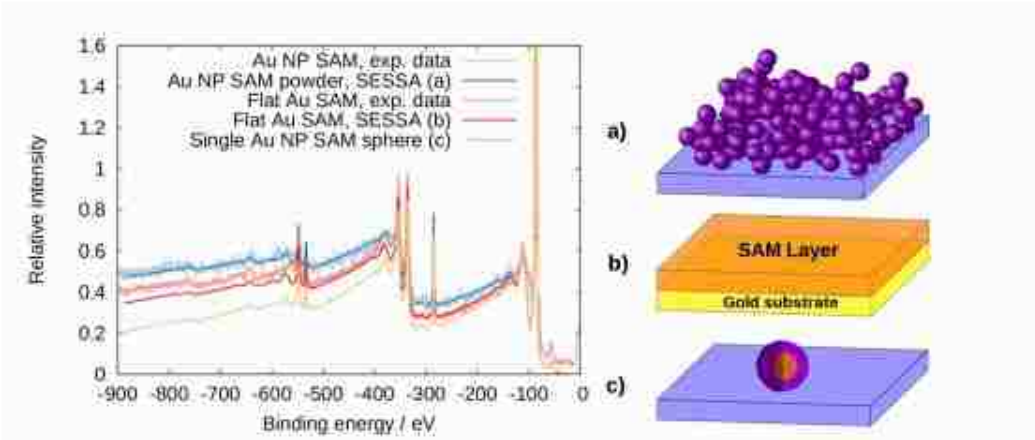

Figure 4.6. Comparison of transmission-corrected, experimental data for SAMs on flat gold and SAMs on gold NPs with the corresponding simulations. Also, the simulated spectrum of a single gold NP is shown. The clear difference in background shapes between the flat geometry and the NP is apparent. In contrast, the single gold NP model correctly predicts the peak-intensity ratio but exhibits a significantly different background shape. The subfigures (a), (b), and (c) are schematic representations of the simulated morphologies: (a) Powder-like arrangement of CS particles; (b) a SAM layer located on a gold substrate; (c) a single CS nanoparticle on an infinite substrate.

The transmission-function correction was essentially derived using the experimental data for gold NPs and the corresponding simulation of a powder-like geometry. The same transmission correction was applied to the experimental spectrum for SAMs on flat gold, again leading to good agreement with the simulation. In general, it can be seen that the background shapes are distinguishable and that SESSA V2.0 is

capable of correctly reproducing the background shape using an externally loaded PENGEOM geometry file, in contrast to the single-particle model, where only the peak-intensity ratios are correctly reproduced.

4.5 CONCLUSION

We have substantially improved SESSA by implementing the PENGEOM package that enables one to simulate different predefined nanomorphologies in addition to the previous functionality to simulate planar samples. Using the T (NP) formula, a comparison of simulated and calculated shell thicknesses of CS NPs was made. The results obtained with SESSA 2.0 are in perfect agreement with the T (NP) formula within the limits of the underlying model which is based on the SLA. With SESSA 2.0, it was very easy to study the limits of the T (NP) formula and it was shown that it is highly suitable for determining shell thicknesses of organic materials but overestimates shell thicknesses for CS particles with strongly scattering shells.

SESSA 2.0 was also applied to a further analysis of experimental data (14 nm gold particles functionalized with an alkanethiol)[110] in which results were previously obtained with SESSA 1.3 and a model in which spherical particles were represented by an array of differently angled surfaces. With the new version of SESSA it was straightforward to allow the radial density to vary. For the total alkanethiol film thickness two values of 2.00 nm and 2.15 nm were found, which both gave equally good agreement with the experimental data, compared to the previous result of 1.85 nm.[110]

Furthermore, we have compared experimental spectra for SAMs on flat gold and SAMs on 14 nm gold NP[110] with simulations. In order to compare experimental spectra with simulations, it was necessary to correct the simulations for the transmission function of the XPS instrument used to measure the experimental spectra. The corrected simulations exhibited very good agreement with the experimental spectra with regard to the shape of the inelastic background, thus showing that SESSA 2.0 is capable of correctly reproducing not only XPS peak intensities but also XPS spectra of dispersed arrays of CS particles. The spectra for SAMs on flat gold and gold NPs were then compared with the spectrum of a single SAM gold NP, which is a model system often employed in XPS. This comparison was conducted to show the significant differences in

the shape of the inelastic background that arise due to the presence of a dispersed array of NPs and which are missing if a single particle is simulated.

4.6 ACKNOWLEDGEMENT

Y.C W. and D.G.C. gratefully acknowledge support from grant EB-002027 from the US National Institutes of Health. Y.C.W. thanks the US National Science Foundation for a Graduate Fellowship.

Chapter 5. SIMULATION OF SELF-ASSEMBLED MONOLAYERS OF DODECANE-, CARBOXYLIC ACID-, AND CARBOXYLIC ACID TERMINATED OLIGO(ETHYLENE GLYCOL)- THIOLS ON FLAT AND NANOPARTICLE SURFACES

Yung-Chen Wang[a], Patrik Johansson[a], and David G. Castner*[a,b]

[a]National ESCA & Surface Analysis Center for Biomedical Problems, Department of Bioengineering, Box 351653, University of Washington, Seattle, WA 98195-1653 USA

[b]National ESCA & Surface Analysis Center for Biomedical Problems, Department of Chemical Engineering, Box 351653, University of Washington, Seattle, WA 98195-1653 USA

*Corresponding Author

David Castner

University of Washington

Department of Bioengineering and Chemical Engineering

Box 351653

Seattle, WA 98195

1-206-543-8094 (phone)

1-206-221-7451 (fax)

castner@uw.edu (e-mail)

5.1 ABSTRACT

The new version of the simulation of electron spectra for surface analysis (SESSA 2.0) was applied to model self-assembled monolayers (SAMs) functionalized on flat gold (Au) and gold nanoparticle (AuNPs) surfaces. Though alkanethiol based SAMs on flat gold surfaces are commonly used and well characterized, the assembly and structure of SAMs on gold nanoparticles remain underexplored. In this work, dodecane-, carboxylic acid-, and carboxylic acid terminated oligo(ethylene glycol)- thiols functionalized on Au surfaces were characterized experimentally using X-ray photoelectron spectroscopy (XPS). The elemental composition obtained by XPS analysis serves as the foundation for the determining overlayer SAMs structure and thickness in SESSA models.

We hypothesized that an accurate model of the each SAMs can be computed with SESSA by combining experimental XPS peak intensities and experimentally characterized structural information in the literature. Variables such as the thickness of adventitious carbon and density of each layer of the SAMs can then be determined by matching the simulated and experimental result. Using this approach, we identified accurate models in SESSA that can describe the SAMs overlayer structure for flat gold surfaces. However, the SAM models developed for flat surfaces does not translate well to AuNPs. As SAMs adopt different structures on AuNPs with high curvature and surface defects, we utilized SESSA to model potential SAMs structure on AuNPs. We show that a good model of carboxylic acid terminated SAMs can be generated by reducing the packing density of SAMs on AuNPs by 70%. However, this approach of reducing SAMs packing density did not provide a good model for the carboxylic acid terminated oligo(ethylene glycol) SAMs. Though SESSA can provide potential models that can describe structurally complicated SAMs, additional structural information is needed to develop better models.

5.2 INTRODUCTION

In recent decades alkanethiol based self-assembled monolayers (SAMs) have attracted considerable interest for surface modification.[138–140] The ability to form well-defined layers with functional headgroups rapidly allows surfaces functionalized with alkanethiol SAMs to control surface chemistries for a wide variety of applications such as sensing, catalysis, and surface modifications.[37,141] Not limited to flat surfaces, alkanethiols were also utilized to synthesize small gold nanoparticles (AuNPs) with diameters of 1 to 3 nm by simultaneously reducing gold salt precursors in the presence of the alkanethiols to stabilize the synthesized AuNPs.[142] Further, SAMs functionalized nanoparticles have historically been used for surface enhanced Raman scattering (SERS),[143,144] drug delivery,[145] and sensing applications.[141]

Though the structure and formation of SAMs on flat surfaces are well understood,[67,94,146–149] detailed characterization on the assembly of SAM covered AuNPs is lacking. SAMs on AuNPs exhibit unique structures that are dependent on the diameter of the particle and the chain length of the alkanethiol.[67,150,151] These structures are often complex and require specialized techniques for their characterization, in contrast to SAMs on flat substrates. Computational techniques such as molecular dynamics (MD) simulations are commonly applied to investigate the formation of SAMs on AuNPs but are limited to structurally simple alkanethiols.[152]

Precise understanding of the structure and surface chemistry of SAM modified AuNPs can provide valuable information for advancing AuNP based sensing and drug delivery applications. In this study, we utilized both X-ray photoelectron spectroscopy (XPS) and computational techniques to characterize the composition and structure of dodecane-, carboxylic acid terminated undecane-, carboxylic acid terminated oligo(ethylene glycol) (OEG-COOH) thiol SAMs on both flat gold and AuNP surfaces. XPS is a surface analysis technique commonly used to characterize SAMs based surface modification on both flat Au and AuNP surfaces.[67,98,134,153] The capability of XPS to provide surface sensitive compositional and chemical state analysis for nanoparticle overlayers makes it an ideal technique for characterizing SAM functionalized AuNPs.

Using the experimental results obtained from XPS, the Simulation of Electron Spectra for Surface Analysis (SESSA) was applied to model SAMs functionalized on flat Au and AuNP surfaces. SESSA can simulate nanostructures with customized compositions through an intuitive graphical user interface (GUI). One big advantage of SESSA is the capability of simulating photoelectron spectra for nanoparticles with overlayers.[62] Even with only limited understanding of the overlayers on a nanoparticle, one can effectively extrapolate information about a nanoparticle's overlayer composition and structure by designing models based on XPS analysis and other analytical techniques that provide structural information about the nanoparticle. In this study, we utilize a new version of SESSA 2.0 to model a series of SAMs with different headgroups on both flat gold and AuNP surfaces. We further utilize experimental sum frequency generation (SFG) spectroscopy analysis to capture the structure of the different SAMs. The version of SESSA used in this study can simulate nanoparticles directly without the need of complex geometrical corrections. Therefore, this study serves as an extension to our group's previous work of simulating carboxylic acid terminated SAMs on flat gold and AuNP surfaces using the older version of SESSA (1.3).[110]

5.3 MATERIALS AND METHODS

5.3.1 SUBSTRATE PREPARATION

Small silicon (Si) wafers were used as substrate for AuNP samples in XPS analysis. Si substrates were prepared from standard 100mm diameter wafers (Silicon Valley Microelectronics, Santa Clara, CA), with a thickness of 525 ± 25um. The Si wafers were diced into 1.1 cm2 squares using the Disco DAD 321 Wafer Dicing Saw in the Washington Nanofabrication Facility (WNF). The diced Si wafers then undergoes a cleaning protocol which consists of an overnight wash in filtered and deionized (DI) water (18.2 MΩ) (EMD Millipore, Billerica, MA), followed by two 15-minutes washes in methylene chloride, two 15-minutes washes in acetone, and two 15-minutes washes in methanol. The cleaned Si wafers were then placed in a dedicated wafer holder, sealed with foil and stored under air at room temperature.

Gold substrates were prepared from the diced and cleaned Si substrates discussed in the previous paragraph. A 5 nm titanium (Ti) adhesion layer followed by a 30 nm Au layer was deposited on top of the Si substrates using the electron beam vapor deposition technique. The Ti adhesion layer improves the bonding between the Au overlayer and the Si substrate, enhancing the physical stability of the gold layer. The deposition was conducted in the WNF using the CHA Industries EVAP (Fremont, CA). The Ti and Au layers were deposited using deposition rates of 2.0 Å and 5.0 Å per second, respectively. The rate and thickness of the metal deposition process were optimized to ensure an even and smooth coverage of the Au layer. The deposition process was monitored by a quartz crystal microbalance within the deposition chamber. After deposition, the Au substrates were backfilled with nitrogen gas, sealed, and stored away from light exposure.

5.3.2 FLAT GOLD SURFACE FUNCTIONALIZATION

Three different alkanethiol based SAMs were used to functionalize the flat gold substrates in this study. A summary of the alkanethiols used and the abbreviation used to describe them is provided in Table 5.1. Both the dodecanethiol and COOH thiol were purchased from Asemblon (Seattle, WA). The OEG-COOH thiol was purchased from Prochimia (Sopot, Poland).

Table 5.1. Summary and abbreviation of alkanethiols

Chemical structure	Alkanethiol abbreviation
HS-C11-CH3	dodecanethiol
HS-C11-COOH	COOH thiol
HS-C11-EG4-O-CH2-COOH	OEG-COOH thiol

A 20mL glass scintillation vial was rinsed with pure 200 proof ethanol (Decon Laboratories, King of Prussia, PA) and then dried in air. The gold substrate was placed inside the cleaned scintillation vial and submerged in ~3mL of a 100uM solution of the target alkanethiol in pure ethanol. The glass vial was then backfilled with nitrogen, sealed, and stored away from light for 36 hours to allow the self-assembly process to go

to completion. After self-assembly, the gold substrate was removed, rinsed with ethanol for 15 seconds and then dried using nitrogen gas.

5.3.3 NANOPARTICLE SYNTHESIS AND FUNCTIONALIZATION

The AuNPs were synthesized using the citrate reduction method, which was first proposed by Turkevich et al.[49] and further developed by Frens.[50] Reagents used includes sodium citrate tribasic dehydrate (Sigma-Aldrich, St. Louis, MO) and gold (III) chloride hydrate (99.999%) (Sigma-Aldrich, St. Louis, MO). First, a 0.01% (w/v) Au solution in deionized H_2O was prepared. The gold solution was then transferred to the round bottom flask and heated to 100°C while stirring under a reflux system. While the Au solution is heating, a sodium citrate stock was prepared by dissolving 285mg of sodium citrate in 25mL of DI H_2O (40mM). As the temperature of the Au solution reaches 100°C, the sodium citrate solution is quickly added into the round bottom flask (2.5% volume of initial gold solution). After 20 minutes, the AuNP solution is removed from the reflux system. The AuNP solution is allowed to sit at room temperature to cool, followed by a nitrogen gas backfill. The AuNPs can then be sealed, foiled, and stored in the refrigerator at 4°C.

To prepare the SAM functionalized AuNPs, the desired amount of AuNPs prepared from the previous paragraph was first transferred to a clean glass container. Thiols dissolved in pure ethanol were then added to the AuNP solution to achieve a final concentration of 100uM. Under stirring, the AuNP containing glassware was sealed and foiled to prevent exposure from light, then left to assemble for 36 hours. After 36 hours, the thiol functionalized AuNPs were sonicated for 30 seconds and subsequently transferred into centrifuge tubes. To purify the AuNPs and remove excess thiols from the AuNP solution, the AuNPs were subjected to centrifugation at 9,000 rpm for 30 minutes. The pellet of the concentrated AuNPs in the bottom of the centrifuge tube was collected, followed by another round of 9,000 rpm centrifugation for 30 minutes on the supernatant solution to collect the remaining AuNPs. To break up the AuNP pellet before each resuspension, the pellet was vortexed for 30 seconds and sonicated for 1 minute. The collected concentrated AuNPs were then transferred to small 1.5mL Eppendorf tubes and re-suspended with 1mL of DI H_2O. These AuNPs were then

centrifuged at 12,000 rpm for 40 minutes. The supernatant was carefully removed and fresh 1mL of DI H_2O was added to re-suspend the AuNPs. The AuNPs were vortexed for 30 seconds and centrifuged again at 12,000 rpm for 40 minutes. After removing the supernatant and backfilling with nitrogen gas, and the concentrated AuNPs were ready for XPS analysis.

5.3.4 SIMULATION OF ELECTRON SPECTRA FOR SURFACE ANALYSIS

Simulation of electron spectra for surface analysis (SESSA) is a standard reference database distributed by the National Institute of Standards and Technology containing all data needed for quantitative simulations of XPS and Auger- electron spectra.[62,63] Data retrieval is based on a powerful expert system that queries the databases and provides the data to the user or the simulation engine for arbitrarily shaped geometrical configurations. The simulation engine is a particularly crucial part of SESSA as it enables the user to conduct batch simulations of arbitrarily shaped nanostructures.

In SESSA 2.0 the following morphologies are predefined and can be chosen: planar, roughness, islands, spheres and layered spheres. The planar morphology can be comprised of an arbitrary number of stratified layers placed on a semi-infinite substrate. The composition and thickness of each layer can be easily changed by the user and SESSA provides estimates for all needed material properties. For the roughness parameter, an additional parameter is defined to account for the increase in relative surface area (RSA) of a rough surface compared to a perfectly planar specimen. The increase in signal intensity due to an increased surface area is accounted for with the RSA parameter. The island and sphere morphologies enable one to simulate structures placed on a planar morphology.

For islands, the simulated structure consists of a trapezoid with variable dimensions in x, y and z directions, together with variable inclinations of the side-walls. In the case of spheres, the dimensions of the sphere and its composition can be varied. The layered-spheres morphology allows one to simulate a spherical particle consisting of an inner core with an arbitrary number of overlayers. The dimensions of the sphere as well as the composition and thickness of each layer can be chosen by the user. All

nanomorphologies are simulated as periodic arrays where the periods can be selected to represent isolated or dense assemblies of particles. As shown in our prior work[21] and by Frydman et al.,[120] the surface of a thick, densely packed film of core-shell nanoparticles seen by the detector is equivalent to the surface of a single sphere and is independent of the viewing angle by the detector. Therefore, a simulation for a densely packed film of core-shell nanoparticles yields the same ratio of photoelectron intensities from the core and the shell as would be obtained from a bulk powder. In this study, nanoparticles are all simulated as a single sphere to represent the densely packed film of nanoparticles.

To minimize computation times and to enable faster processing of batch jobs, a highly efficient Monte Carlo code is employed, based on the trajectory-reversal method of Gries and Werner.[66] In contrast to conventional Monte Carlo codes where electrons are tracked on their trajectories from the source to the detector, the trajectory-reversal approach tracks electrons in the opposite direction, starting from the detector and following the trajectory back to the point of origin. Thus, all electrons contribute to the signal resulting in significantly decreased simulation times, typically in the range from seconds to several minutes, depending on the number of peaks to be simulated and the desired precision in the results. To account for elastic scattering events, all simulations in this study were performed without using the straight-line approximation.

5.3.5 TRANSMISSION ELECTRON MICROSCOPY

The shape and size of the AuNPs were determined using transmission electron microscopy (TEM) analysis. The AuNP sample for the TEM analysis was prepared by drying AuNPs directly onto a carbon-supported TEM grid (Ted Pella, Redding, CA). The AuNP solution was produced by centrifuging 1.5mL of AuNPs under 12,000 rpm for 20 minutes. After removing the supernatant, the AuNPs were resuspended using 0.5mL mixture of 50:50 ethanol and DI H_2O. Ethanol solution was used to accelerate the drying process to prevent particle aggregation. TEM images were taken on FEI Tecnai G2 F20 TEM (FEI, Hillsboro, Oregon) operating with 200kV acceleration of the electron beam and 180kX-245kX magnification. All images were taken at a 2048 x 2048 pixel resolution using the bright field mode. The size and circularity of the AuNPs was

analyzed from the TEM images using particle analysis algorithm in ImageJ (version 1.46d, National Institute of Health, USA).

5.3.6 X-RAY PHOTOELECTRON SPECTROSCOPY

XPS atomic composition data were collected on a Surface Science Instruments S-probe spectrometer equipped with a monochromatized Al Kα X-ray source (*hv* = 1486.6eV). For each sample, spectra were collected from three different regions with a 800 µm x 800 µm spot size, including survey scans from 0-1100 eV binding energy and detail scans (S 2p and N 1s) to calculate the elemental composition and thickness approximation. The survey spectra were collected at 1 eV/step for four scans with a dwell time of 100 ms. The detail S 2p and N 1s spectra were collected at 0.4 eV/step with a dwell time of 100 ms for 32 and 16 scans, respectively. The pass energy for the survey and detail scans was 150 eV. The S-probe data were processed using manufacturer provided sensitivity factors using the *Hawk Data Analysis* software.

Angle resolved XPS analysis were conducted using a Kratos AXIS Ultra DLD (Kratos, Manchester, England). The Kratos XPS is equipped with a monochromatized Al Kα X-ray source. The electrostatic mode was used to collect photoelectrons during angle resolved XPS experiments. The nominal photoelectron take-off angles, defined as the angle between the substrate normal and the axis of the analyzer lens, for the angle resolved experiments were 0˚, 55˚ and 75.5˚. The high-resolution C 1s spectra were collected at 0.1 eV/Step for 32 scans with a dwell time of 300 ms and pass energy of 20eV. For each sample, spectra were collected from three different regions of 300 µm x 700 µm spot size.

5.3.7 ATOMIC FORCE MICROSCOPY

Atomic force microscopy (AFM) was used to characterize the roughness of the Au substrate. The images were collected using a Bruker Dimension ICON in PeakForce mapping mode using a ScanAsyst-Air probe (resonant frequency: 70 KHz, spring constant: 0.4 N/m). Images were collected at 512 by 512 pixels with a scan rate of 1 Hz. To obtain surface roughness, the collected images were analyzed using Gwyddion software.

5.3.8 SUM FREQUENCY GENERATION

The SFG spectra were measured with a picosecond EKSPLA system. The 532 nm visible beam was generated by frequency doubling of a short-pulsed Nd:YAG laser (32 ps pulse width and 50 Hz repetition rate), which also functioned as the pump for an OPG/OPA/DFG system that generated a tunable IR beam. With incidence angles of 65° (visible) and 62° (IR) relative the surface normal, the beams were overlapped on the samples with a spot size of about 0.2 mm^2, where the energies per pulse were 20 μJ for the visible and 100-120 μJ for the IR (depending on the wavenumber). All SFG data were recorded in the ppp polarization combination (SFG, visible, and IR all p-polarized). Each spectrum presented in this work is an average of data from 4 spots (2 spots each from 2 sample replicates), measured with a spectrograph and a photomultiplier tube detector collecting 400 acquisitions per step with an IR step size of 2 cm^{-1}. Before averaging and subsequent data analysis, every data point in the spectra for each spot was power normalized by dividing through the corresponding visible and IR beam energies. In our spectral analyses of the SFG results, we used the following equations to fit the data:

$$I_{SFG} = \left|\chi^{(2)} \cdot E_{\omega Vis} \cdot E_{\omega IR}\right|^2 \qquad (5.1)$$

.

$$\chi^{(2)} = \chi_{NR}^{(2)} + \sum_k \frac{A_k}{\omega_k - \omega_{IR} - i\Gamma_k} \qquad (5.2)$$

where $E_{\omega_{Vis}}$ and $E_{\omega_{IR}}$ are the visible and IR electric fields, $\chi^{(2)}$is the second-order SFG susceptibility, $\chi_{NR}^{(2)}$ is the nonresonant contribution, ω_{IR} is the IR wavenumber. A_k is the amplitude for the kth resonant mode, while the corresponding peak wavenumber and half width are given by ω_k and Γ_k, respectively.

5.4 RESULTS AND DISCUSSIONS

5.4.1 TEM ANALYSIS

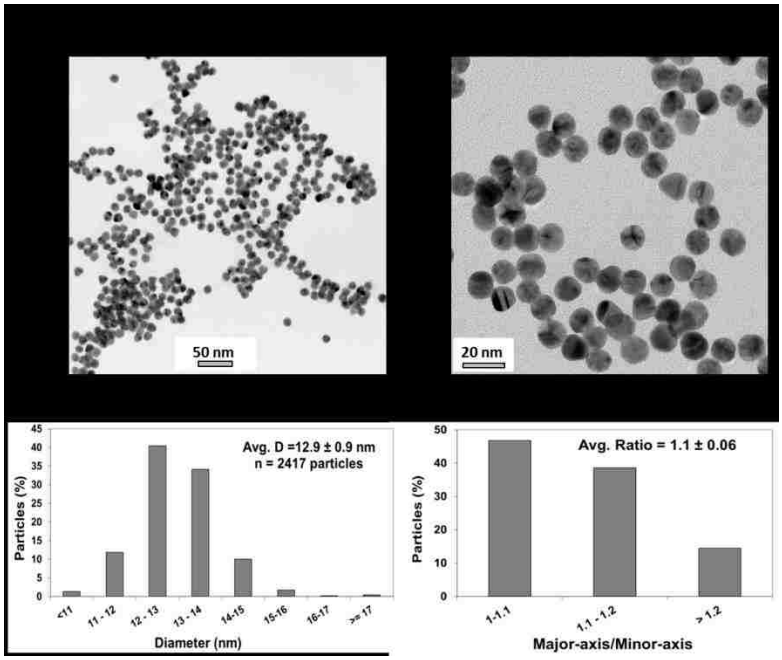

Figure 5.1. (a) and (b) shows TEM bright field images of AuNPs synthesized using the citrate reduction method. The distribution of nanoparticle diameter is shown in (c). It was determined using ImageJ's particle analysis algorithm that the AuNPs had were mostly monodispersed and had an average diameter of 12.9 ± 0.9nm. (d) The ratio of major-axis and minor-axis of the AuNPs were calculated to determine their sphericity. The average AuNPs were overall spherical with a major-axis to minor axis ratio of 1.1.

TEM bright field image and particle analysis for the AuNPs is shown in Figure 5.1. Figure 5.1 (a) and (b) are representative bright field image of AuNPs synthesized via citrate reduction. Image analysis using ImageJ shows that the AuNPs are monodispersed with average diameter of 13nm and a standard size deviation of 0.9nm (n= 2417 particles) (Fgure 5.1(c)). The AuNPs are overall spherical with a major-axis to minor-axis ratio of 1.1 (Figure 5.1(c)). No batch-to-batch inconsistencies regarding the sphericity and size distribution of the particles were observed.

5.4.2 AFM CHARACTERIZATION OF THE FLAT GOLD SUBSTRATE

One important parameter in SESSA simulation is the relative surface area (RSA). This parameter can be modified by the user to adjust the roughness of the simulated flat sample. To obtain experimental value for this parameter, we utilized AFM to measure the surface roughness of the sample. Figure 5.2 shows a AFM image of the flat gold substrate used for SAMs functionalization. In an analysis area of 1.0 µm x 1.0 µm, the average height and surface area of the Au substrate determined by software analysis was 2.05 nm and 1.0061 μm^2 respectively. Since SESSA relies on the RSA factor to account for surface roughness, an RSA factor of 1.006 was used for all simulations of SAMs functionalized flat gold substrates.

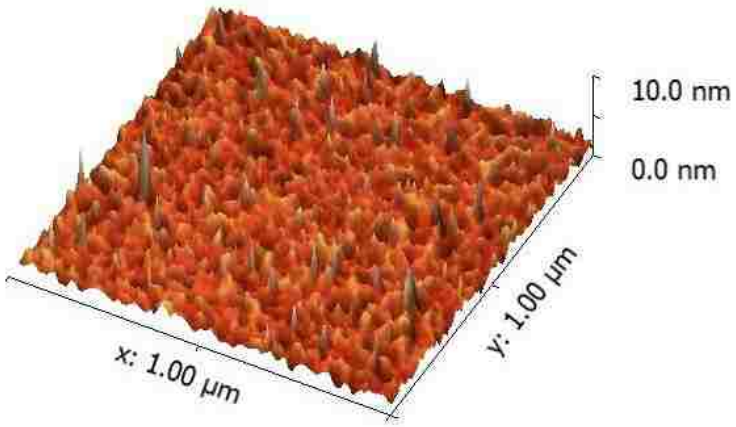

Figure 5.2. Representative AFM image of flat gold substrates used for SAMs functionalization in this study. The gold substrates had an average height of 2.05 nm and an average surface area of 1.0061 μm^2 in an analysis area of 1.0 µm x 1.0 µm.

5.4.3 SFG CHARACTERIZATION OF FUNCTIONALIZED FLAT GOLD

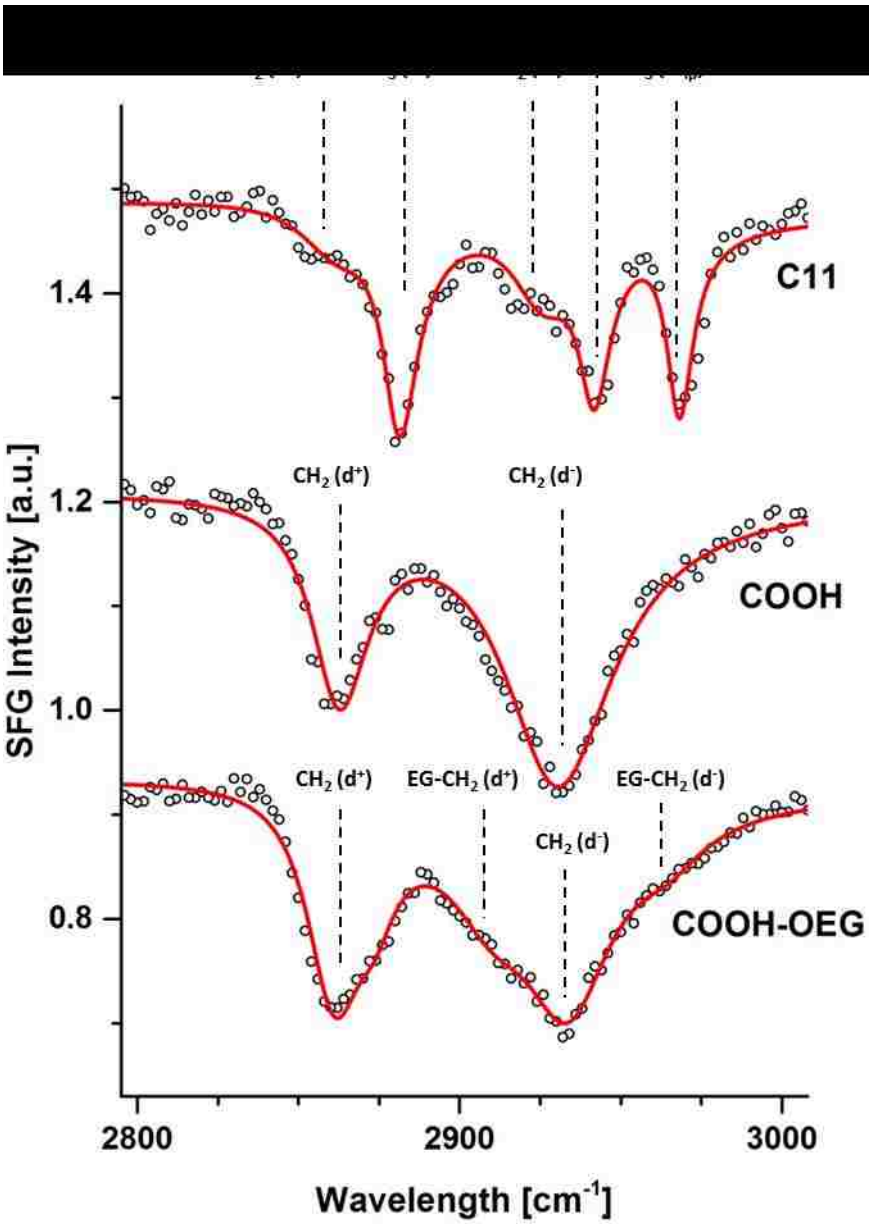

Figure 5.3. Comparison of SFG C-H region spectra of the dodecanethiol (C11), COOH, and OEG-COOH SAMs.

SFG was used to probe the structure of the SAMs on flat gold surface (Figure 5.3). For the dodecanethiol functionalized surface, the bands located at 2880.9 cm^{-1} and 2941.4 cm^{-1} are assigned to symmetric CH_3 modes. The weak bands located at 2860.9 cm^{-1} and 2925.1 cm^{-1} are assigned to CH_2 modes.[154] The presence of the weak CH_2 -peaks indicates potential defects in the methyl chain or CH_2 sites adjacent to the ends

of the chains. Overall, the dodecanethiol SAM is well ordered. For the COOH SAMs, the bands located at 2862.9 cm^{-1} and 2929.9 $cm^{-1}$are assigned to CH_2 modes. The strong CH_2 signals indicate that the COOH SAM is only partially ordered and contain guache defects. The gauche defects are likely caused by the bulky and potentially negatively charged carboxyl functional head groups. Similar to the COOH SAM, the OEG-COOH SAM showed significant CH_2 peaks at 2858.5 cm^{-1} and 2933.1 cm^{-1}. Only very weak signals were observed for the EG-CH_2 peaks at 2909.4 cm^{-1} and 2964.6 cm^{-1}, indicating that the main contributor of the CH_2 defects is the alkane layer rather than the OEG layer. Interestingly, a previous SFG study found an OEG-CH_3 SAM adsorbed onto gold was highly ordered.[155] In contrast to the highly ordered OEG-CH3 SAM, the OEG-COOH SAM's charged and bulky headgroup are likely the cause of the disordered SAM.

5.4.4 XPS CHARACTERIZATION OF FUNCTIONALIZED FLAT GOLD AND GOLD NANOPARTICLES

Table 5.2 summarizes the XPS analysis result of SAMs functionalized flat gold and AuNP surfaces. The analysis result of the bare gold and AuNPs (unfunctionalized) are also provided. The bare flat gold sample was found to have a small amount of carbon, which likely originated from adventitious hydrocarbon due to air exposure prior to XPS analysis. Dodecanethiol functionalized surfaces exhibits the expected carbon and sulfur signals from the SAMs along with an Au signal originated from the Au substrate. A varying degree of oxygen signal was detected from both the COOH and OEG-COOH thiol SAMs. Comparing the COOH and OEG-COOH SAMs on the flat Au surfaces, the OEG-COOH SAMs were found to have ~2x higher oxygen concentrations and a significantly decreased Au concentration compared to the COOH SAMs. These observations were expected as OEG-COOH SAM contains more oxygen atoms (higher oxygen signal from the overlayer) and is thicker than the COOH SAM (more attenuation of the Au substrate signal). Further, the carbon/oxygen ratio of the COOH SAMs (5.8) and OEG-COOH SAMs (2.7) are comparable to the theoretical carbon/oxygen ratio of the COOH thiol (5.5) and OEG-COOH thiol (3). The slight differences between the experimental and the theoretical ratios can be explained by potential hydrocarbon

contamination and the distribution of carbon and oxygen atoms in the SAMs. The SAMs were exposed to air prior to XPS analysis, which could potentially contaminate the sample with adventitious hydrocarbon. Also, the depth distribution of the carbon and oxygen atoms differs in the two SAMs, which affects the of signal attenuation for the carbon and oxygen photoelectrons.

Table 5.2. XPS elemental composition of SAMs functionalized flat gold and AuNPs by the axis of the analyzer lens along with surface normal of the Si wafer substrate. The dodecanethiol functionalized AuNPs were not analyzed due to difficulties during sample preparation. (n.d. = not detected)

		XPS atomic %				
Sample type	SAMs	C 1s	O 1s	S 2p	Au 4f	Na 1s
Flat gold	Bare gold	16.5 ± 2.0	n.d.	n.d.	83.5 ± 2.0	n.d.
	Dodecanethiol	50.8 ± 1.9	n.d.	2.2 ± 0.6	47.0 ± 1.4	n.d.
	COOH thiol	48.4 ± 2.1	8.4 ± 1.0	2.1 ± 0.4	41.2 ± 2.4	n.d.
	OEG-COOH thiol	46.7 ± 0.8	17.1 ± 0.4	1.4 ± 0.3	34.8 ± 0.3	n.d.
AuNPs	Bare AuNPs	34.6 ± 4.3	15.1 ± 4.4	n.d.	46.7 ± 6.3	3.2 ± 1.5
	Dodecanethiol	not available				
	COOH thiol	52.7 ± 3.5	10.0 ± 1.7	2.9 ± 0.7	34.4 ± 3.3	n.d.
	OEG-COOH thiol	57.0 ± 0.9	21.7 ± 1.4	1.7 ± 0.3	19.6 ± 0.8	n.d.

For citrate stabilized AuNPs (unfunctionalized bare AuNPs), gold signal from the AuNPs and the carbon, oxygen and sodium signals from the sodium citrate layer were detected. Due to the difficulty in producing hydrophobic SAMs on AuNPs in aqueous solution, the dodecanethiol functionalized AuNPs were not characterized because the AuNPs aggregated and crashed out of the solution during the functionalization process. Similar for flat gold samples, elements associated with alkanethiol were detected by XPS for the COOH and OEG-COOH thiol functionalized AuNPs. Compared to the COOH SAMs, AuNPs functionalized with OEG-COOH SAMs were found to have a higher oxygen concentration and increased attenuation of the gold signal. The carbon/oxygen ratio for both the COOH SAMs (5.2) and OEG-COOH SAMs (2.6) are both smaller compared to the theoretical ratio (5.5 and 3). Again, the slightly smaller ratio could be explained by the distribution of oxygen atoms in the SAMs.

Though the same SAMs were used for the flat gold and AuNP surfaces, the XPS analysis indicates differences in the composition. This is not surprising due to the size of

AuNPs used in this study. In a typical XPS experiment for a thin film on a flat substrate, the photoelectron is collected from a narrow range of photoelectron take off angles that depends on the acceptance solid angle of the analyzer lens. However for nanoparticles, XPS signal is collected from all photoelectron take-off angles.[120] We can probe the effect of photoelectron take-off angles by comparing the atomic ratio of carbon from the SAMs overlayer to Au from the substrate. The COOH and OEG-COOH SAM functionalized flat gold surfaces have C/Au atomic ratios of 1.2 and 1.3, respectively. The COOH and OEG-COOH SAM functionalized AuNPs have C/Au ratios of 2.9 and 1.6, respectively. The increase in the C/Au atomic ratios for the AuNPs can be explained by the relative increase of the overlayer SAMs signals due the increased range of photoelectron take-off angles detected from the AuNPs. This observation is consistent with previous investigations of alkanethiol functionalized flat gold and AuNP surfaces.[67]

High-resolution XPS scans were also used to characterize the OEG-COOH SAMs on the flat gold surface. Compared to the other two SAMs, the structure and composition of the OEG-COOH thiol is more complicated and understanding the structure of the flexible OEG layer and the carboxylic acid headgroup will help develop a better model in SESSA. For this study, we used angle resolved XPS (ARXPS) analysis to probe the carboxylic acid distribution in the OEG-COOH SAMs on flat Au surfaces. ARXPS is a non-destructive depth profiling technique commonly used to characterize changes in the composition or chemical of states of a thin sample. ARXPS can be achieved by simply tilting the sample stage with respect to the analyzer lens axis, which varies the sampling depth of XPS.[55] The COOH is the headgroup of the SAMs, therefore if the SAMs assembled in a well-ordered fashion on flat gold surfaces, the COOH headgroup should be localized near the surface of the SAMs.

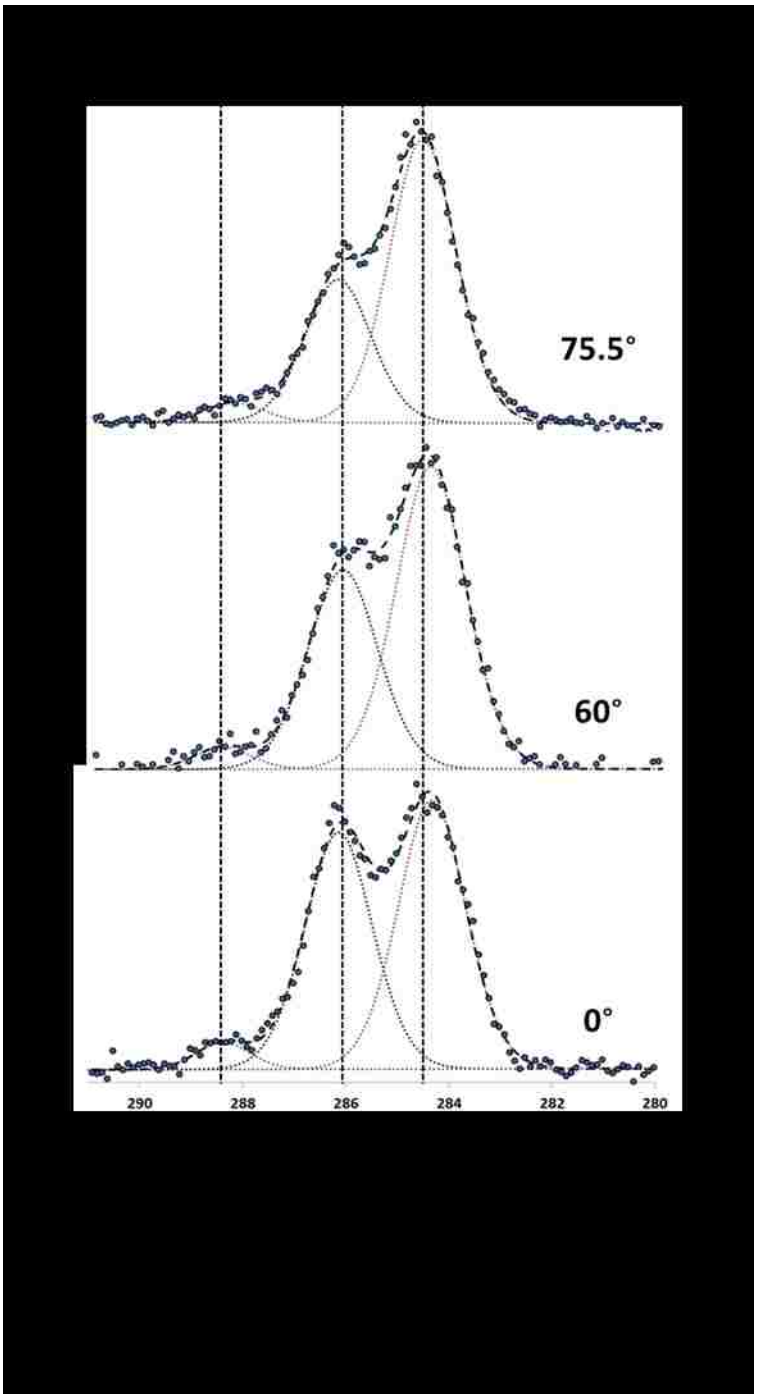

Figure 5.4. ARXPS high-resolution C1s analysis of OEG-COOH SAM functionalized flat gold surfaces with sample tilted at angles of 0°, 60°, and 75.5°. To quantify the chemical states of the carbon species in the SAMs, the high-resolution C1s spectra was fit with C-C/C-H at 284.5 eV, C-O at 286.1 eV, and O-C=O at 288.1 eV. The quantified concentrations of the carbon species are provided.

Figure 5.4. shows the normalized high-resolution C1s ARXPS spectra from the OEG-COOH SAM on flat gold at photoelectron take-off angles of 0°, 60°, and 75.5°.

Effectively, the sampling depth is reduced by ~50% and ~25% at photoelectron take-off angles of 60° and 75.5° relative to a photoelectron take-off angle of 0°. The high-resolution C1s spectra were fit with peaks for the three different carbon species in the SAM: C-C/C-H at 284.5 eV, C-O at 286.1 eV, and O-C=O at 288.1 eV. Interestingly, we did not observe significant differences in the relative concentrations of the COOH species among the different tile angles. It was expected to see a change in the relative ratio of the different carbon species at the different take-off angles if the COOH head group is exposed at the surface of the OEG-COOH SAM. Also, we observed a slight decrease in the O-C-O species and an increase in C-C/C-H species. This indicates that O-C-O species originated from the OEG group are not localized on in the outer layer of the SAM. Therefore, the ARXPS results suggest that the COOH and OEG species are not localized in the outermost layer of the SAM. Further experiments are necessary to more precisely determine the structure of the ethylene glycol and the carboxylic acid layer for the OEG-COOH thiol.

5.4.5 SESSA SIMULATION OF FUNCTIONALIZED FLAT GOLD SURFACES

After experimentally characterizing the SAM functionalized flat gold surfaces. We constructed models in SESSA for the dodecanethiol, COOH-thiol, and OEG-COOH thiol SAMs. The model was constructed in a layer by layer fashion in SESSA, based on the molecule structure of each SAMs. For all SAMs, a layer of sulfur was created right above the flat gold substrate, followed by the appropriate number of individual methylene layers and different headgroups. The thickness of the sulfur layer was modeled based on the literature bond length value.[152,156] The thickness of individual methylene layers was based on theoretical calculated value of 1.1Å derived from chemical bond length of SAMs[157] while taking into account a 30° tilt of the SAMs due to the van der Waals interactions of the methyl groups in hydrocarbon chains.[146,147] Based on a previous electron diffraction study of the ordered sulfur lattice ((√3x√3)R30°) for SAMs on Au(111) surfaces, the SAMs modeled in this study had a density of 21.4$Å^2$/thiolate.[147]

Using SAM models based on literature thickness and density values for alkanethiol SAMs on flat Au substrates, the SESSA simulated XPS results of

dodecanethiol SAMs shows good agreement to the experimentally determined XPS result (Table 5.3). The sum of root mean square deviation (ΣRMSD) was used to evaluate the quality of fit of the simulated result. The smaller the ΣRMSD, the better the fit. An additional variable introduced to the simulation is the thickness of an adventitious hydrocarbon overlayer. Without the introduction of the adventitious hydrocarbon overlayer, SESSA underestimates the amount of carbon while overestimates the amount of gold relative to the experimental XPS results. The increase in thickness of the hydrocarbon layer increases the simulated carbon signal while attenuating the gold signal. With a hydrocarbon thickness of 2.0Å, we were able to achieve good agreement between the simulated result and the experimental XPS result. After the 2Å hydrocarbon layer is included, the total SAMs overlayer thickness in the SESSA model is 16.9Å. This result is comparable to 16.1 Å, the thickness calculated from a formula derived from experimental ellipsometry analysis of alkanethiol SAM on gold (1.5_n - 1.9Å).[157]

Table 5.3. Comparison of experimental XPS result and SESSA simulation of dodecanethiol functionalized flat gold surface with varying amount of hydrocarbon contamination. The sum root mean square deviation (ΣRMSD) value indicates the simulated elemental composition (%) for all elements compared to the experimental XPS result.

		XPS atomic %			
dodecanethiol	**Hydrocarbon(Å)**	C 1s	S 2p	Au 4f	ΣRMSD
SESSA	0.00	46.0	3.3	50.8	3.57
	0.50	47.1	3.2	49.7	2.69
	1.00	48.1	3.2	48.8	1.95
	1.50	49.3	3.1	47.6	1.08
	2.00	50.4	3.0	46.6	0.57
	2.50	51.4	3.0	45.6	0.99
Experimental		50.8 ± 1.9	2.2 ± 0.6	47.0 ± 1.4	

A similar model was built in SESSA for the COOH thiol functionalized flat gold surface. The distinction between the COOH thiol and dodecanethiol is the addition of the carboxylic acid head group. Initial simulations were first performed to determine the thickness of the COOH layer. We found that a COOH layer thickness of 1.6Å provides

good agreement to the experimental XPS oxygen signal. Table 5.4 summarizes the impact of hydrocarbon contamination layer for the COOH thiol SAMs. Compared to the model of dodecanethiol SAMs, a thinner layer of hydrocarbon contamination is predicted for the COOH thiol SAMs. This result is surprising as the free energy of the COOH headgroup is larger than the methyl surface from dodecanethiol, which should result in a thicker contamination layer. In the SESSA model, the total overlayer thickness including the 0.25Å hydrocarbon layer is 14.6Å. Based on ellipsometry study of carboxylic acid SAMs on gold surface (1.16_n + 4.8Å),[33] the overlayer thickness for the COOH thiol used in this study would be 16.4Å. Compared to the ellipsometry thickness, the SESSA model is underestimating the thickness by about 2Å. The discrepancy can be attributed to the uncertainty of the experimental XPS analysis and the ellipsometry formula. Even slight variation in the carbon or gold XPS concentration can significantly impact the SESSA overlayer model. In the ellipsometry study, a constant refractive index independent of CH_2 chain length was used to calculate the SAM thickness. Further, the ellipsometry formula of 1.16Å per CH_2 group more closely resembles a SAM sample tilt of 25° compared to 30° used in the current SESSA model.[10] If the SAM tilt is set to 25° in SESSA, the SAMs overlayer thickness including an optimized hydrocarbon layer of 0.5Å is 15.4Å. The result of this model only differs from the experimental ellipsometry result by 1Å.

Table 5.4. Comparison of experimental XPS result and SESSA simulation of COOH thiol functionalized flat gold surface with varying amount of hydrocarbon contamination. The ΣRMSD value indicates the simulated elemental composition (%) for all elements compared to the experimental XPS result.

		XPS atomic %				
COOH thiol	**Hydrocarbon (Å)**	C 1s	S 2p	O 1s	Au 4f	ΣRMSD
SESSA	0.00	40.4	3.1	8.3	48.3	0.64
	0.25	40.7	3.1	8.2	47.9	0.59
	0.50	41.5	3.0	8.1	47.4	0.72
	0.75	42.1	3.0	8.0	46.9	1.00
	1.00	42.6	3.0	7.8	46.6	1.24
Experimental		41.4 ± 2.4	2.1 ± 0.4	8.4 ± 1.0	48.4 ± 2.1	

A different model can potentially explain the discrepancy between the simulated and experimentally estimated thickness of the COOH-SAMs. In the previous model, the SAMs were assumed to be well-ordered and with consistent 30° tilt angle. However, SFG analysis of the COOH SAMs (figure 5.3) showed that the COOH SAMs is not well-ordered. One way to model a disordered SAMs is to reduce its density while maintaining the overall SAMs thickness and not reducing the effective tilt angle. The result of this SESSA model is shown in table 5.5. The 100% density is defined by the 21.4Å^2/thiolate as discussed in the previous section. As the SAMs packing density decreases, a thicker hydrocarbon layer is required to compensate for the reduced carbon signal. For example, at 80% density, a hydrocarbon layer thickness of 2.0Å is necessary. As the thickness of the SAMs are retained in this model, the addition of the hydrocarbon layer brings the overall SAMs thickness to 16.3Å, which is comparable to the ellipsometry estimated thickness of 16.4Å.

Table 5.5. ΣRMSD value of between the experimental XPS result and SESSA simulation of COOH thiol functionalized flat gold surface by varying both the density of the SAMs and the thickness of the hydrocarbon contamination layer. The ΣRMSD value indicates the simulated elemental composition (%) for all elements compared to the experimental XPS result.

		Alkanethiol SAMs density			
	ΣRMSD	80%	85%	90%	100%
Hydrocarbon (Å)	0.00	2.63	1.78	1.09	0.64
	0.50	2.53	1.85	1.29	0.72
	1.00	1.99	1.57	0.67	1.24
	1.50	0.99	0.55	0.76	2.00
	2.00	0.55	0.76	1.29	2.60

The model for the COOH-OEG thiol SAM is more complicated compared to the previous two SAMs. Both dodecanethiol and COOH thiol consist of well-defined structures and therefore can be modeled easily. In contrast, the COOH-OEG thiol is considerably thicker and contains flexible ethylene glycol chains. As shown earlier, the ARXPS analysis of the OEG-COOH SAMs demonstrated a potential mixing of the outer most OEG and COOH groups in the SAM. To gain insight into the structure of the COOH-OEG SAMs, we simulated two different SESSA models with either a well-

defined layer by layer structure (Figure 5.5.a) or an intermixing of the carboxylic head group with the OEG units (Figure 5.5.b). For the OEG group without intermixing with the COOH layer, a wide range of thicknesses and densities were simulated based on the experimentally determined OEG structure.[94] For the mixed OEG layer, a range of possible thicknesses and densities were simulated based on composition of the layer. For both models, a range of adventitious hydrocarbon layers were applied to account for the potential contamination.

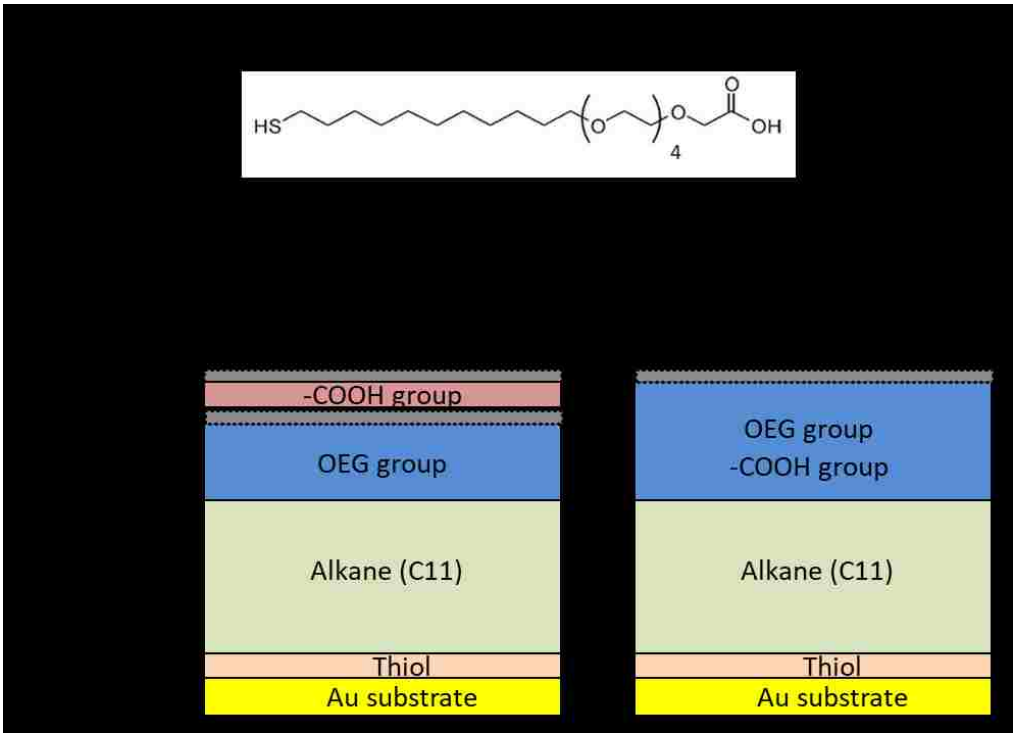

Figure 5.5. (a) The molecular structure of the OEG-COOH thiol. (b) A SESSA model of the OEG-SAMs with well-defined layer by layer structure with no intermixing between each layer. (c) A SESSA model that describes a potential structure of the OEG-COOH SAMs with the COOH headgroup intermixing with the OEG chains.

Table 5.6. ΣRMSD value of between the layer by layer model simulated by SESSA and the experimental XPS result of OEG-COOH SAMs on flat gold. The thickness of hydrocarbon contamination layer and the density of the OEG layer was adjusted to fit the SESSA model to the experimental result. The literature density of the OEG layer (~ 1.20E23) is highlighted.

		OEG layer density (atoms per cm^3)				
		(literature density)				
	ΣRMSD	1.00E23	1.10E23	**1.20E23**	1.30E23	1.40E23
Hydrocarbon (Å)	0.00	1.20	1.36	1.66	2.08	2.67
	0.25	1.45	1.61	2.04	2.45	2.93
	0.50	1.70	1.84	2.20	2.68	3.06
	0.75	1.85	2.10	2.46	2.86	3.32
	1.00	1.97	2.28	2.63	2.08	2.67

Table 5.6 summarizes the SESSA simulation result for the well-defined layer by layer model described in Figure 5.5.(b). The table shows the ΣRMSD value between the SESSA simulation and the experimental result using a range of OEG layer densities and hydrocarbon overlayer thicknesses. To investigate the structure of the OEG layer, the thickness of the OEG chains was set to the literature value (2.78Å per EG group).[94] The "literature" volume density of the OEG region of 1.20E23 is calculated using literature OEG thickness and surface spacing of the thiol molecules in SAMs on gold.[147] This model built using the literature OEG-COOH SAMs structural parameters was able to predict the XPS elemental composition with acceptable accuracy. For example, the SESSA simulation using the literature density and no hydrocarbon contamination layer yields a ΣRMSD value of 1.66, which means the total simulated elemental composition only deviates by ~2% from the experimental XPS result. Reducing the OEG layer density further can improve the fit as the ΣRMSD value decreases to 1.20 when the density of the OEG region is decreased to 1.00E23. It is possible to relax the overall SAM density reach near perfect agreement for the simulated model and the experimental XPS result. However, without additional experimental characterization to probe the structure of the SAMs, we risk overfitting our model.

The second model in which the OEG layer is intermixed with the outer COOH headgroup (Figure 5.5.(c)) was also evaluated. Similar to the previous model, the

thickness of the OEG layer is kept constant while the density of the OEG layer and the thickness of the hydrocarbon contamination is varied. This model, compared to the previous well-defined layer by layer model of the OEG-COOH layer, does not provide as good of fit to the experimental XPS result (Table 5.7). The highlighted density of 1.15E23 is the estimated density of the atoms in the mixed OEG-COOH layer. The higher ΣRMSD values indicate larger deviation of the simulated result to the experimental result, suggesting that the intermixed OEG-COOH model is less likely. Similar to the previous model, the intermixed model consistently overestimates the carbon signal while underestimating the gold signal. Again, reducing the thickness or density of the SAMs can result in a model that can better fit the experimental model. However, additional experiments that can provide more structural information about the SAMs is needed.

Table 5.7. ΣRMSD value of between the intermixing model simulated by SESSA and the experimental XPS result of OEG-COOH SAMs on flat gold. The OEG layer and the COOH layer are intermixed. The estimated density of the mixed OEG layer (1.15E23) is highlighted.

		Intermixed OEG layer density (atoms per cm^3) (estimated density)				
	ΣRMSD	1.05E23	1.10E23	**1.15E23**	1.20E23	1.25E23
Hydrocarbon (Å)	0.00	2.38	2.83	3.26	3.73	4.04
	0.25	2.51	2.90	3.35	3.61	4.08
	0.50	2.68	2.96	3.36	3.76	4.17
	0.75	2.81	3.19	3.54	3.89	4.21
	1.00	2.96	3.31	3.73	4.02	4.33

5.4.6 SESSA SIMULATION OF FUNCTIONALIZED GOLD NANOPARTICLES

We apply the new capability of SESSA 2.0 to simulate nanoparticles to model SAM functionalized AuNPs. As discussed earlier, attempts to functionalize AuNPs with dodecanethiol resulted in the nanoparticles to aggregate and crash out of the solution. Therefore, we only modeled the COOH and OEG-COOH functionalized AuNPs.

Table 5.8. summarizes the SESSA simulated XPS results for COOH functionalized AuNPs. Similar to simulations for flat SAMs simulations, we first based

our simulation model on the theoretical SAMs structure. We applied the same thickness and density parameters used in the flat SAMs simulations to the nanoparticle model simulations. Though it is unlikely that SAMs will adopt the same structure on AuNPs with large curvature and various surface defects, we utilize this theoretical model as the foundation for our simulations. In this model with literature flat SAMs packing density, the SESSA model drastically overestimate the overlayer signal as shown by the high carbon atomic % and low gold atomic %. Though it is not surprising that the flat SAMs model does not produce good agreement for SAMs on AuNPs, we could estimate the impact of the nanoparticle's surface defects on SAMs assembly. Early experimental investigations have shown that SAMs on AuNPs are at least as ordered as SAMs on flat surfaces.[28–30] A more recent scanning tunneling microscopy (STM) investigation on the ligand packing of alkanethiols concluded that the SAMs adopts a slightly relaxed formation (reduced density) to compensate for the high-energy defects and particle curvature while retaining order.[31] Considering the possibility that SAMs on AuNPs remained ordered on the low index facets but adopt a lower density due to the presence of the edge and corner atoms between the low index facets, the COOH-SAMs on AuNPs were modeled with reduced packing density while retaining the thickness of the SAMs. After gradually reducing the packing density, we found good agreement between the SESSA simulated atomic composition and the experimental result when the SAMs packing density is reduced to 70% with a thin layer of hydrocarbon contamination layer.

Table 5.8. SESSA simulated result of COOH SAMs functionalized AuNPs using either the packing density of SAMs on flat gold surfaces and a model of 70% SAMs packing density. The thickness of hydrocarbon layer was varied to probe potential contamination.

		XPS atomic %				
COOH-SAMs	Hydrocarbon (Å)	C 1s	O 1s	S 2p	Au 4f	ΣRMSD
Flat packing density	0	65.1	9.1	2.8	23.1	8.4
	0.75	65.4	8.7	2.8	23.2	8.5
	1.50	66.3	8.1	2.7	22.9	9.0
70% packing density	0	52.5	11.4	2.9	33.2	0.9
	0.75	54.6	10.5	2.8	32.2	1.5
	1.50	56.1	10.1	2.7	31.1	2.3
Experimental		52.7 ± 3.5	10.0 ± 1.7	2.9 ± 0.7	34.4 ± 3.3	

Lastly, the OEG-COOH SAM functionalized AuNPs are characterized using SESSA. Given the limited understanding about the structure of the OEG-COOH layers on AuNPs, first it was assumed the OEG-COOH SAMs assemble onto AuNPs with the same packing density as the flat Au surface in a well-defined layer by layer SAM. Table 5.9 summarizes the SESSA simulation results for the well-defined layer by layer model described in Figure 5.5.(b) on AuNPs. The table shows the ΣRMSD value between the SEESA simulations and the experimental results using a range of OEG layer densities. It is immediately apparent that the SESSA model based on OEG-COOH SAMs on flat gold surface results cannot adequately describe OEG-COOH SAMs on AuNPs, as evident from the large ΣRMSD values. By assuming the OEG-COOH SAMs on AuNPs are slightly less packed compared to their flat SAMs counterpart, we show in Table 5.10 the impact of reducing the overall SAMs packing density for the well-defined layer by layer SAMs. Interestingly, decreasing the packing density of SAMs did not result in a better fit. With this decreased density model, the previously overestimated carbon signal approaches the experimental result. However, the gold signal that was previously underestimated did not increase enough to fit the experimental gold atomic %. Though the model using reduced SAMs packing yielded good result for the COOH-SAMs on AuNPs, it is not by itself an adequate model for describing OEG-COOH SAMs on AuNPs for the case of the well-defined layer by layer model.

Table 5.9. ΣRMSD value of between the layer by layer model simulated by SESSA and the experimental XPS result of OEG-COOH SAMs on AuNPs. The thickness of hydrocarbon contamination layer and the density of the OEG layer was adjusted to fit the SESSA model to the experimental result. The literature density of the OEG layer (~ 1.20E23) is highlighted.

		Intermixed OEG layer density (atoms per cm^3)				
		(literature density)				
	ΣRMSD	1.00E23	1.10E23	**1.20E23**	1.30E23	1.40E23
Hydrocarbon (Å)	0.00	7.3	7.0	7.4	8.0	7.9
	0.25	6.7	7.6	7.8	7.4	7.4
	0.50	6.7	7.1	7.7	7.3	7.5
	0.75	6.8	7.4	7.6	7.4	7.7
	1.00	7.0	7.1	7.3	7.7	7.8

Table 5.10.SESSA simulated result of OEG-COOH SAMs functionalized AuNPs using either the packing density of SAMs on flat gold surfaces and a model of 70% SAMs packing density. The thickness of hydrocarbon layer was varied to probe potential contamination.

		XPS atomic %				
COOH-SAMs	Hydrocarbon (Å)	C 1s	O 1s	S 2p	Au 4f	ΣRMSD
Flat packing density	0	63.5	24.9	4.7	6.9	7.4
	0.75	64.8	23.9	4.5	6.9	7.6
	1.50	67.0	22.5	4.1	6.5	8.3
70% packing density	0	55.3	31.7	4.1	8.9	7.4
	0.75	58.1	28.6	4.1	9.1	6.4
	1.50	59.6	27.5	4.0	8.8	6.4
Experimental		57.0 ± 0.9	21.7 ± 1.4	1.7 ± 0.3	19.6 ± 0.8	

5.5 CONCLUSION

In this work, XPS was used to characterize the composition of dodecane-, COOH-, and OEG-COOH thiol SAMs on both flat gold and AuNP surfaces. The XPS simulation software SESSA was used to model these SAMs with varying headgroups and chain lengths. For the flat gold surfaces, accurate models of each SAMs can be computed with SESSA by combining experimental XPS compositions and experimentally determined structural information from the literature. Utilizing SESSA, we

can further estimate the amount of hydrocarbon contamination on the different SAMs modified surfaces. For AuNPs with small low index facets and significant densities of edge and corner atoms, the structural models of SAMs used for flat surfaces do not provide satisfactory fits to the experimental results. A good model of COOH thiol SAMs can be generated by reducing the packing density of SAMs on AuNPs by 70%. However, this approach of reducing SAMs packing density did not provide a good model for the OEG-COOH SAMs. The two models tested with either a well-defined layer by layer or intermixing of the OEG-COOH layer does not provide an accurate fit to the experimental result. Additional experimental or computational structural characterizations of the OEG-COOH SAMs on AuNPs is needed to establish an accurate SESSA model.

5.6 ACKNOWLEDGEMENT

Y.-C. Wang and D.G. Castner gratefully acknowledge the support from National Institutes of Health grant EB-002027 to NESAC/BIO from the National Institute of Biomedical Imaging and Bioengineering. Part of this work was conducted at the Molecular Analysis Facility, a National Nanotechnology Coordinated Infrastructure site at the University of Washington that is supported in part by the National Science Foundation (grant ECC-1542101), the University of Washington, the Molecular Engineering & Sciences Institute, and the Clean Energy Institute. Y.-C. Wang was supported by the National Science Foundation Graduate Research Fellowship Program under Grant No. DGE-1256082.

Chapter 6. QUANTIFYING THE IMPACT OF NANOPARTICLE COATINGS AND NON-UNIFORMITIES ON XPS ANALYSIS: GOLD/SILVER CORE-SHELL NANOPARTICLES

Yung-Chen Wang[a] and David G. Castner*[a,b]

[a]National ESCA & Surface Analysis Center for Biomedical Problems, Department of Bioengineering, Box 351653, University of Washington, Seattle, WA 98195-1653 USA

[b]National ESCA & Surface Analysis Center for Biomedical Problems, Department of Chemical Engineering, Box 351653, University of Washington, Seattle, WA 98195-1653 USA

*Corresponding Author

David Castner

University of Washington

Department of Bioengineering and Chemical Engineering

Box 351653

Seattle, WA 98195

1-206-543-8094 (phone)

1-206-221-7451 (fax)

castner@uw.edu (e-mail)

6.1 ABSTRACT

Spectral modeling of photoelectrons can serve as a valuable tool when combined with X-ray photoelectron spectroscopy (XPS) analysis. Herein, a new version of the NIST Simulation of Electron Spectra for Surface Analysis (SESSA 2.0) software, capable of directly simulating spherical multilayer NPs, was applied to model citrate stabilized Au/Ag-core/shell nanoparticles (NPs). The NPs were characterized using XPS and scanning transmission electron microscopy (STEM) to determine the composition and morphology of the NPs. The Au/Ag-core/shell NPs were observed to be polydispersed in size, non-circular, and contain off-centered Au-cores. Using the average NP dimensions determined from STEM analysis, SESSA spectral modeling indicated that washed Au/Ag-core shell NPs were stabilized with a 0.8 nm layer of sodium citrate and a 0.05 nm (one wash) or 0.025nm (two wash) layer of adventitious hydrocarbon, but didn't fully account for the observed XPS signal from the Au core. This was addressed by a series of simulations and normalizations to account for contributions of NP non-circularity and off-centered Au-cores. Both of these non-uniformities reduce the effective Ag-shell thickness, which effect the Au-core photoelectron intensity. The off-centered cores had the greatest impact for the particles in this study. When the contributions from the geometrical non-uniformities are included in the simulations, the SESSA generated elemental compositions that matched the XPS elemental compositions. This work demonstrates how spectral modeling software such as SESSA, when combined with experimental XPS and STEM measurements, advances the ability to quantitatively assess overlayer thicknesses for multilayer core-shell NPs and deal with complex, nonideal geometrical properties.

6.2 INTRODUCTION

Nanoparticles (NPs) ranging from the sizes of 1 to 100 nm are being used in many branches of science and incorporated into a wide variety of commercial products. Despite the exciting advancement in the applications of NPs, important aspects such as biocompatibility, biostability, and the environmental impact of these NPs must be well characterized for their safe and effective use.[11,107] Attention must also be focused on the concerns of inadequate characterization and under-reporting of data for NP used in biomedical applications.[10,107,158,159] Previous studies aimed at elucidating the relationship between NPs and their physiochemical properties have concluded that synthesis method, size, shape, handling history and surface functionalization of NPs can all play important roles in determining their toxicity and circulation time in biological systems.[13,14,160,161] Common methods used to characterize these properties of NPs include transmission electron microscopy (TEM), dynamic light scattering (DLS), UV/Vis, and Zeta potential measurements.[162] Although these methods provide essential and important information about NPs, they don't provide important detailed and quantitative information about the NP surface composition or indicate possible presence of submonolayer levels of contaminates often present on NP surfaces. It is the outermost surface of nanoparticles, often coated with deliberate or accidental overlayers that directly interact with the surrounding environment. Thus, it is important to obtain a detailed, quantitative characterization of the surface structure and composition of NPs.

Increasingly X-ray photoelectron spectroscopy (XPS) is being used to characterize NPs[10] because it can be used both to detect the presence of monolayer surface coatings and, in combination with computational modeling, thicknesses of single or multiple layers for structured particles.[110,120,163,164] Exponential sensitivity to analysis depths up to ~10 nm makes XPS a useful tool for characterizing NPs that are similar in dimension. XPS is frequently used to identify and verify the presence of functionalized chemical groups and attached-biomolecules on the NP surface through qualitative and quantitative analysis.[11,67,102,165–169] Combining quantitative XPS results and prior knowledge of the overall NP composition, structural properties of the NPs such as particle diameter and overlayer or multiple layer thicknesses can be determined.[170,171]

To date methods of determining shell thicknesses using XPS analysis assume a uniform particle shape and size. Most of these methods also assume a uniform coating thickness and some require extensive calculations.[120,163] Shard developed a more user friendly method for estimating shell thickness of spherical core-shell NPs[123] that was recently extended to spherical core-shell-shell NPs.[25] For particles with additional overlayers or complex morphologies, numerical simulations of various types have been used for calculating layer thicknesses and remain the most useful approach. Earlier generations of the numerial smulations for determining the structure of complex sperical paraticles involved fairly complex simulations not readily ameniable for routine use.[120]

Fortunately there are now several alternative codes that enable an analyst to more routinely model XPS signals from multiple types of nanostructures. These codes provide information such as overlayer or multiple-layer thickness and can be extended to explore effects such as variations size and shape. MultiQuant,[172,173] Quantitative Analysis of Surfaces by Electron Spectroscopy (QUASES),[124,174] and Sumulation of Electron Spectra for Surface Analysis (SESSA) [21,175,176] are among analytical codes that can be used to quantitatively examine the impacts of nanostructure on XPS signals. QUASES can determine the composition and structure of surface nanostructures based on the analysis of peak intensity, peak shape, and the background of inelastic electrons.[124,174] MultiQuant focuses on the impact of particle geometry on relative signal intensities while SESSA is designed for the simulation of the entire photo- and Auger-electron spectrum from a user defined sample.[21,175,176] The previous version of SESSA (Ver. 1.3) was limited to the spectral simulation of layered flat substrates and cannot be directly applied to spherical samples. However, it was successfully applied to characterize the overlayer thickness and structure of 16-mercaptohexadecanoic acid self-assembled monolayer (C16 COOH-SAM) on gold NPs by using a summation of geometrical components with flat surfaces to represent round particles.[110] The most recent version of SESSA (Ver. 2.0) is capable of generating XPS spectra for flat and nanostructures such as islands, spheres, and layered spheres without the need for a user to make a series of complex geometrical corrections.[126] With the ability to simulate multi-layer NPs directly, SESSA can now be easily combined with experimental XPS analysis to provide direct insight into overlayer thickness and structures of NPs.[21]

Although particle uniformity is a target for many synthesis processes and assumed in modeling work, such uniformity is rarely fully achieved. In this work, we used SESSA 2.0 to examine the impact of variations in size, distorations of shape, and effective coating thickness on XPS signals from Au/Ag-core/shell NPs. The particles had been stabilized by sodium citrate and were also covered, as should be expected, by a thin layer of adventitious hydrocarbon. Scanning transmission electron microscopy (STEM) analysis of a series of particles showed that the core/shell Au/Ag NPs, described previously,[160] had a polydispersed size distribution, often had slightly non-circular shapes, and had Au cores that were frequently off-center. The STEM measurements were used to determine average dimensions of the Au core and Ag shell as well as the distribution of deviations from that average. We then combined SESSA's new capability of directly modeling spherical NPs with the experimental XPS results to determine the thickness of the overlayers and, with additional calculations, investigated on how the variations in particle structure impacted the quantitative XPS analysis.

6.3 MATERIALS AND METHODS

6.3.1 MATERIALS

The citrate-stabilized Au/Ag-core/shell nanoparrticles ~20 nm in diameter used in this study are associated with a National Institute of Environmental Health Sciences (NIEHS) Centers for Nanotechnology Health Implications Research (NCNHIR) consortium examining the toxicology of nanoparticles. The ~20 nm particles had been grown on 7 to 8 nm Au seed particles that were purchased from NanoComposix (San Diego, CA) for consortium use. The as received particles, 1 mg/ml particles suspended in a ~2 mM citrate buffer solution and packaged in 30 ml plastic containers, were stored in a refrigerator at 4˚C before any further processing. As measured by dynamic light scattering, the size of the particles used in this study had remained stable during storage since their arrival at PNNL in November 2011 (longer than the recommended particle shelf lifetime). Papers describing and using these particles in toxicological studies have been published.[10,175–177]

6.3.2 SCANNING TRASMISSION ELECTRON MICROSCOPY (STEM)

Structural features of the nanoparticles have been analyzed using STEM and high resolution TEM (HR-TEM) imaging and described in an earlier publication.[7] For STEM imaging in this study a FEI-Titan 80-300 microscope equipped with a probe-forming lens corrector was used and operated at an accelerating voltage of 300 keV. The high-angle annular dark-field (HAADF) image collection angle was 50-200 mrad. STEM samples were prepared by drop casting a drop of suspension onto a 200 mesh lacey carbon TEM grid. STEM data in this paper, as described below, was collected during the course of a previously reported study[160] that used the same batch of these NPs.

ImageJ software was used to analyze the diameter, circularity, Au-core diameter, Ag-shell thickness, and the degree of the off-centered Au-core of the Au/Ag-core shell NPs. The NP diameters and circularity were determined using the software's particle analysis algorithm. The boundary of the core and shell were determined visually and applied to calculate the Au-core diameter and Ag-shell thickness by measuring the distance of eight radially spaced straight lines originating from the center of the Au-core to the outer edge of the Ag-shell. The degree of the off centered Au-core was determined by calculating the distance between each particle's maxima (center of the Au-core) and ultimate point (center of the whole particle).

6.3.3 X-RAY PHOTOELECTRON SPECTROSCOPY (XPS)

XPS measurements were performed with a Physical Electronics Quantera Scanning X-ray Microprobe. This system uses a focused monochromatic Al Kα X-ray (1486.7 eV) source for excitation and a spherical section analyzer. The instrument has a 32 element multichannel detection system. A 40 W X-ray beam focused to 200 μm diameter was used for this analysis. The binding energy (BE) scale is calibrated using the Cu2p3/2 peak at 932.62 ± 0.05 eV and Au 4f7/2 peak at 83.96 ± 0.05 eV for known reference foils. The X-ray beam is incident normal to the sample and the photoelectron detector is at 45° off-normal. High-energy resolution spectra were collected using a

pass-energy of 69.0 eV with a step size of 0.125 eV. For the Ag 3d5/2 line, these conditions produced a FWHM of 0.93 eV.

Particles were prepared for XPS analysis by a centrifuge washing process. Stock solution (0.2 mL) was first dispersed in 1.5 ml centrifuge tubes, and then ultra-centrifuged at 30,000 rpm (49,000 ×g maximum, 38,000 ×g average, and 27,000 ×g minimum) for 90 minutes. After the first centrifugation, the supernatant was pipetted off and the particles re-dispersed in 0.2 mL of deionized (DI) water. This re-dispersion was followed by another round of centrifugation and removal of the supernatant. The particles were again re-dispersed and another round of centrifugation followed. After each round of centrifugation a sample of the NPs was saved for XPS analysis. In each case the supernatant was poured off and 20 µL of DI water was added to the NP “plug” to assist deposition onto a cleaned Si wafer for XPS analysis. Multiple drops of solution were applied to create a deposit covering the substrate. The material deposited after one centrifugation cycle is labeled ‘one wash’, the sample after two centrifugation cycles is labeled ‘two wash’. Examining particles after one- and two-wash cycles provides some information regarding stability of the citrate coating with regard to the washing process. Both XPS survey and high-energy resolution spectra were acquired from the deposited NPs. High-resolution spectra were collected from the Ag3d, Au4f, C1s, O1s and Na1s regions. The XPS compositional results were calculated using the standard sensitivity factors provided by PHI MultiPak software version 9.5.1.0 using peak area intensities after a Shirley background subtraction.

6.3.4 SIMULATION OF ELECTRON SPECTRA FOR SURFACE ANALYSIS (SESSA) SIMULATION OF AU/AG-CORE SHELL NPS

SESSA (Version 2.0) can generate XPS data based on a user-defined layered spherical model.[126] The instrumentation parameters used in SESSA including the x-ray source, analyzer, and aperture geometry were set to match the parameters of the PHI Quantera. The properties of the layers such as composition, thickness, and density can be varied to match the experimental XPS results. The density of the layers were estimated by SESSA and assumed to be constant. To determine the elemental composition of the simulated spectra, the peak areas generated by SESSA were

divided by their corresponding sensitivity factor and normalized as percent elemental composition. In this work, simulations were done for a single NP as previous studies have shown a single NP provides a good representation of a disordered, powder-like film of NPs.[120,126] Lastly, all simulations included elastic scattering of the photoelectrons.

6.4 RESULTS AND DISCUSSIONS

6.4.1 NANOPARTICLE CHARACTERIZATION

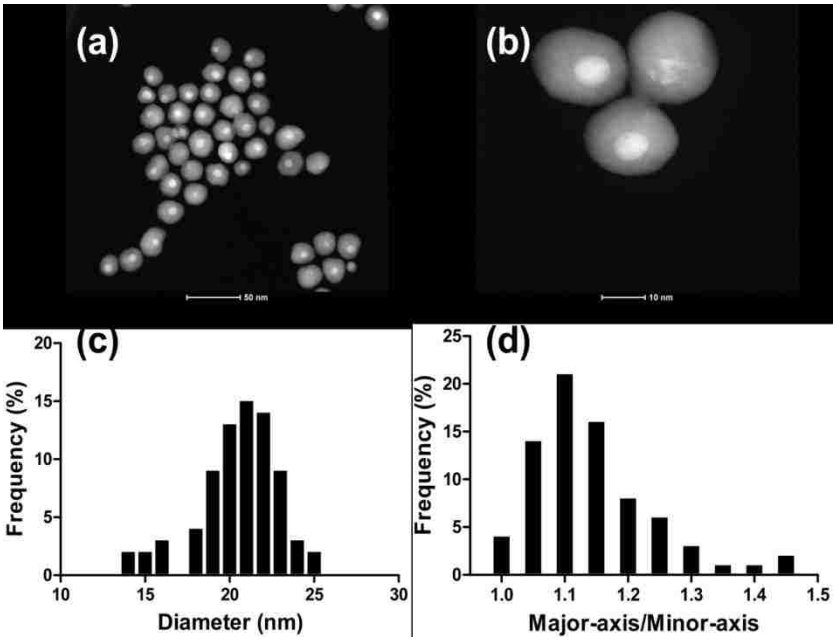

Figure 6.1. (a & b) STEM images of Au/Ag-core/shell nanoparticles. (c) Distribution of Au/Ag-core/shell nanoparticle diameter with a bin width of 1 nm and a mean diameter of 20.5 ± 2.4 nm (n = 76 particles). (d) Distribution of Au-core Ag shell nanoparticle major-axis/minor-axis ratio with a bin width of 0.05 and a mean ratio of 1.14 ± 0.1 (n = 76 particles).

The size and circularity of the Au/Ag-core/shell NPs were determined from Image J analysis of the STEM images (Figure 6.1.(a)&(b)). The NPs had a mean diameter of 20.5 ± 2.4 nm (Figure 6.1.(c)) and an average non-circularity of 1.14 ± 0.1, as measured using the ratio of the major axis and minor axis of individual NPs (Figure 6.1.(d)). The size and circularity calculations were based on analysis of 76 particles. The NPs had a wide size distribution ranging from 13.8 nm to 24.8 nm and most deviated noticeably from a perfect sphere (*e.g.*, more than 60% of the particles had a major-axis / minor axis ratio larger than 1.1). Off-centered Au-cores, defined as the difference between the

center of the whole particle and the center of the Au core, were also observed for most NPs.

Figure 6.2 shows the cross sectional schematic of the ‘ideal’ or ‘average’ Au/Ag-core shell NPs assuming they were spherial particles with the average particle size and core diameter measured from the STEM images. As purchased from the manufacturer, the Au/Ag-core shell NPs were stabilzed with sodium citrate. The outermost adventitious hydrocarbon overlayer likely orginiates from the various steps in sample handling including air exposure during preparation prior to XPS analysis.

The mean diameter of the Au-core and the mean Ag-shell thickness measured manually from the STEM images were 7.4 ± 0.9 nm and 6.4 ± 2.3 nm. The whole particle diameter calculated using these manual measured results (20.2 nm) matches well with the particle diameter (20.5 ± 2.4 nm) determined from ImageJ’s particle analysis algorithm. Further, no correlation was observed between the polydispersity, circularity, and Au-core off centered effect in the Au-core/Ag-shell NPs (see the supplementary Figure S6.1-S6.3).

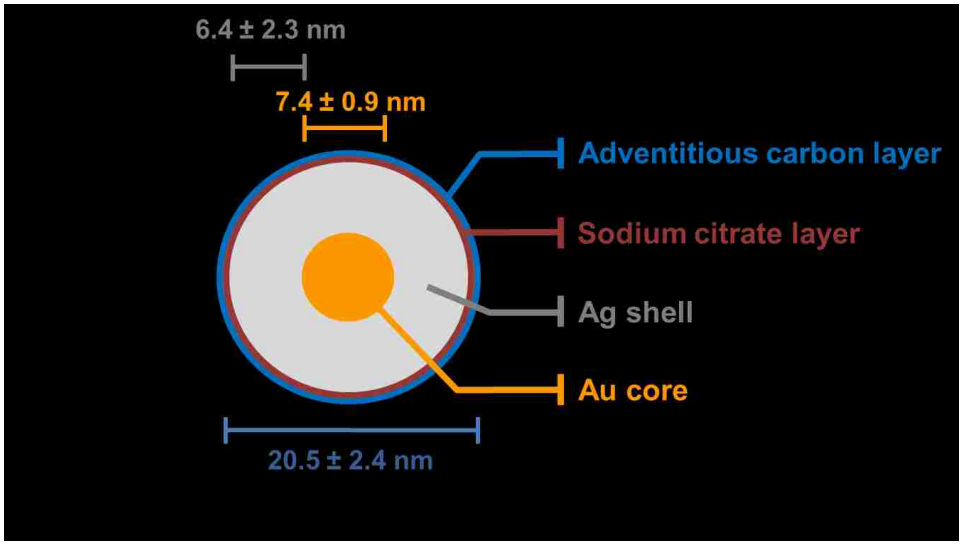

Figure 6.2. Cross sectional schematic of an average, ideal Au/Ag core/shell nanoparticle. The mean for the measured Au-core diameter and Ag-shell thickness was 7.4 ± 0.9 nm and 6.4 ± 2.3 nm (52 particles), respectively. Whole particle diameter derived from the manually measured mean core diameter and shell thickness (20.2 nm) matches closely to the whole particle diameter measured using ImageJ’s particle analysis algorithm (20.5 ± 2.4 nm). Figure not to scale.

6.4.2 XPS ANALYSIS

For comparison to SESSA we focus primarily on examination of the XPS determined atomic compositions and comparing the experimental determined values to those simulated from various models. The XPS determined atomic compositions for the one-wash and two-samples are shown in Table 1. These compositions are determined in the standard way using peak areas and sensitivity factors and assuming a flat surface and uniform elemental distribution. This information is effectively “reinterpreted” using SESSA or other modeling methods to obtain layer and coating information. For comparison the XPS results for a samples of NPs that had been deposited without washing (no-wash sample) is also included. Several different replicates of the no-wash samples were prepared directly from the citrate buffer solution, but typically various contaminants were detected by XPS. Only one of the no-wash samples had just the expected elements of Ag, Au, C, O and Na. That analysis is shown in Table 1. XPS analysis of three-wash samples was also done, but aggregation of the NPs made it difficult to deposit a uniform layer of NPs onto the silicon substrate, resulting in the presence of significant XPS substrate signals (e.g., Si) from all three-wash samples. Thus, because significant substrate signals were detected from all three-wash samples analyzed, no XPS results from the three-wash samples are included in Table 1. The problems encountered analyzing the no wash and three-wash samples provide yet another example of how NP handling and processing can have a significant influence on the characterization results and the necessity of documenting the history and state of the NPs analyzed.

The XPS atomic compositions of the one- and two-wash samples are the same within experimental error, although for the two-wash sample the concentrations of elements from the citrate and hydrocarbon overlayers (C, O and Na) are slightly lower and the concentrations of the elements from the metallic core (Ag and Au) are slightly higher than for the one-wash sample. The XPS atomic composition of the no-wash sample is significantly different from both the one-wash and two-wash samples, with increased signals from thicker citrate and hydrocarbon layers which result in increased attenuation of Ag and Au signals from the metallic core. The stoichiometric atomic ratio of C/O for sodium citrate is 0.86. The observed C/O ratio in the one- and two-wash

samples is slightly higher (1.0), consistent with the presence of small amounts of adventitious hydrocarbon. The C/O ratio is even higher (1.4) on the no-wash sample, indicating the presence of a thicker adventitious hydrocarbon layer on this sample. Further quantification of the XPS results will be provided below.

Table 6.1. XPS determined atomic composition of Au/Ag core-shell nanoparticles deposited onto silicon wafer substrates. Average values and standard deviations are reported for six replicate analyses of the one- and two-wash samples. Only one analysis is reported for the no-wash sample (see text for details).

	XPS Atomic Percent				
Sample	Silver	Gold	Carbon	Oxygen	Sodium
no wash (n = 1)	26.1	0.41	40.3	29.0	4.2
one wash (n = 6)	50.9 $\pm$ 4.1	0.75 $\pm$ 0.04	22.1 $\pm$ 1.8	22.0 $\pm$ 1.5	4.3 $\pm$ 1.1
two wash (n = 6)	53.9 $\pm$ 1.3	0.69 $\pm$ 0.03	21.0 $\pm$ 1.2	21.0 $\pm$ 0.6	3.4 $\pm$ 0.3

6.4.3 SESSA SIMULATIONS

SESSA simulations of the Au/Ag-core/shell NPs were initially based on the schematic NP presented in figure 6.2. The Au-core diameter and Ag-shell thickness of the NP model were measured from STEM images. To obtain accuarate thickness of the sodium citrate and adventitious carbon layer, SESSA simulations were performed for the one- and two-wash samples using various thickness of both layers to find the best match to the experimental XPS elemental composision. For the one- and two- wash samples, respectively, it was determined that a 0.05 nm and 0.025 nm thick adventitious hydrocarbon layers provided the best match between the SESSA determined and experimentally determined elemental composition of the NPs (table S6.1). As expected from the XPS composition in Table 1, the no-wash sample had a noticely thicker (~0.2 nm) adventitious hydrocarbon overlayer.

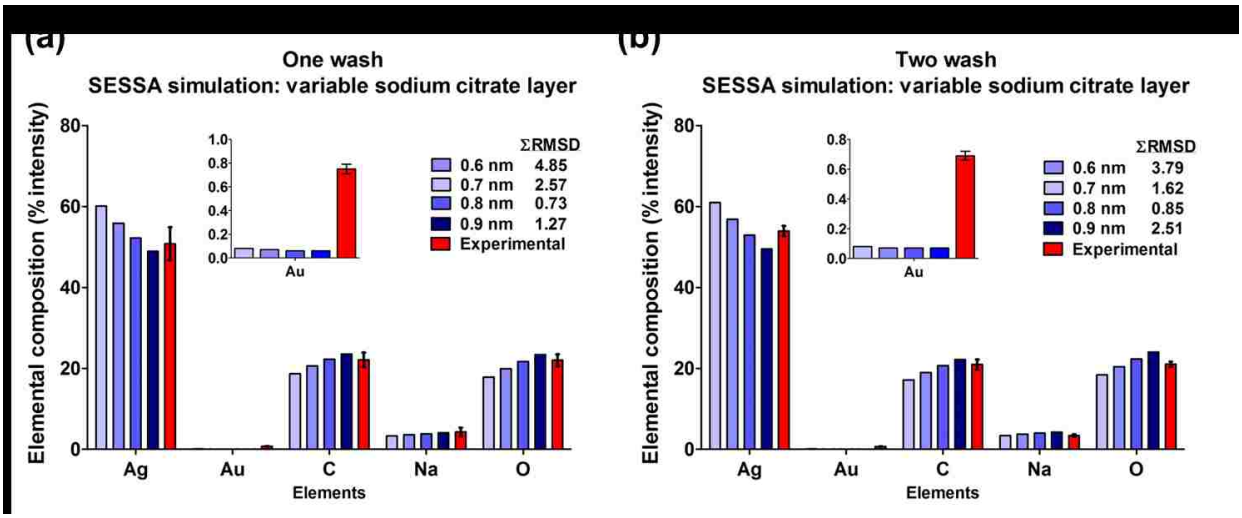

Figure 6.3. Comparison of experimental XPS result and SESSA simulation of the composition for Au/Ag-core/shell nanoparticles with varying sodium citrate thickness ranging from 0.6 nm to 1.0 nm for the one-wash (a) and two-wash (b) samples. The sum root mean square deviation (ΣRMSD) indicates the simulated elemental composition (%) for all elements compared to the experimental XPS result.

NP core/shell with an increase of the carbon, sodium, and oxygen intensities from sodium citrate overlayer. To quantitatively determine the appropriate sodium citrate thickness for the one-wash and two-wash sample, the sum of the root mean squred deviation (ΣRMSD) of the simulated results for each elemenet was compared with the experimental XPS result. Smaller ΣRMSD value implies a better match between the experimental and simulated elemental composition. Simulation using a 0.8 nm thick sodium citrate layer provided the lowest ΣRMSD and therefore the best fit with the experimental XPS results for the NPs after one wash and two wash. Table S1 shows the combined effect of varying sodium citrate and adventitious hydrocarbon layer thickness on the ΣRMSD vaule. Thus, the second centrifuge washing resulted in at most a slight reduction of the adventitious hydrocarbon layer thickness. In comparison the citrate layer was ~2x thicker (~1.8 nm) on the no-wash sample. For all samples, the SESSA simulated gold intensities were on average lower than the experimental gold intensity by a factor of >3.

The underestimation of gold intensity by SESSA simulations using an “average” spherical particle is due to the actual geometrical properties of the Au/Ag-core/shell NPs shown in Figure 6.1 (range of sizes, non-sphereical shape and offset Au cores). The wide distribution in particle sizes can potentially impact the simluation result as the ratio

of surface to bulk atoms will change with particle size. However, the majority of the polydispersity for the Au-core/Ag-shell NP particle sizes was due to variations in the Ag-shell thickness due to both particle non-circularity and deviation of the core from the particle center. As shown in figure 6.2, STEM image analysis showed the mean Au-core diameter has a smaller variation (± 0.9 nm) than the variation in the Ag-shell thickness (± 2.3 nm). The polydispersity of the NPs can be described geometrically by deviations in NP circularity and the off-centered position of the Au-core, as both of these quantities affect the NP's Ag-shell thickness (distance from the Au-core surface to the particle surface) distribution. Simulations of different NP structures were used to determine the sensitivity of XPS signals to the different types of variations observed in the real nanoparticles.

Since NPs can only be simulated as perfect spheres with fixed diameter in the current version of SESSA, the contribution from non-spherical NPs can't be accounted for directly with SESSA. However, non-spherical Au/Ag-core/shell NPs can be thought of as consisting of a range of Ag-shell layer thicknesses, which in turn result in different degrees of Au photoelectron attenuation. Experimentally, Au photoelectrons passing through different thicknesses of Ag-shells do not average out since Au photoelectron intensity depends exponentially on the distance traveled. The non-spherical properties of the Au/Ag-core shell NPs can therefore contribute to the underestimation of gold intensity by SESSA simulations.

As noted above, the Au-core were not always in the center of the NP (figure 6.4(a)). The degree of the off-centered Au-core was characterized quantitively by measuring the distance between the center of the Au-core and the center of the whole Au/Ag-core shell NP (figure 6.4). Off-centered Au cores were observed in most NPs, with an mean off centered distance of 2.2 ± 1.3 nm (Figure 6.4(b)). Similar to non-spherical NPs, off-centered Au-cores will lead to range of Ag-shell thicknesses and the underestimation of gold intensity by SESSA simulations.

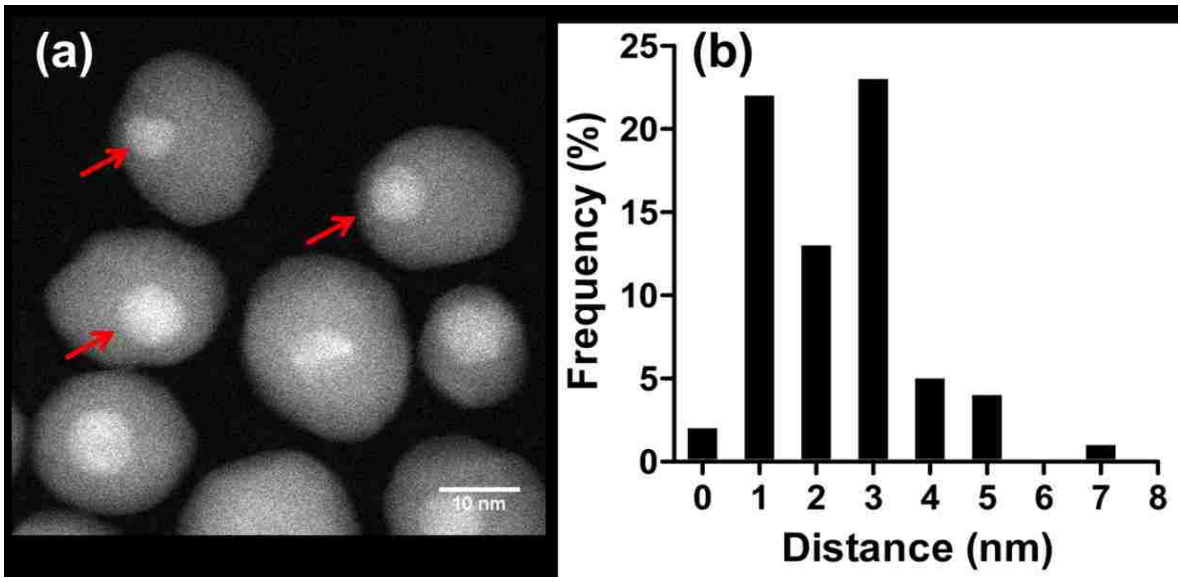

Figure 6.4. (a) STEM images of Au/Ag-core/shell nanoparticles containing non-centered cores as highlighted by red arrows. (b) Distribution of the distance of gold core off-center relative to the whole Au/Ag-core/shell nanoparticle with bin width of 1 nm and mean distance of 2.2 ± 1.3 nm (n = 70 particles).

To quantity the impact of the non-spherical NPs and off-centered Au-cores we investigated how altering the dimension of the Au-core diameter and Ag-shell thickness affected the simulated results for the one-wash and two-wash NPs (figure 6.5). These axes of these plots show the “deviation” or DELTA of the effective Ag shell thickness and Au core diameters relative to those of the “average” particle. The optimal sodium citrate and adventitious hydrocarbon layer thicknesses determined from earlier simulations (figure 6.3 and table S6.1) were used for these simulations. The difference of gold elemental atomic % between the experimental XPS results and the SESSA simulations were plotted as a function of the delta Au and Ag dimensions. The darker blue region in the both panels of figure 6.5 corresponds to specific combinations of Au and Ag dimensions that produce the best agreement between the experimental XPS results and the SESSA simulations. The red circle located near the center of figures indicates the average dimension of the Au/Ag core-shell NPs determined from the STEM images. From the previous simulations shown in figure 6.3, it was determined that the average experimental STEM dimensions alone could not adequately model the actual Au/Ag-core/shell NPs as they do not account for the complex geometrical properties of the actual NPs. For both the one-wash and two-wash samples, the results

in figure 6.5 show that to best match the SESSA Au atomic % to the experimental Au atomic % requires the Ag-shell thickness to decrease by 2.5 nm, which is comparable to the standard deviation of the STEM determined Ag shell thickness. Note than increasing the Ag shell thickness above the average STEM dimension results in minimal changes in the Au atomic % since the simulated Au intensity approaches zero under these conditions. Also, just increasing the Au-core diameter while keeping the Ag-shell thickness fixed at the average STEM value would require unrealistic increases in the Au core diameter (>10 nm) for the simulations to match the experimental XPS results. Thus, variation of the Ag shell thickness had a significantly larger effect on simulated Au intensities than changes in the Au-core diameter. This confirms that the Ag-shell thickness of the NPs was effectively thinner than the average value determined from analysis of the STEM images, resulting in stronger experimental XPS Au signals. The no-wash sample also showed the same effects of requiring a thinner Ag shell to match the simulated and experimental Au concentrations.

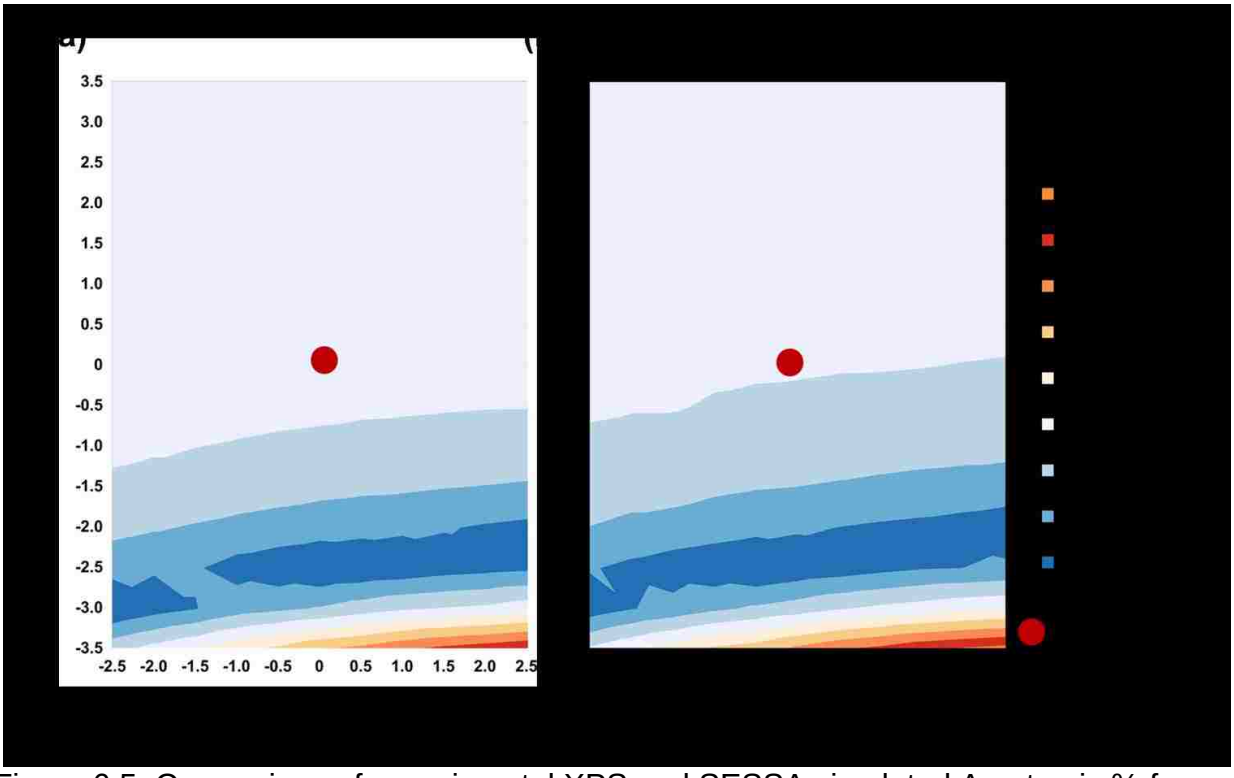

Figure 6.5. Comparison of experimental XPS and SESSA simulated Au atomic % for varying Ag-shell thicknesses and Au-core diameters. The apparent ΔAg-shell thickness and ΔAu-core thickness are relative to the average particle dimensions. (a) One centrifuge wash. (b) Two centrifuge wash. The red dot on both panels indicates the average dimensions of the Au-core and Ag-shell determined by STEM.

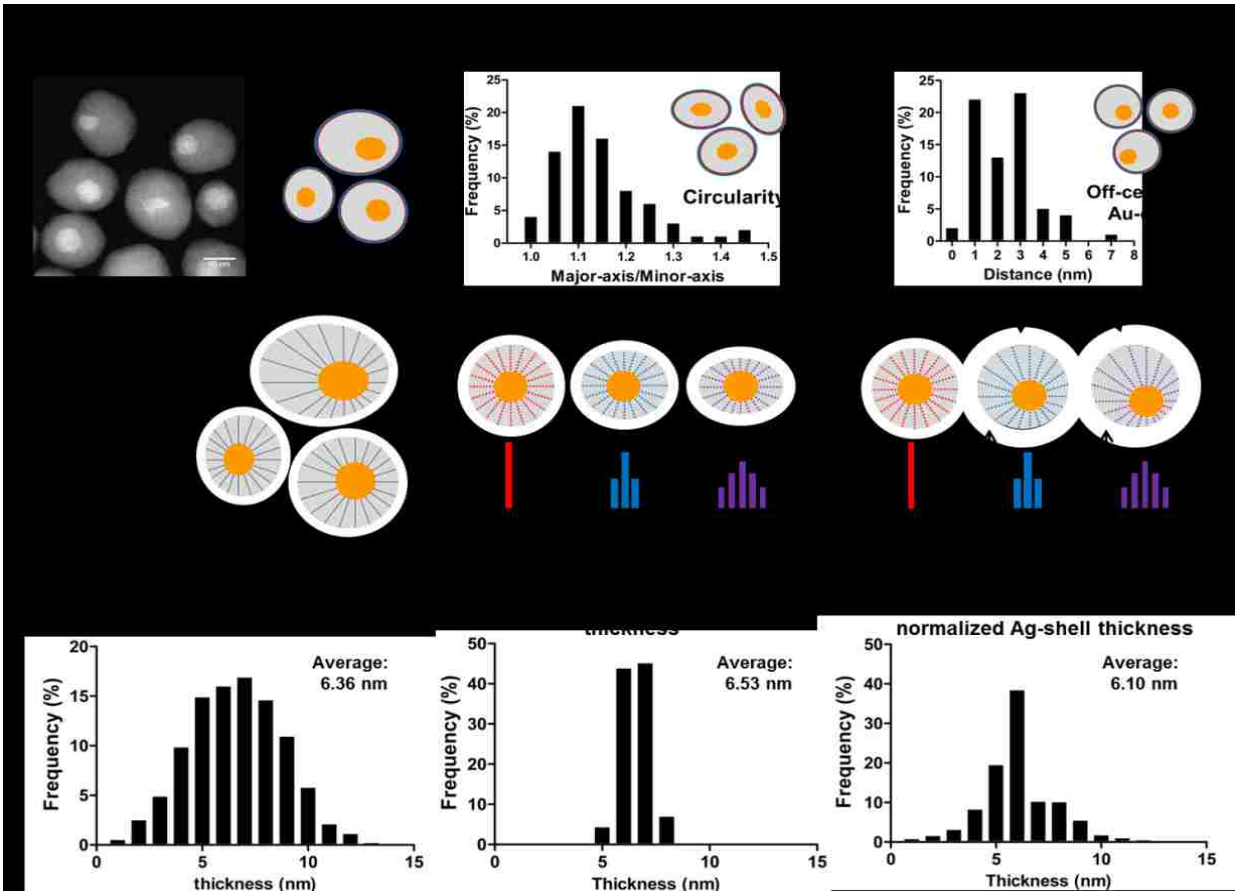

Figure 6.6. Schematic illustration of the Ag-shell thickness normalization using: (a) the experimentally measured Ag-shell thickness distribution from STEM analysis, (b) only the non-circularity of the Au/Ag-core shell NPs and assuming the Au-core is located in the center of the particle, and (c) only the degree of off-centered for the Au-core while assuming the particle is perfectly circular.

Although SESSA cannot directly simulate NP samples with a distribution of dimensions, it is possible to simulate various Ag-shell thickness seperately and normalize the result based on the corresponding Ag-shell distribution. figure 6.7 compares the simulation results for the one- and two-wash samples based on experimentally measured and various normalized Ag-shell distributions shown in figure 6.6. As expected, for all models the SESSA simulations showed good fit to the experimental data for all elements except gold. For the one wash sample (figure 6.7(a)), comparing to the experimental gold composition (0.75 atomic %), the simulation based on the average STEM dimensions significantly underestimated the gold composition (0.07 atomic %). The simulation based on the experimentally measured circularity slightly increased gold composition to 0.09 atomic %, while accounting for the off-

centered Au-cores showed a much greater increase in gold composition to 0.36 atomic %. Lastly, simulation based on STEM measured Ag-shell distribution, which includes both non-circularity and off-centered core effects, generated the best match of the simulated gold composition (0.64 atomic %) to the experimental XPS gold composition (0.75 atomic %). Similar effects were also observed for the two wash sample (Figure 6.7.(b)) and no-wash sample (data not shown). Thus, accounting for the polydispersity of the both non-circularity and off-centered core for the Au/Ag-core/shell NPs is necessary to obtain good agreement between the SESSA and experimental XPS results, with the off-centered Au-core having a larger effect than the NP non-circularity.

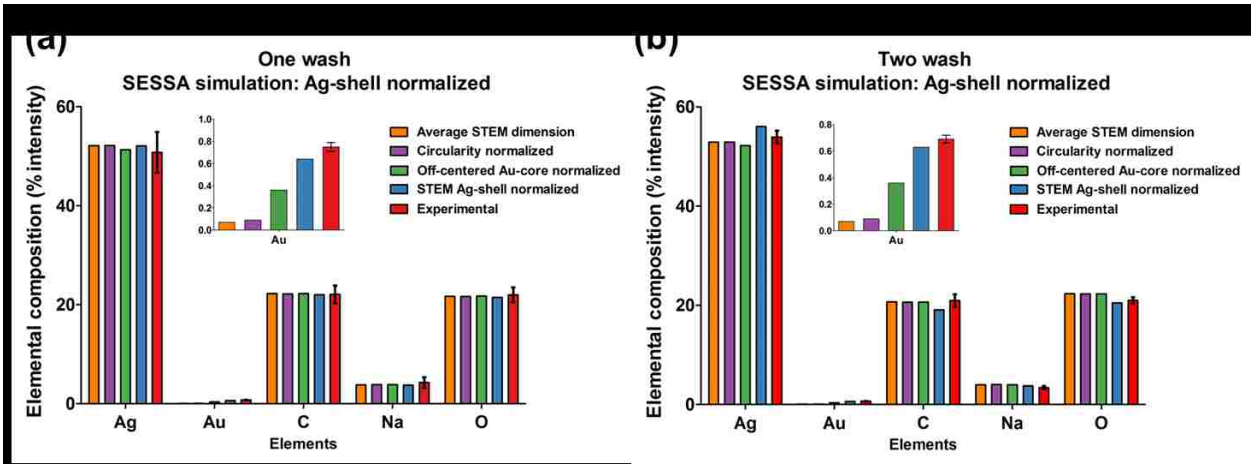

Figure 6.7. Comparison of experimental XPS results and SESSA simulations for the (a) one-wash and (b) two-wash Au/Ag-core/shell NPs based on the average STEM dimension, circularity normalized, off-centered Au-core normalized, and the STEM Ag-shell normalized Ag-shell distribution. By including the impacts of both non-circularity and off center cores based on the STEM distributions, the model matches the experimental data and the off-centered cores were found to have the greatest impact.

6.5 CONCLUSION

The new version of spectral modeling software SESSA (Ver. 2.0) was applied to simulate Au/Ag-core/shell NPs that are polydispersed, non-circular, and contained off-centered Au-cores. The SESSA approach is relatively easy to apply and can provide important information about coatings, coating stability, and the effectiveness of cleaning and other sample handling processes. The simulation of an “average” ideal spherical particles provided consistent determination of the adventitious hydrocarbon contamination and citrate layer thicknesses, but variations in particle geometery needed

to be considered to explain and properly quantify the deviation in the Au signals from the NP core.

Simulation results based on average NP dimensions determined that the Au/Ag-core shell NPs after one and two wash cycles were stabilized with a 0.8 nm thick layer of sodium citrate and coated by a 0.05 nm (one wash) and 0.025 nm (two wash) thick adventitious hydrocarbon overlayers. There was little difference between the samples identified as one and two wash. However, significant differences were observed for the zero and three wash samples, providing information about the durability of the citrate layer to this washing method and the effectiveness of the wash.

Simulating NPs with average dimensions and not accounting for the geometrical properties of the NPs resulted in significant underestimation of the gold intensity. To address this, a series of simulations based on detailed STEM image analysis were performed to include the contribution of the non-ideal geometrical properties. We were able to separate the contribution of NP non-circularity NPs and off-centered Au-cores and determine their individual impact on the simulated elemental composition of the Au/Ag-core shell NPs. Simulations based on the combined effect of NP circularity and off-centered Au-core resulted in reduced effective Ag-shell thickness and provided simulated elemental compositions that matched the experimental XPS results.

This work demonstrates the impact of using SESSA to model NPs with non-ideal geometrical properties and highlights the benefits of combining SESSA with experimental XPS and STEM analysis to obtain a detailed understanding and insight into how to quantify the effects of non-ideal geometries for characterizing the structure and composition of actual NPs.

6.6 ACKNOWLEDGEMENT

Y.-C. Wang and D.G. Castner gratefully acknowledge the support from National Institutes of Health grant EB-002027 to NESAC/BIO from the National Institute of Biomedical Imaging and Bioengineering. D.R. Baer acknowledges support from the National Institutes of Health, National Institute of Environmental Health Sciences (NIEHS) under grant U19 ES019544. The silver nanomaterials were provided by the NIEHS Centers for Nanotechnology Health Implications Research (NCNHIR)

Consortium. Y.-C. Wang was supported by the National Science Foundation Graduate Research Fellowship Program under Grant No. DGE-1256082. Any opinions, findings, and conclusions or recommendations expressed in this material are those of the author(s) and do not necessarily reflect the views of the National Science Foundation. A portion of this research was performed at the Environmental Molecular Sciences Laboratory (EMSL), a national scientific user facility sponsored by the DOE's Office of Biological and Environmental Research and is located at Pacific Northwest National Laboratory (PNNL). We thank Drs. J. Smith and P. Musuamy for assistance with preparation of the samples for the XPS measurements and Dr. C. Wang for the STEM measurements that were reported in[160]. We thank M. Chudzicki, C. Powell, A. Shard, and W. Werner for simulating discussions regarding XPS analysis of nanoparticles.

Chapter 7. CONCLUSIONS AND FUTURE WORK

7.1 CONCLUSIONS

The overall goal of this dissertation was to develop versatile methods for the surface chemical analysis of nanoparticles, both experimentally and computationally. The experimental works encompass characterizing model system alkanethiol self-assembled monolayers (SAMs) on gold surfaces and investigating protein orientation through specific gold nanoparticles (AuNPs) surface modifications. The computational studies include method development of calculating overlayer layer thickness on nanoparticles, modeling the structure of SAMs on gold nanoparticles, and investigating core-shell nanoparticles with complex morphologies.

The work on controlling and probing the orientation of immobilized Protein G B1 on AuNPs was discussed in Chapter 3. A site-specific covalent conjugation chemistry was introduced to control the orientation of the immobilized protein. Utilizing the surface sensitivity of time-of-flight secondary ion mass spectrometry (ToF-SIMS), the orientation of the immobilized determined by the unique secondary ion signal originating from the amino acids at opposite ends of the protein. This study provides a model for investigating protein orientation on nanoparticles and also a platform for further antibody conjugation.

In Chapter 4, it was demonstrated that spectral simulation software Simulation of Electron Spectra for Surface Analysis (SESSA) can directly and accurately model the internal structure of core-shell nanoparticles. SESSA can generate accurate X-ray photoelectron spectroscopy (XPS) spectra and peak intensities when appropriate instrumentation parameters are included. This study serves as a foundation for other SESSA studies in this dissertation by first demonstrating the capability modelling core-shell nanoparticles.

SESSA's modelling capability can be utilized to investigate the structure of SAMs on nanoparticles when combined with experimental XPS analysis. In chapter 5, SESSA was utilized to model a series of SAMs functionalized flat gold and gold nanoparticles. It was shown that SESSA models can accurately describe the SAMs on flat surfaces but

will require additional experimental analysis to model the structurally complex SAMs on nanoparticles.

SESSA can further be applied to characterize non-uniform core-shell nanoparticles with complex morphologies. The work discussed in Chapter 6 demonstrates the impact of using SESSA to model nanoparticles with nonideal geometrical properties and highlights the benefits of a complementary, multitechnique approach with SESSA, XPS, and scanning transmission electron microscopy (STEM) to obtain a detailed understanding into how to quantify the effects of nonideal geometries for characterizing the structure and composition of actual nanoparticles.

Overall, these findings in this dissertation advance the field's understanding on nanoparticle characterization and provides method for quantitative analysis of nanoparticles.

7.2 FUTURE DIRECTION

CONTROLLING ORIENTATION OF IMMOBILIZED ANTIBODY ON GOLD NANOPARTICLES

It was demonstrated in Chapter 3 that the orientation of immobilized protein on AuNPs can be controlled using different Protein G B1 cysteine mutants, which serves as a platform for immunoglobulin G (IgG) antibody immobilization. For future experiments, it will be possible to control the orientation of IgG on AuNPs by using the cysteine mutant that exposes the Fc binding site of Protein G B1. Additional XPS and ToF-SIMS analysis can be used to characterize this process by monitoring changes in atomic nitrogen % and secondary ions from the IgG. Functional assays using fluorescent antigens or localized surface plasmon resonance (LSPR) can be conducted to show that IgG remains active after binding to Protein G B1 on AuNPs. These experiments will provide systematic characterization of the nanoparticle surface modifications and oriented IgG antibody immobilization.

APPLYING SESSA TO MODEL COMPLEX OVERLAYERS

The capability of SEESA to model a wide variety of nanoparticles was demonstrated in this dissertation. However, as discussed in Chapter 5, modelling structures of SAMs on nanoparticles remains a challenge. Additional experimental

analysis that can elucidate the packing and structural information of SAMs on AuNPs can improve SESSA's predictive capability. Further, using the multitechnique approach and complementary experimental analysis, it will be possible to use SESSA to model complex overlayers such as the IgG immobilization on surface modified AuNPs discussed earlier.

Lastly, the upcoming SESSA Version 2.1 will have the capability of simulating customizable nanomorphologies. This implies that future SESSA simulations can simulate nanoparticles that are not spherical nor monodispersed. This feature can expand the applications of SESSA by allowing it to model real life, nonideal nanostructures with ease.

APPENDIX

APPENDIX A. USE OF XPS TO QUANTIFY THICKNESS OF COATINGS ON NANOPARTICLES

Donald R. Baer,[a*] Yung-Chen Wang,[b] David G. Castner[b,c]

[a]Environmental Molecular Sciences Laboratory, Pacific Northwest National Laboratory, Richland WA 99352 USA

[b]National ESCA & Surface Analysis Center for Biomedical Problems, Department of Bioengineering, Box 351653, University of Washington, Seattle, WA 98195-1653 USA

[c]National ESCA & Surface Analysis Center for Biomedical Problems, Department of Chemical Engineering, Box 351653, University of Washington, Seattle, WA 98195-1653 USA

Microscopy Today, 2016, Volume 24, Issue 2, Pages 40-45,
doi:10.1017/S1551929516000109

[*]Electronic mail: don.baer@pnnl.gov

Appendix A.1 ABSTRACT

XPS and other surface sensitive methods are being increasingly used to extract quantitative information about organic and inorganic coatings and contamination on nanoparticles. The extraction of coating thickness requires information about particle diameter from other measurements, such as electron microscopy, combined with a model that includes the physical processes associated with XPS. Advantages of using XPS include the sensitivity to very thin coatings (or surface contamination) and the ability to extract important information about organic layers. Single particle information from electron microscopy combined with XPS sensitivity in determining composition make a powerful combination for nanoparticle analysis.

APPENDIX B. VERSAILLES PROJECT ON ADVANCED MATERIALS AND STANDARDS INTERLABORATORY STUDY ON MEASURING THE THICKNESS AND CHEMISTRY OF NANOPARTICLE COATINGS USING XPS AND LEIS

Natalie A. Belsey,[a] David J. H. Cant,[a] Caterina Minelli,[a] Joyce R. Araujo,[b] Bernd Bock,[c] Philipp Brüner,[d] David G. Castner,[e] Giacomo Ceccone,[f] Jonathan D. P. Counsell,[g] Paul M. Dietrich,[h] Mark H. Engelhard,[i] Sarah Fearn,[j] Carlos E. Galhardo,[b] Henryk Kalbe,[h] Jeong Won Kim,[k] Luis Lartundo-Rojas,[l] Henry S. Luftman,[m] Tim S. Nunney,[n] Johannes Pseiner,[o] Emily F. Smith,[p] Valentina Spampinato,[f] Jacobus M. Sturm,[q] Andrew G. Thomas,[r] Jon P.W. Treacy,[n] Lothar Veith,[c] Michael Wagstaffe,[r] Hai Wang,[s] Meiling Wang,[s] Yung-Chen Wang,[e] Wolfgang Werner,[o] Li Yang,[t] and Alexander G. Shard,*[a]

[a]National Physical Laboratory, Teddington, Middlesex TW11 0LW, U.K.

[b]Instituto Nacional de Metrologia, Qualidade e Tecnologia (INMETRO), Divisão de Metrologia de Materiais (Dimat) Avenida Nossa Senhora das Graças, 50 Duque de Caxias, RJ 25250-020, Brazil

[c]Tascon GmbH, Mendelstr. 17, D-48149 Münster, Germany

[d]ION-TOF GmbH, Heisenbergstr. 15, 48149 Münster, Germany

[e]National ESCA and Surface Analysis Center for Biomedical Problems, Departments of Bioengineering and Chemical Engineering, University of Washington, Seattle, Washington 98195-1653, United States

[f]European Commission, Directorate General Joint Research Centre, Directorate F – Health, Consumers and Reference Materials, Consumer Products Safety Unit, Via E. Fermi 2749 TP125 I21027 Ispra (VA), Italy

[g]Kratos Analytical Ltd., Wharfside, Trafford Wharf Road, Manchester M17 1GP, U.K.

[h]BAM Federal Institute for Materials Research and Testing (BAM 6.1), Unter den Eichen 44-46, D-12203 Berlin, Germany

[i]Pacific Northwest National Laboratory, EMSL, Richland, Washington 99352, United States

[j]Department of Materials, Imperial College London, South Kensington Campus, London SW7 2AZ, U.K.

[k]Korea Research Institute of Standards and Science, 267 Gajeong-ro, Daejeon 34113, Korea

[l]Instituto Politécnico Nacional, Centro de Nanociencias y Micro y Nanotecnologías, UPALM, Zacatenco, México D.F. CP. 07738, México

[m]Surface Analysis Facility, Lehigh University, 7 Asa Drive, Bethlehem, Pennsylvania 18015, United States

[n]Thermo Fisher Scientific, Unit 24, The Birches Industrial Estate, Imberhorne Lane, East Grinstead, West Sussex, RH19 1UB, U.K.

[o]Institut fuer Angewandte Physik, TU Vienna, Wiedner Hauptstr 8-10, A 1040 Vienna, Austria

[p]Nanoscale and Microscale Research Centre, School of Chemistry, University of Nottingham, University Park, Nottingham NG7 2RD, U.K.

[q]Industrial Focus Group XUV Optics, MESA+ Institute for Nanotechnology, University of Twente, P.O. Box 217, 7500 AE Enschede, The Netherlands

[r]School of Materials and Photon Science Institute, University of Manchester, Manchester M13 9PL, U.K.

[s]National Institute of Metrology, Beijing 100029, P. R. China

[t]Department of Chemistry, Xi'an-Jiaotong Liverpool University, Suzhou, China

The Journal of Physical Chemistry C, 2016, Volume 120, Issue 42, Pages 24070-24079, doi:10.1021/acs.jpcc.6b06713

[*]Electronic mail: alex.shard@npl.co.uk

Appendix B.1 ABSTRACT

We report the results of a Versailles Project on Advanced Materials and Standards (VAMAS) interlaboratory study on the measurement of the shell thickness and chemistry of nanoparticle coatings. Peptide-coated gold particles were supplied to laboratories in two forms: a colloidal suspension in pure water and particles dried onto a silicon wafer. Participants prepared and analyzed these samples using either X-ray photoelectron spectroscopy (XPS) or low energy ion scattering (LEIS). Careful data analysis revealed some significant sources of discrepancy, particularly for XPS. Degradation during transportation, storage, or sample preparation resulted in a variability in thickness of 53%. The calculation method chosen by XPS participants contributed a variability of 67%. However, variability of 12% was achieved for the samples deposited using a single method and by choosing photoelectron peaks that were not adversely affected by instrumental transmission effects. The study identified a need for more consistency in instrumental transmission functions and relative sensitivity factors since this contributed a variability of 33%. The results from the LEIS participants were more consistent, with variability of less than 10% in thickness, and this is mostly due to a common method of data analysis. The calculation was performed using a model developed for uniform, flat films, and some participants employed a correction factor to account for the sample geometry, which appears warranted based upon a simulation of LEIS data from one of the participants and comparison to the XPS results.

APPENDIX C. A TECHNIQUE FOR CALCULATION OF SHELL THICKNESSES FOR CORE-SHELL-SHELL NANOPARTICLES FROM XPS DATA

David J. H. Cant,[a] Yung-Chen Wang,[b] David G. Castner,[b,c] and Alexander G. Shard[a*]

[a]National Physical Laboratory, Hampton Road, Teddington, Middlesex TW11 0LW, UK

[b]National ESCA & Surface Analysis Center for Biomedical Problems, Department of Bioengineering, Box 351653, University of Washington, Seattle, WA 98195-1653 USA

[c]National ESCA & Surface Analysis Center for Biomedical Problems, Department of Chemical Engineering, Box 351653, University of Washington, Seattle, WA 98195-1653 USA

Surface and Interface Analysis, 2015, Volume 48, Issue 5, Pages 274-282, doi:10.1002/sia.5923

[*]Electronic mail: alex.shard@npl.co.uk

Appendix C.1 ABSTRACT

This paper extends a straightforward technique for the calculation of shell thicknesses in core-shell nanoparticles to the case of core-shell-shell nanoparticles using X-ray Photoelectron Spectroscopy (XPS) data. This method can be applied by XPS analysts and does not require any numerical simulation or advanced knowledge, although iteration is required in the case where both shell thicknesses are unknown. The standard deviation in the calculated thicknesses vs simulated values is typically less than 10%, which is the uncertainty of the electron attenuation lengths used in XPS analysis.

APPENDIX D. PYTHON SCRIPT FOR SESSA SIMULATION AUTOMATION

Appendix D.1 BACKGROUND

There were two bottlenecks for running simulations in SESSA. First is the computational time, which can only be improved by upgrading the computer hardware or outsource the computation to a supercomputer. However, for the simulations outlined in this thesis work, more time is actually spent on preparing the simulation software and analyzing the extracted output. The cause of this problem stems from the design of the SESSA program. A user must input the desired nanoparticle composition, instrumentation parameters, and simulation conditions for each analysis. Though one can readily input the information through the graphical user interface (GUI), this process becomes extremely repetitive and time consuming when hundreds or thousands of simulation parameters need to be varied. On the other hand, the software is capable of receiving user inputs through a command line interface (CLI), in which the aforementioned sample composition and instrumentation parameters can be written into a text document in a command line fashion. However, the user still needs to construct the CLI file individually for each type of sample or simulation conditions. The current method of producing these CLI files remains repetitive and time consuming. Therefore, a method that can generate these CLI files automatically can dramatically increase the efficiency of conducing simulations with SESSA. A separate script that can communicate with the SESSA software and execute the simulations by loading the previously generated CLI files can increase the efficiency and enhance the user's experience with the SESSA packages. Further, the script will also able to extract the simulated results and organize them for rapid analysis. Without this script, the simulation must be executed manually and the result also must be collected manually (e.g., copy

and pasting the simulated photoelectron intensity to an Excel file). The goal was to construct a program for generating CLI files from the user designated parameters and integrate the program to automatically perform simulations while collecting and analyzing the data. This program will alleviate the major bottleneck for the current version of SESSA and will benefit future SESSA users and can dramatically improve the user experience with the program.

Python was used to write the script that can automatically generate CLI files and automating the SESSA simulation process. Python was the programming language for the development of the scripts for two main reasons. First, Python interpreters are readily available across most operating systems, meaning that once the script is written, the same version of the script can be used on Windows, Mac, and Unix systems. Second is the readability of the codes and syntax of Python. This implies that even a user without advanced training in computer programming can understand the code easily and can customize the program for their specific needs.

Appendix D.2 APPROACH

The first script, which generates SESSA CLI files, functions by reading a comma-separated values (CSV) file that contains all necessary parameters that the user wish to define. The CSV file can be generated from an Excel template by simply saving the Excel template file as a CSV file. Figure A.1 shows snapshot of the template Excel file for generating layered nanoparticle CLI files. The user can define various common parameters such as the layer composition, density, thickness, and instrumentation parameters. As it is commonly necessary to iterate through a range of thickness or density to find a value that matches experimental analysis, it is possible to directly set the upper boundary and lower boundary in the Excel template file for generating multiple files.

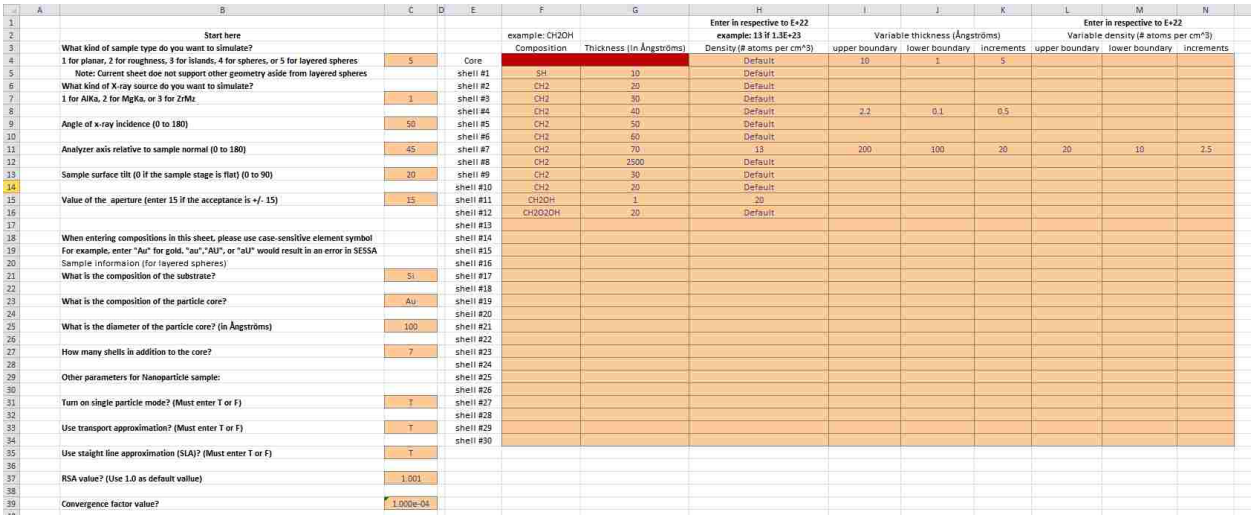

						Enter in respective to E+22						Enter in respective to E+22		
Start here			example: CH2OH		example: 13 if 1.3E+23	Variable thickness (Ångströms)			Variable density (# atoms per cm^3)		
What kind of sample type do you want to simulate?			Composition	Thickness (In Ångströms)	Density (# atoms per cm^3)	upper boundary	lower boundary	increments	upper boundary	lower boundary	increments
1 for planar, 2 for roughness, 3 for islands, 4 for spheres, or 5 for layered spheres	5	Core			Default	10	1	5			
Note: Current sheet doe not support other geometry aside from layered spheres		shell #1	SH	10	Default						
What kind of X-ray source do you want to simulate?		shell #2	CH2	20	Default						
1 for AlKa, 2 for MgKa, or 3 for ZrMz	1	shell #3	CH2	30	Default						
		shell #4	CH2	40	Default	2.2	0.1	0.5			
Angle of x-ray incidence (0 to 180)	50	shell #5	CH2	50	Default						
		shell #6	CH2	60	Default						
Analyzer axis relative to sample normal (0 to 180)	45	shell #7	CH2	70	13	200	100	20	20	10	2.5
		shell #8	CH2	2500	Default						
Sample surface tilt (0 if the sample stage is flat) (0 to 90)	20	shell #9	CH2	30	Default						
		shell #10	CH2	20	Default						
Value of the aperture (enter 15 if the acceptance is +/- 15)	15	shell #11	CH2OH	1	20						
		shell #12	CH2O2OH	20	Default						
		shell #13									
When entering compositions in this sheet, please use case-sensitive element symbol		shell #14									
For example, enter "Au" for gold. "au","AU", or "aU" would result in an error in SESSA		shell #15									
Sample information (for layered spheres)		shell #16									
What is the composition of the substrate?	Si	shell #17									
		shell #18									
What is the composition of the particle core?	Au	shell #19									
		shell #20									
What is the diameter of the particle core? (in Ångströms)	100	shell #21									
		shell #22									
How many shells in addition to the core?	7	shell #23									
		shell #24									
Other parameters for Nanoparticle sample:		shell #25									
		shell #26									
Turn on single particle mode? (Must enter T or F)	T	shell #27									
		shell #28									
Use transport approximation? (Must enter T or F)	T	shell #29									
		shell #30									
Use staight line approximation (SLA)? (Must enter T or F)	T										
RSA value? (Use 1.0 as default vallue)	1.001										
Convergence factor value?	1.000e-04										

Figure D.1. Excel template for generating SESSA session files for layered nanoparticles. It is possible to define various common parameters such as layer composition, thickness, density, and instrumentation parameters. If the user wishes to generate multiple files by varying the thickness and density information of certain layers, user can simply set the upper and lower boundary for those layers.

The script for generating session files will read the CSV files and record the necessary information for generating CLI files. When no variables are defined, the script simply output a single CLI files that contain specific command that SESSA can execute. When thickness or density are varied, the script will iterate through all possible combination of the all variables and output all CLI files that contains the incremental changes for each variable.

The second script can automate the process of loading session files and recording the simulated XPS intensity. This script communicates with SESSA and loads each CLI file automatically. After all the simulations are completed, the script will read all result files generated by SESSA and generate an Excel file that contains formatted XPS intensity along with the name of the peak for easy analysis.

Appendix D.3 SCRIPT FOR GENERATING SESSION FILES

```
# Goal: generate session files automatically for SESSA software V2.0. Python version 3
from datetime import datetime
import os.path
import sys
```

```
import csv
import itertools

# ---------Welcome message---------#
# print('')
# print('Hi! This is a program that generates SESSA V2.0 session files')
# print('This program is especially helpful if you need to generate lots of files!
\n')
# print('This script is optimized for layered sphere sample\n')
# ---------Methods for various things--------#

# reads the value of a certain cell based on the format of cell location (column, row)
def read_cell(x, y):
    with open('SESSA_sample_def.csv', 'r') as f:
        reader = csv.reader(f)
        y_count = 0
        for n in reader:
            if y_count == y:
                cell = n[x]
                return cell
            y_count += 1


def read_layered_spheres_information():
    s_type = int(read_cell(2, 3))  # sample_type
    x_s = int(read_cell(2, 6))  # x_ray source type
    x_r = float(read_cell(2, 8))  # x_ray_incident angle
    a_axis = float(read_cell(2, 10))  # analysis axis angle
    s_surface = float(read_cell(2, 12))  # sample surface normal (angle)
    a_angle = float(read_cell(2, 14))  # aperture angle
    c_substrate = read_cell(2, 20)
    c_composition = read_cell(2, 22)  # core composition
    c_diameter = read_cell(2, 24)  # core diameter
    n_of_shells = int(read_cell(2, 26))  # number of additional shells
    single = read_cell(2, 30)
    trans = read_cell(2, 32)
    sla = read_cell(2, 34)
    rsa = float(read_cell(2, 36))
    convergence_fact = read_cell(2, 38)
    return s_type, x_s, x_r, a_axis, s_surface, a_angle, c_substrate, c_composition,
c_diameter, n_of_shells, \
        single, trans, sla, rsa, convergence_fact

def increment_calc(incre, upper, lower):
    total_dis = float(upper) - float(lower)
    result = total_dis // float(incre)
    if total_dis % float(incre) == 0.0:
        result -= 1
    vary_list = []
    for nn in range(int(result) + 1):
        vary_list.append(float(lower) + (nn * float(incre)))
    vary_list.append(float(upper))
    return vary_list

# ---------Welcome message---------#
print('Before we begin, please define your sample parameters using the template excel
file: SESSA_sample_def')
print('Save the file as a CSV (comma separated value file) in the current directory as
"SESSA_sample_def.csv"\n')
input('Enter any key to continue...\n')

# Check if the proper CSV file exist, else return an error message
if os.path.isfile('SESSA_sample_def.csv') is False:
```

```
    print('CSV file not found in the current directory.')
    sys.exit('Please make sure the CSV file exist in the current directory and restart
the script')

# Read the sample information from the CSV file for layered sphere sample
sample_type, x_source, x_ray_incident, analysis_axis, sample_surface, aperture_angle,
sub_comp, core_composition\
, core_diameter, number_of_shells, single_particle_TF, transport_approx_TF, sla_TF,
rsa_value, convergence_factor\
    = read_layered_spheres_information()

# ---Read values of the additional layers, including possible variation in thickness &
density----#
# Read shell composition based on the user input of the number of shells
shell_comp_list = []
for n in range(4, 4 + number_of_shells):
    shell_comp_list.append(read_cell(5, n))
# Read shell thickness based on the user input of the number of shells
shell_thick_list = []
for n in range(4, 4 + number_of_shells):
    shell_thick_list.append(float(read_cell(6, n))*2)

# For layered spheres, shell thickness need to be doubled
# Read shell density based on the user input of the number of shells
density_list = []
for n in range(3, 4 + number_of_shells):
    density_list.append(read_cell(7, n))

# Read the variable values (if exist) thickness first, followed by density, including
the boundaries and increments
nested_variable_thick = []
vary_thick_TF = False  # Default assuming no variation in thickness
vary_thick_TF_list = [False]
for p in range(number_of_shells):
    vary_thick_TF_list.append(False)

vary_density_TF = False  # Default assuming no variation in density
vary_density_TF_list = [False]
for q in range(number_of_shells):
    vary_density_TF_list.append(False)

#  Read the thickness variation (and check if exist) and save to a nested list
for z in range(number_of_shells+1):
    temp_list = []
    for zz in range(8, 11):
        if read_cell(zz, z+3) != '' and z > 0:
            temp_list.append(float(read_cell(zz, z+3))*2)

# For layered spheres, shell thickness need to be doubled
        elif read_cell(zz, z+3) != '' and z == 0:
            temp_list.append(float(read_cell(zz, z+3)))
        else:
            temp_list.append(read_cell(zz, z+3))
        if read_cell(zz, z+3) != '':
            vary_thick_TF = True
            vary_thick_TF_list[z] = True
    nested_variable_thick.append(temp_list)

# Similar to above, read the density variation information in a nested list
nested_variable_density = []
for i in range(number_of_shells+1):
    temp_list = []
    for ii in range(11, 14):
```

```
        if read_cell(ii, i+3) != '':
            temp_list.append(float(read_cell(ii, i+3)))
            vary_density_TF = True
            vary_density_TF_list[i] = True

# Mark the shell that needs to be varied (density)
        else:
            temp_list.append(read_cell(ii, i+3))  # else case for no entry

    nested_variable_density.append(temp_list)

# Count the number of varying layers ( including the core )
number_layer_variables = 0  # Holds the value of the numbers of total varying layers
for n in range(len(vary_density_TF_list)):  # add up the total number of varying
density layers
    if vary_density_TF_list[n] is True:
        number_layer_variables += 1
for n in range(len(vary_thick_TF_list)):
    if vary_thick_TF_list[n] is True:
        number_layer_variables += 1

# Method for creating nested list that contains the new parameters based on the
potential variations
# First, take the upper and lower boundary and create a list of intermediate values
# Thickness first
nested_variable_thick_list = []
for n in range(len(nested_variable_thick)):
    if vary_thick_TF_list[n] is False:  # No action if that layer isn't varying
        pass
    else:
        upper_bound = nested_variable_thick[n][0]  # upper limit
        lower_bound = nested_variable_thick[n][1]  # lower limit
        increment = nested_variable_thick[n][2]    # increment
        if upper_bound <= lower_bound:  # upper & lower value check
            sys.exit('The upper boundary of a thickness in the CSV file is smaller
than the lower boundary')
        temp_vary_thick_list = increment_calc(increment, upper_bound, lower_bound)
        nested_variable_thick_list.append(temp_vary_thick_list)  # Save as a nested
list that contains all values

# Similar concept for the density variation
nested_variable_density_list = []
for n in range(len(nested_variable_density)):
    if vary_density_TF_list[n] is False:
        pass
    else:
        upper_bound = nested_variable_density[n][0]  # upper limit
        lower_bound = nested_variable_density[n][1]  # lower limit
        increment = nested_variable_density[n][2]    # increment
        if upper_bound <= lower_bound:  # upper & lower value check
            sys.exit('The upper boundary of a density in the CSV file is smaller than
the lower boundary')
        temp_vary_density_list = increment_calc(increment, upper_bound, lower_bound)
        nested_variable_density_list.append(temp_vary_density_list)

# Count the total number of files that will be generated
total_generated_files = 1  # preset minimal of 1 file
for n in range(len(nested_variable_thick_list)):
    temp = len(nested_variable_thick_list[n])  # check the length of each nested list
    total_generated_files *= temp  # multiply
for n in range(len(nested_variable_density_list)):
    temp = len(nested_variable_density_list[n])
    total_generated_files *= temp  # multiply
```

```
print('Will vary a total of %i variables' % number_layer_variables)
print('A total of %i files will be generated\n' % total_generated_files)

# Generate a nested list that contains all the combination of variable values
total_variable_list = nested_variable_thick_list + nested_variable_density_list
total_nested_variable_list = []
for l in itertools.product(*total_variable_list):
    total_nested_variable_list.append(list(l))

# Generate the session files
dt_now = str(datetime.now())  # grab the current time
dt_now = dt_now[:16]  # only to the millisecond
dt = dt_now.replace(':', '-')  # formatting
folder_name = 'session files ' + dt

# string for folder named session files + the current time
os.mkdir(folder_name)  # generate such folder
current_folder_dir = str(os.getcwd()) + '\\' + folder_name

# define the directory of the current folder

for n in range(total_generated_files):

    file_name = '_'.join(str(e) for e in total_nested_variable_list[n])
    if total_generated_files == 1:
        file_name = 'SESSION FILE'

    with open(current_folder_dir + '\\%s.txt' % file_name, 'w') as session_file:
        x_period = 0
        print('-- SESSA sessa files generated by session_file_mk2', file=session_file)
        print('-- Generated on {}\n'.format(dt), file=session_file)

        print('\\PROJECT RESET', file=session_file)  # reset SESSA settings
        print('\\SAMPLE RESET', file=session_file)  # reset SESSA settings
        print('\\GEOMETRY RESET', file=session_file)  # reset SESSA settings
        print('\\SPECTROMETER RESET\n', file=session_file)  # reset SESSA settings
        if x_source == '2':
            print('\\SOURCE SET MGKA', file=session_file)
        if x_source == '3':
            print('\\SOURCE SET ZRMZ', file=session_file)
        print('\\GEOMETRY SET ANALYZER THETA {} GEOMETRY 1'.format(analysis_axis), file=session_file)  #
analyzer angle
        print('\\GEOMETRY SET SOURCE THETA {} GEOMETRY 1'.format(x_ray_incident), file=session_file)  # source
angle
        print('\\GEOMETRY SET SAMPLE THETA {} GEOMETRY 1'.format(sample_surface), file=session_file)  # sample
angle
        print('\\GEOMETRY SET APERTURE UTHETA {} GEOMETRY 1'.format(aperture_angle * 2), file=session_file)  #
A. angle
        print('\\SAMPLE MORPHOLOGY SET LAYERED_SPHERES\n', file=session_file)

        print('\\SAMPLE MORPHOLOGY SET X_PERIOD {}'.format(float(core_diameter) * 100), file=session_file)
        print('\\SAMPLE MORPHOLOGY SET Y_PERIOD {}\n'.format(float(core_diameter) * 100), file=session_file)

        if single_particle_TF == 'T':
            print('\\Model set single true', file=session_file)
        if transport_approx_TF == 'T':
            print('\\MODEL SET TA true', file=session_file)
        if transport_approx_TF == 'F':
            print('\\MODEL SET TA false', file=session_file)
        if sla_TF == 'T':
            print('\\MODEL SET SLA true', file=session_file)  # set SLA setting
        if sla_TF == 'F':
```

```
        print('\\MODEL SET SLA false\n', file=session_file)  # set SLA setting

    print('\\MODEL AUTO NCOL REGION 1', file=session_file)  # set region
    print('\\SAMPLE MORPHOLOGY SET RSA {}'.format(rsa_value), file=session_file)
    print('\\MODEL SET CONVERGENCE {}\n'.format(convergence_factor), file=session_file)  # set convergence factor
    print('\\SAMPLE SET MATERIAL {} LAYER 1'.format(core_composition), file=session_file)  # set core comp.
    print('\\SAMPLE SET MATERIAL {} LAYER 2'.format(sub_comp), file=session_file)
    print('\\SAMPLE SET THICKNESS {} LAYER 1\n'.format(core_diameter), file=session_file)  # set core diameter.
    if vary_thick_TF_list[0] is False:
        x_period = float(core_diameter)
    for nn in range(len(shell_comp_list)):  # loop through all shells
        print('\\SAMPLE ADD LAYER {} THICKNESS {} ABOVE 0'.format(shell_comp_list[nn], shell_thick_list[nn]),
              file=session_file)

    print('', file=session_file)  # spacer

    for nn in range(len(density_list)):  # loop through all shells to set density
        if density_list[nn] != 'Default':
            print('\\SAMPLE SET DENSITY {}e+022 LAYER {}'.format(density_list[nn], len(density_list)-nn),
                  file=session_file)  # set density for the desired shells

    print('', file=session_file)  # spacer
    k = 0  # counter
    for kk in range(len(vary_thick_TF_list)):
        if vary_thick_TF_list[kk] is False and kk != 0:
            x_period += float(shell_thick_list[kk-1])
        if vary_thick_TF_list[kk] is True:  # If a layer requires variations
            print('\\SAMPLE SET THICKNESS {} LAYER {}'.format((total_nested_variable_list[n][k]),
                  abs(kk - len(vary_thick_TF_list))), file=session_file)
            x_period += total_nested_variable_list[n][k]
            k += 1

    for dd in range(len(vary_density_TF_list)):
        if vary_density_TF_list[dd] is True:
            print('\\SAMPLE SET DENSITY {}e+022 LAYER {}'.format((total_nested_variable_list[n][k]),
                  abs(dd - len(vary_density_TF_list))), file=session_file)
            k += 1
    print('', file=session_file)  # spacer

    print('\\SAMPLE MORPHOLOGY SET X_PERIOD {}'.format(x_period), file=session_file)
    print('\\SAMPLE MORPHOLOGY SET Y_PERIOD {}'.format(x_period), file=session_file)
    print('\\SAMPLE MORPHOLOGY SET Z_HEIGHT {}\n'.format(x_period / 2), file=session_file)

# End of code
```

Appendix D.4 SCRIPT FOR SESSA AUTOMATION AND CAPTURING RESULTS

```
# Goal: automates SESSA simulations and collects simulated result. Python version 3

import os
import glob
import subprocess
import sys
import csv
from datetime import datetime
import re
```

```
sessa_dir = 'C:\\Program Files (x86)\\SESSA V2.0\\bin'
sessa_session_dir = 'C:\\temp'
# The folder where session files are located, grabs all session files' path into a
list
sessa_file_path = glob.glob('C:\\temp\\*.SES')
# Intended directory for the result to be saved in, create the folder first
sessa_result_dir = 'C:\\temp\\result\\'
session_file_name = []  # creates empty list for store file names
for (dirpath, firnames, filenames) in os.walk(sessa_session_dir):
    session_file_name.extend(filenames)  # save file names into a list
    break
if len(session_file_name) is 0:
    sys.exit('Error, no session file found in the target folder')
# Write to the session file and generate an line at the end for saving result
for p in range(len(session_file_name)):
    with open(sessa_file_path[p], 'a') as session_file:
        print('\\ MODEL SIMULATE', file=session_file)
        print('\\MODEL SAVE INTENSITIES {}{}'.format(sessa_result_dir,
session_file_name[p]), file=session_file)

# Calls SESSA via cmd and execute the session files
os.chdir(sessa_dir)
for i in range(len(sessa_file_path)):
    print('Now executing session file: "%s," ' % session_file_name[i] + str(i+1) + '
out of '+str(len(session_file_name)))
    subprocess.call('sessa.exe -s "%s"' % sessa_file_path[i])
# NOTE: The session files now have extra commend generated by this script (Model
simulate and Model Save....)

# The script below will read through all raw result file and generate a csv file that
contains raw photoelectron intensity for analysis

# For sorting the files in order
numbers = re.compile(r'(\d+)')
def numericalsort(value):
    parts = numbers.split(value)
    parts[1::2] = map(int, parts[1::2])
    return parts

# Directory of all result files
sessa_result_dir = 'C:\\temp\\result\\'

# The folder where result files are located, grabs all result files' path into a list
result_file_path = sorted(glob.glob('C:\\temp\\result\\*.adf'), key=numericalsort)

result_file_names = []  # creates empty list to store file names
for (dirpath, firnames, filenames) in os.walk(sessa_result_dir):
    result_file_names.extend(filenames)  # save file names into a list
    break

f = open(result_file_path[0])  # Grab the simulated peaks
result_header = (f.readline().split(','))
f.close()
peak_names = result_header[-1].split(' ')
peak_names = [w.replace('\n', '') for w in peak_names]
# remove the extra "\n" from end of the peak name
peak_names.insert(0, '')  # empty string at the beginning for formatting
del peak_names[0:3]  # remove non-peak information

result = []  # empty list for storing peak result
for p in range(len(result_file_path)):  # loop for all files
    f = open(result_file_path[p])
```

```
    f.readline()  # skip the first line (which is just header information)
    temp = (f.readline().split(' '))  # Read space delimited result
    temp = temp[24:]  # Remove extra result
    del temp[-1]  # Remove extra result
    temp.insert(0, result_file_names[p])
    result.append(temp)  # Add to result list
    f.close()

# Now, write into csv file for
os.chdir(sessa_result_dir)  # Point to fold to generate csv file
dt = str(datetime.now())  # grab current time
dt = dt.split()  # split date and time

with open('result.csv', 'w', newline='') as csvfile:  # Saving the result into a csv
(excel) file
    writer = csv.writer(csvfile, delimiter=',')
    writer.writerow([])
    writer.writerow(['date', 'time'])
    writer.writerow(dt)
    writer.writerow([])
    writer.writerow(peak_names)
    writer.writerows(result)

# End of code
```

REFERENCES

1. Li J, Cai P, Shalviri A, et al. A multifunctional polymeric nanotheranostic system delivers doxorubicin and imaging agents across the blood-brain barrier targeting brain metastases of breast cancer. *ACS Nano*. 2014;8(10):9925-9940. doi:10.1021/nn501069c.
2. Wang AZ, Langer R, Farokhzad OC. Nanoparticle Delivery of Cancer Drugs. *Annu Rev Med*. 2012;63(1):185-198. doi:10.1146/annurev-med-040210-162544.
3. Ghosh P, Han G, De M, Kim CK, Rotello VM. Gold nanoparticles in delivery applications. *Adv Drug Deliv Rev*. 2008;60(11):1307-1315. doi:10.1016/j.addr.2008.03.016.
4. Rosi NL, Mirkin CA. Nanostructures in biodiagnostics. *Chem Rev*. 2005;105(4):1547-1562. doi:10.1021/cr030067f.
5. Zhang L, Gu F, Chan J, Wang A, Langer R, Farokhzad O. Nanoparticles in Medicine: Therapeutic Applications and Developments. *Clin Pharmacol Ther*. 2008;83(5):761-769. doi:10.1038/sj.clpt.6100400.
6. Vance ME, Kuiken T, Vejerano EP, McGinnis SP, Hochella MF, Hull DR. Nanotechnology in the real world: Redeveloping the nanomaterial consumer products inventory. *Beilstein J Nanotechnol*. 2015;6(1):1769-1780. doi:10.3762/bjnano.6.181.
7. EPA. Nanotechnology white paper. *US Environ Prot Agency, EPA 100/B-07/001*. 2007;(February):136. doi:EPA 100/B-07/001.
8. Kroll A, Pillukat MH, Hahn D, Schnekenburger J. Current in vitro methods in nanoparticle risk assessment: Limitations and challenges. *Eur J Pharm Biopharm*. 2009;72(2):370-377. doi:10.1016/j.ejpb.2008.08.009.
9. Sanvicens N, Marco MP. Multifunctional nanoparticles - properties and prospects for their use in human medicine. *Trends Biotechnol*. 2008;26(8):425-433. doi:10.1016/j.tibtech.2008.04.005.
10. Baer DR, Engelhard MH, Johnson GE, et al. Surface characterization of nanomaterials and nanoparticles: Important needs and challenging opportunities. *J Vac Sci Technol A Vacuum, Surfaces, Film*. 2013;31(5):50820. doi:10.1116/1.4818423.
11. Belsey NA, Shard AG, Minelli C. Analysis of protein coatings on gold nanoparticles by XPS and liquid-based particle sizing techniques. *Biointerphases*. 2015;10(1):19012. doi:10.1116/1.4913566.
12. Baer DR, Amonette JE, Engelhard MH, et al. Characterization challenges for nanomaterials. *Surf interface Anal*. 2008;40(3-4):529-537. doi:10.1002/sia.2726.
13. Jiang W, Kim BYS, Rutka JT, Chan WCW. Nanoparticle-mediated cellular response is size-dependent. *Nat Nanotechnol*. 2008;3(3):145-150. doi:10.1038/nnano.2008.30.
14. Unfried K, Albrecht C, Klotz LO, et al. Cellular responses to nanoparticles: Target structures and mechanisms. *Nanotoxicology*. 2007;1(1):52-71. doi:10.1080/00222930701314932.
15. Gaumet M, Vargas A, Gurny R, Delie F. Nanoparticles for drug delivery: The need for precision in reporting particle size parameters. *Eur J Pharm Biopharm*. 2008;69(1):1-9. doi:10.1016/j.ejpb.2007.08.001.
16. Cho EJ, Holback H, Liu KC, Abouelmagd SA, Park J, Yeo Y. Nanoparticle characterization: State of the art, challenges, and emerging technologies. *Mol Pharm*. 2013;10(6):2093-2110. doi:10.1021/mp300697h.

17. Mahmoudi M, Lynch I, Ejtehadi MR, Monopoli MP, Bombelli FB, Laurent S. Protein-nanoparticle interactions: Opportunities and challenges. *Chem Rev*. 2011;111(9):5610-5637. doi:10.1021/cr100440g.
18. Schnyder A, Krähenbühl S, Drewe J, Huwyler J. Targeting of daunomycin using biotinylated immunoliposomes: pharmacokinetics, tissue distribution and in vitro pharmacological effects. *J Drug Target*. 2005;13(5):325-335. doi:10.1080/10611860500206674.
19. Kukowska-Latallo JF, Candido KA, Cao Z, et al. Nanoparticle targeting of anticancer drug improves therapeutic response in animal model of human epithelial cancer. *Cancer Res*. 2005;65(12):5317-5324. doi:10.1158/0008-5472.CAN-04-3921.
20. Bergen JM, Von Recum HA, Goodman TT, Massey AP, Pun SH. Gold nanoparticles as a versatile platform for optimizing physicochemical parameters for targeted drug delivery. *Macromol Biosci*. 2006;6(7):506-516. doi:10.1002/mabi.200600075.
21. Chudzicki M, Werner WSM, Shard AG, Wang Y-CC, Castner DG, Powell CJ. Evaluating the Internal Structure of Core-Shell Nanoparticles Using X-ray Photoelectron Intensities and Simulated Spectra. *J Phys Chem C*. 2015;119(31):17687-17696. doi:10.1021/acs.jpcc.5b04517.
22. Wang YC, Engelhard MH, Baer DR, Castner DG. Quantifying the Impact of Nanoparticle Coatings and Nonuniformities on XPS Analysis: Gold/Silver Core-Shell Nanoparticles. *Anal Chem*. 2016;88(7):3917-3925. doi:10.1021/acs.analchem.6b00100.
23. Baer DR, Wang Y-C, Castner DG. Use of XPS to Quantify Thickness of Coatings on Nanoparticles. *Micros Today*. 2016;24(2):40-45. doi:10.1017/S1551929516000109.
24. Belsey NA, Cant DJH, Minelli C, et al. Versailles Project on Advanced Materials and Standards Interlaboratory Study on Measuring the Thickness and Chemistry of Nanoparticle Coatings Using XPS and LEIS. *J Phys Chem C*. 2016;120(42):24070-24079. doi:10.1021/acs.jpcc.6b06713.
25. Cant DJH, Wang YC, Castner DG, Shard AG. A technique for calculation of shell thicknesses for core-shell-shell nanoparticles from XPS data. *Surf Interface Anal*. 2016;48(5):274-282. doi:10.1002/sia.5923.
26. Häkkinen H. The gold–sulfur interface at the nanoscale. *Nat Chem*. 2012;4(6):443-455. doi:10.1038/nchem.1352.
27. Zanchet D, Hall BD, Ugarte D. Structure Population in Thiol-Passivated Gold Nanoparticles. *J Phys Chem B*. 2000;104(47):11013-11018. doi:10.1021/jp0017644.
28. Badia A, Cuccia L, Demers L, Morin F, Lennox RB. Structure and dynamics in alkanethiolate monolayers self-assembled on gold nanoparticles: A DSC, FT-IR, and deuterium NMR study. *J Am Chem Soc*. 1997;119(11):2682-2692. doi:10.1021/ja963571t.
29. Hostetler MJ, Stokes JJ, Murray RW, Hill C, Carolina N. Infrared Spectroscopy of Three-Dimensional Self-Assembled Monolayers: a N-Alkanethiolate Monolayers on Gold Cluster Compounds. *Langmuir*. 1996;12(15):3604-3612. doi:10.1021/la960249n.
30. Hostetler MJ, Wingate JE, Zhong C-J, et al. Alkanethiolate Gold Cluster Molecules with Core Diameters from 1.5 to 5.2 nm: Core and Monolayer Properties as a Function of Core Size. *Langmuir*. 1998;14(1):17-30. doi:10.1021/la970588w.
31. Jackson AM, Hu Y, Silva PJ, Stellacci F. From homoligand- to mixed-ligand- monolayer-protected metal nanoparticles: A scanning tunneling microscopy investigation. *J Am Chem Soc*. 2006;128(34):11135-11149. doi:10.1021/ja061545h.
32. Biebuyck HA, Bain CD, Whitesides GM. Comparison of Organic Monolayers on

Polycrystalline Gold Spontaneously Assembled from Solutions Containing Dialkyl Disulfides or Alkanethiols. *Langmuir*. 1994;10(6):1825-1831. doi:10.1021/la00018a034.
33. Bain CD, Whitesides GM. Formation of monolayers by the coadsorption of thiols on gold: Variation in the length of the alkyl chain. *J Am Chem Soc*. 1989;111(18):7164-7175. doi:10.1021/ja00200a040.
34. Decher G. Fuzzy Nanoassemblies: Toward Layered Polymeric Multicomposites. *Science (80-)*. 1997;277(5330):1232-1237. doi:10.1126/science.277.5330.1232.
35. Plant AL. Self-Assembled Phospholipid/Alkanethiol Biomimetic Bilayers on Gold. *Langmuir*. 1993;9(11):2764-2767. doi:10.1021/la00035a004.
36. Staub R, Toerker M, Fritz T, Schmitz-Hübsch T, Sellam F, Leo K. Scanning tunneling microscope investigations of organic heterostructures prepared by a combination of self-assembly and molecular beam epitaxy. *Surf Sci*. 2000;445(2-3):368-379. doi:10.1016/S0039-6028(99)01083-3.
37. Love JC, Estroff LA, Kriebel JK, Nuzzo RG, Whitesides GM. Self-assembled monolayers of thiolates on metals as a form of nanotechnology. *Chem Rev*. 2005;105(4):1103-1169. doi:10.1021/cr0300789.
38. Reis KJ, Ayoub EM, Boyle MD. Streptococcal Fc receptors. I. Isolation and partial characterization of the receptor from a group C streptococcus. *J Immunol*. 1984;132(6):3091-3097. http://www.ncbi.nlm.nih.gov/pubmed/6233367.
39. Myhre EB, Kronvall G. Heterogeneity of nonimmune immunoglobulin Fc reactivity among gram-positive cocci: description of three major types of receptors for human immunoglobulin G. *Infect Immun*. 1977;17(3):475-482.
40. Alexander P, Fahnestock S, Lee T, Orban J, Bryan P. Thermodynamic analysis of the folding of the streptococcal protein G IgG- binding domains B1 and B2: Why small proteins tend to have high denaturation temperatures. *Biochemistry*. 1992;31(14):3597-3603. doi:10.1021/bi00129a007.
41. Blanco FJ, Serrano L. Folding of Protein G B1 Domain Studied by the Conformational Characterization of Fragments Comprising Its Secondary Structure Elements. *Eur J Biochem*. 1995;230(2):634-649. doi:10.1111/j.1432-1033.1995.0634h.x.
42. Sheinerman FB, Brooks CL. Calculations on folding of segment B1 of streptococcal protein G. *J Mol Biol*. 1998;278(2):439-456. doi:10.1006/jmbi.1998.1688.
43. Sloan DJ, Hellinga HW. Dissection of the protein G B1 domain binding site for human IgG Fc fragment. *Protein Sci*. 1999;8(8):1643-1648. doi:10.1110/ps.8.8.1643.
44. Kobayashi N, Honda S, Yoshii H, Uedaira H, Munekata E. Complement assembly of two fragments of the streptococcal protein G B1 domain in aqueous solution. *FEBS Lett*. 1995;366(2-3):99-103. doi:10.1016/0014-5793(95)00503-2.
45. Fesinmeyer RM, Hudson FM, Andersen NH. Enhanced hairpin stability through loop design: The case of the protein G B1 domain hairpin. *J Am Chem Soc*. 2004;126(23):7238-7243. doi:10.1021/ja0379520.
46. Baugh L, Weidner T, Baio JE, et al. Probing the orientation of surface-immobilized protein G B1 using ToF-SIMS, sum frequency generation, and NEXAFS spectroscopy. *Langmuir*. 2010;26(21):16434-16441. doi:10.1021/la1007389.
47. Baio JE, Weidner T, Baugh L, Gamble LJ, Stayton PS, Castner DG. Probing the orientation of electrostatically immobilized protein G B1 by time-of-flight secondary ion spectrometry, sum frequency generation, and near-edge X-ray adsorption fine structure spectroscopy. *Langmuir*. 2012;28(4):2107-2112. doi:10.1021/la203907t.

48. Baio JE, Weidner T, Samuel NT, et al. Multitechnique characterization of adsorbed peptide and protein orientation: LK310 and Protein G B1. *J Vac Sci Technol B, Nanotechnol Microelectron Mater Process Meas Phenom*. 2010;28(4):C5D1-C5D8. doi:10.1116/1.3456176.
49. Turkevich J, Stevenson PC, Hillier J, et al. A study of the nucleation and growth processes in the synthesis of colloidal gold. *Discuss Faraday Soc*. 1951;11(c):55-75. doi:10.1039/DF9511100055.
50. FRENS G. Controlled Nucleation for the Regulation of the Particle Size in Monodisperse Gold Suspensions. *Nat Phys Sci*. 1973;241(105):20-22. doi:10.1038/physci241020a0.
51. Polte J, Ahner TT, Delissen F, et al. Mechanism of gold nanoparticle formation in the classical citrate synthesis method derived from coupled in situ XANES and SAXS evaluation. *J Am Chem Soc*. 2010;132(4):1296-1301. doi:10.1021/ja906506j.
52. Kimling J, Maier M, Okenve B, Kotaidis V, Ballot H, Plech A. Turkevich method for gold nanoparticle synthesis revisited. *J Phys Chem B*. 2006;110(32):15700-15707. doi:10.1021/jp061667w.
53. Williams DB, Carter CB. The Transmission Electron Microscope. *Transm Electron Microsc*. 1996:3-22. doi:10.1007/978-1-4757-2519-3_1.
54. Einstein A. Über einen die Erzeugung und Verwandlung des Lichtes betreffenden heuristischen Gesichtspunkt. *Ann Phys*. 1905;322(6):132-148. doi:10.1002/andp.19053220607.
55. Vickerman JC, Gilmore I. *Surface Analysis– The Principal Techniques*.; 2009. doi:10.1002/9780470721582.
56. Benninghoven A. Chemical Analysis of Inorganic and Organic Surfaces and Thin Films by Static Time-of-Flight Secondary Ion Mass Spectrometry (TOF-SIMS). *Angew Chemie Int Ed English*. 1994;33(10):1023-1043. doi:10.1002/anie.199410231.
57. Thompson PM. Quantitative surface analysis of organic polymer blends using a time-of-flight static secondary ion mass spectrometer. *Anal Chem*. 1991;63(21):2447-2456. doi:10.1021/ac00021a012.
58. Ferrari S, Ratner BD. ToF-SIMS quantification of albumin adsorbed on plasma-deposited fluoropolymers by partial least-squares regression. *Surf Interface Anal*. 2000;29(12):837-844. doi:10.1002/1096-9918(200012)29:12<837::AID-SIA937>3.0.CO;2-O.
59. Belu AM, Graham DJ, Castner DG. Time-of-flight secondary ion mass spectrometry: Techniques and applications for the characterization of biomaterial surfaces. *Biomaterials*. 2003;24(21):3635-3653. doi:10.1016/S0142-9612(03)00159-5.
60. Mantus DS, Ratner BD, Carlson BA, et al. Static secondary ion mass spectrometry of adsorbed proteins. *Anal Chem*. 1993;65(10):1431-1438. doi:10.1021/ac00058a021.
61. Lhoest JB, Wagner MS, Tidwell CD, Castner DG. Characterization of adsorbed protein films by time of flight secondary ion mass spectrometry. *J Biomed Mater Res*. 2001;57(3):432-440. doi:10.1002/1097-4636(20011205)57:3<432::AID-JBM1186>3.0.CO;2-G.
62. Smekal W, Werner WSM, Powell CJ. Simulation of electron spectra for surface analysis (SESSA): A novel software tool for quantitative Auger-electron spectroscopy and X-ray photoelectron spectroscopy. *Surf Interface Anal*. 2005;37(11):1059-1067. doi:10.1002/sia.2097.
63. Werner WSM, Smekal W, Powell CJ, J. Powell C. NIST Database for the Simulation of Electron Spectra for Surface Analysis (SESSA) Users â€™ Guide. *Natl Inst Stand*

Technol. 2014.
64. Werner W. Influence of multiple elastic and inelastic scattering on photoelectron line shape. *Phys Rev B*. 1995;52(4):2964-2975. doi:10.1103/PhysRevB.52.2964.
65. Werner WSMM. Electron transport in solids for quantitative surface analysis. *Surf Interface Anal*. 2001;31(3):141-176. doi:10.1002/sia.973.
66. Gries WH, Werner W. Take-off angle and film thickness dependences of the attenuation length of X-ray photoelectrons by a trajectory reversal method. *Surf Interface Anal*. 1990;16(1-12):149-153. doi:10.1002/sia.740160129.
67. Techane SD, Gamble LJ, Castner DG. Multitechnique characterization of self-assembled carboxylic acid-terminated alkanethiol monolayers on nanoparticle and flat gold surfaces. *J Phys Chem C*. 2011;115(19):9432-9441. doi:10.1021/jp201213g.
68. Chan WCW, Nie S. Quantum Dot Bioconjugates for Ultrasensitive Nonisotopic Detection. *Science (80-)*. 1998;281(5385):2016-2018. doi:10.1126/science.281.5385.2016.
69. Li YP, Pei YY, Zhang XY, et al. PEGylated PLGA nanoparticles as protein carriers: Synthesis, preparation and biodistribution in rats. *J Control Release*. 2001;71(2):203-211. doi:10.1016/S0168-3659(01)00218-8.
70. Prabaharan M, Grailer JJ, Pilla S, Steeber DA, Gong S. Gold nanoparticles with a monolayer of doxorubicin-conjugated amphiphilic block copolymer for tumor-targeted drug delivery. *Biomaterials*. 2009;30(30):6065-6075. doi:10.1016/j.biomaterials.2009.07.048.
71. Tamura M, Fujihara H. Chiral Bisphosphine BINAP-Stabilized Gold and Palladium Nanoparticles with Small Size and Their Palladium Nanoparticle-Catalyzed Asymmetric Reaction. *J Am Chem Soc*. 2003;125(51):15742-15743. doi:10.1021/ja0369055.
72. Lynch I, Dawson KA. Protein-nanoparticle interactions. *Nano Today*. 2008;3(1-2):40-47. doi:10.1016/S1748-0132(08)70014-8.
73. Rafati A, ter Veen HRJ, Castner DG, Ter Veen R, Castner DG. Low Energy Ion Scattering: Determining Overlayer Thickness for Functionalized Gold Nanoparticles. *Surf interface Anal*. 2013;45(11):1737-1741. doi:10.1002/sia.5315.
74. Webster DM, Sundaram P, Byrne ME. Injectable nanomaterials for drug delivery: Carriers, targeting moieties, and therapeutics. *Eur J Pharm Biopharm*. 2013;84(1):1-20. doi:10.1016/j.ejpb.2012.12.009.
75. Pan D, Pramanik M, Senpan A, Wickline SA, Wang L V., Lanza GM. A facile synthesis of novel self-assembled gold nanorods designed for near-infrared imaging. *J Nanosci Nanotechnol*. 2010;10(12):8118-8123. doi:10.1166/jnn.2010.3034.
76. Yan C, Wu Y, Feng J, et al. Anti-αvβ3 antibody guided three-step pretargeting approach using magnetoliposomes for molecular magnetic resonance imaging of breast cancer angiogenesis. *Int J Nanomedicine*. 2013;8:245-255. doi:10.2147/IJN.S38678.
77. Yang M, Cheng K, Qi S, et al. Affibody modified and radiolabeled gold-Iron oxide hetero-nanostructures for tumor PET, optical and MR imaging. *Biomaterials*. 2013;34(11):2796-2806. doi:10.1016/j.biomaterials.2013.01.014.
78. Shen M, Rusling J, Dixit CK. Site-selective orientated immobilization of antibodies and conjugates for immunodiagnostics development. *Methods*. 2016;116:95-111. doi:10.1016/j.ymeth.2016.11.010.
79. Brogan KL, Wolfe KN, Jones PA, Schoenfisch MH. Direct oriented immobilization of F(ab) antibody fragments on gold. *Anal Chim Acta*. 2003;496(1-2):73-80.

doi:10.1016/S0003-2670(03)00991-7.
80. Lee W, Oh B-K, Lee H, Choi J-W. Immobilization of antibody fragment for immunosensor application based on surface plasmon resonance. *Colloids Surfaces B Biointerfaces*. 2005;40:143-148. doi:10.1016/j.colsurfb.2004.10.021.
81. Karyakin AA, Presnova G V., Rubtsova MY, Egorov AM. Oriented immobilization of antibodies onto the gold surfaces via their native thiol groups. *Anal Chem*. 2000;72(16):3805-3811. doi:10.1021/ac9907890.
82. Handlogten MW, Kiziltepe T, Moustakas DT, Bilgier B. Design of a heterobivalent ligand to inhibit IgE clustering on mast cells. *Chem Biol*. 2011;18(9):1179-1188. doi:10.1016/j.chembiol.2011.06.012.
83. Alves NJ, Mustafaoglu N, Bilgicer B. Oriented antibody immobilization by site-specific UV photocrosslinking of biotin at the conserved nucleotide binding site for enhanced antigen detection. *Biosens Bioelectron*. 2013;49:387-393. doi:10.1016/j.bios.2013.05.052.
84. Wang H, Castner DG, Ratner BD, Jiang S. Probing the orientation of surface-immobilized immunoglobulin G by time-of-flight secondary ion mass spectrometry. *Langmuir*. 2004;20(5):1877-1887. doi:10.1021/la035376f.
85. Chen S, Liu L, Zhou J, Jiang S. Controlling antibody orientation on charged self-assembled monolayers. *Langmuir*. 2003;19(7):2859-2864. doi:10.1021/la026498v.
86. Neubert H, Jacoby ES, Bansal SS, Iles RK, Cowan DA, Kicman AT. Enhanced affinity capture MALDI-TOF MS: Orientation of an immunoglobulin G using recombinant protein G. *Anal Chem*. 2002;74(15):3677-3683. doi:10.1021/ac025558z.
87. de Juan-Franco E, Caruz A, Pedrajas JR, Lechuga LM. Site-directed antibody immobilization using a protein A–gold binding domain fusion protein for enhanced SPR immunosensing. *Analyst*. 2013;138(7):2023. doi:10.1039/c3an36498d.
88. Vashist SK, Dixit CK, MacCraith BD, O'Kennedy R. Effect of antibody immobilization strategies on the analytical performance of a surface plasmon resonance-based immunoassay. *Analyst*. 2011;136(21):4431. doi:10.1039/c1an15325k.
89. Welch NG, Scoble JA, Muir BW, Pigram PJ. Orientation and characterization of immobilized antibodies for improved immunoassays (Review). *Biointerphases*. 2017;12(2):02D301. doi:10.1116/1.4978435.
90. Trilling AK, Beekwilder J, Zuilhof H. Antibody orientation on biosensor surfaces: a minireview. *Analyst*. 2013;138(6):1619-1627. doi:10.1039/c2an36787d.
91. Castner DG. Biomedical surface analysis: Evolution and future directions (Review). *Biointerphases*. 2017;12(2):02C301. doi:10.1116/1.4982169.
92. Tidwell CD, Castner DG, Golledge SL, et al. Static time-of-flight secondary ion mass spectrometry and x-ray photoelectron spectroscopy characterization of adsorbed albumin and fibronectin films. *Surf Interface Anal*. 2001;31(8):724-733. doi:10.1002/sia.1101.
93. Baio JE, Cheng F, Ratner DM, Stayton PS, Castner DG. Probing orientation of immobilized humanized anti-lysozyme variable fragment by time-of-flight secondary-ion mass spectrometry. *J Biomed Mater Res - Part A*. 2011;97 A(1):1-7. doi:10.1002/jbm.a.33025.
94. Harder P, Grunze* M, Dahint R, et al. Molecular Conformation in Oligo(ethylene glycol)-Terminated Self-Assembled Monolayers on Gold and Silver Surfaces Determines Their Ability To Resist Protein Adsorption. *J Phys Chem B*. 1998;102(2):426-436. doi:10.1021/jp972635z.
95. Feldman K, Hahner G, Spencer ND, Harder P, Grunze M. Probing resistance to protein

adsorption of oligo(ethylene glycol)- terminated self-assembled monolayers by scanning force microscopy. *J Am Chem Soc*. 1999;121(43):10134-10141. doi:10.1021/ja991049b.
96. Andruzzi L, Senaratne W, Hexemer A, et al. Oligo(ethylene glycol) containing polymer brushes as bioselective surfaces. *Langmuir*. 2005;21(6):2495-2504. doi:10.1021/la047574s.
97. Wagner MS, Castner DG. Analysis of adsorbed proteins by static time-of-flight secondary ion mass spectrometry. *Appl Surf Sci*. 2004;231-232:366-376. doi:10.1016/j.apsusc.2004.03.100.
98. Michel R, Pasche S, Textor M, Castner DG. Influence of PEG architecture on protein adsorption and conformation. *Langmuir*. 2005;21(26):12327-12332. doi:10.1021/la051726h.
99. Powell CJJ, Jablonski A. Progress in quantitative surface analysis by X-ray photoelectron spectroscopy: Current status and perspectives. *J Electron Spectros Relat Phenomena*. 2010;178-179(C):331-346. doi:10.1016/j.elspec.2009.05.004.
100. J. F. Watts JW. *An Introduction of Surface Analysis and XPS*. Vol 27.; 2003. doi:10.1002/0470867930.
101. Brundle CR, Conti G, Mack P. XPS and angle resolved XPS, in the semiconductor industry: Characterization and metrology control of ultra-thin films. *J Electron Spectros Relat Phenomena*. 2010;178-179(C):433-448. doi:10.1016/j.elspec.2010.03.008.
102. Torelli MD, Putans RA, Tan Y, Lohse SE, Murphy CJ, Hamers RJ. Quantitative determination of ligand densities on nanomaterials by X-ray photoelectron spectroscopy. *ACS Appl Mater Interfaces*. 2015;7(3):1720-1725. doi:10.1021/am507300x.
103. Tenne R, Margulis L, Genut M, Hodes G. Polyhedral and cylindrical structures of tungsten disulphide. *Nature*. 1992;360(6403):444-446. doi:10.1038/360444a0.
104. Remškar M, Viršek M, Mrzel A. The MoS2 nanotube hybrids. *Appl Phys Lett*. 2009;95(13). doi:10.1063/1.3240892.
105. Tougaard S. Energy loss in XPS: Fundamental processes and applications for quantification, non-destructive depth profiling and 3D imaging. *J Electron Spectros Relat Phenomena*. 2010;178-179(C):128-153. doi:10.1016/j.elspec.2009.08.005.
106. Baer DR, Engelhard MH. XPS analysis of nanostructured materials and biological surfaces. *J Electron Spectros Relat Phenomena*. 2010;178-179(C):415-432. doi:10.1016/j.elspec.2009.09.003.
107. Grainger DWW, Castner DGG. Nanobiomaterials and nanoanalysis: Opportunities for improving the science to benefit biomedical technologies. *Adv Mater*. 2008;20(5):867-877. doi:10.1002/adma.200701760.
108. Giesbers M, Marcelis ATM, Zuilhof H. Simulation of XPS C1s spectra of organic monolayers by quantum chemical methods. *Langmuir*. 2013;29(15):4782-4788. doi:10.1021/la400445s.
109. Zhang F, Wang P, Koberstein J, Khalid S, Chan SW. Cerium oxidation state in ceria nanoparticles studied with X-ray photoelectron spectroscopy and absorption near edge spectroscopy. *Surf Sci*. 2004;563(1-3):74-82. doi:10.1016/j.susc.2004.05.138.
110. Techane S, Baer DR, Castner DG. Simulation and modeling of self-assembled monolayers of carboxylic acid thiols on flat and nanoparticle gold surfaces. *Anal Chem*. 2011;83(17):6704-6712. doi:10.1021/ac201175a.
111. Beketov G, Heinrichs B, Pirard JP, Chenakin S, Kruse N. XPS structural characterization of Pd/SiO2 catalysts prepared by cogelation. *Appl Surf Sci*. 2013;287:293-298.

doi:10.1016/j.apsusc.2013.09.145.
112. Mukherjee S, Hazarika A, Santra PK, et al. Determination of internal structures of heterogeneous nanocrystals using variable-energy photoemission spectroscopy. *J Phys Chem C*. 2014;118(28):15534-15540. doi:10.1021/jp504283m.
113. Doh WH, Papaefthimiou V, Dintzer T, Dupuis V, Zafeiratos S. Synchrotron Radiation X-ray Photoelectron Spectroscopy as a Tool To Resolve the Dimensions of Spherical Core/Shell Nanoparticles. *J Phys Chem C*. 2014;118(46):26621-26628. doi:10.1021/jp508895u.
114. Kerkhof FPJM, Moulijn JA. Quantitative analysis of XPS intensities for supported catalysts. *J Phys Chem*. 1979;83(12):1612-1619. doi:10.1021/j100475a011.
115. Romeo M, Bak K, El Fallah J, Le Normand F, Hilaire L. XPS Study of the reduction of cerium dioxide. *Surf Interface Anal*. 1993;20(6):508-512. doi:10.1002/sia.740200604.
116. Fulghum JE, Linton RW. Quantitation of coverages on rough surfaces by XPS: An overview. *Surf Interface Anal*. 1988;13(4):186-192. doi:10.1002/sia.740130404.
117. Cimino a., Gazzoli D, Valigi M. XPS quantitative analysis and models of supported oxide catalysts. *J Electron Spectros Relat Phenomena*. 1999;104(1-3):1-29. doi:10.1016/S0368-2048(98)00300-4.
118. Cumpson PJ, Zalm PC. Thickogram: A method for easy film thickness measurement in XPS. *Surf Interface Anal*. 2000;29(6):403-406. doi:10.1002/1096-9918(200006)29:6<403::AID-SIA884>3.0.CO;2-8.
119. Shard AG, Wang J, Spencer SJ. XPS topofactors: determining overlayer thickness on particles and fibres. *Surf Interface Anal*. 2009;41(7):541-548. doi:10.1002/sia.3044.
120. Frydman A, Castner DG, Schmal M, Campbell CT. A Method for Accurate Quantitative XPS Analysis of Multimetallic or Multiphase Catalysts on Support Particles. *J Catal*. 1995;157(1):133-144. doi:10.1006/jcat.1995.1274.
121. Mohai M, Bertóti I. Calculation of layer thickness on nanotube surfaces from XPS intensity data. In: *Surface and Interface Analysis*. Vol 44. ; 2012:1130-1134. doi:10.1002/sia.4864.
122. Frydman A. Particle and Phase Thicknesses from XPS Analysis of Supported Bimetallic Catalysts: Calcined Co-Rh/Nb2O5. *J Catal*. 1995;152(1):164-178. doi:10.1006/jcat.1995.1070.
123. Shard AG. A straightforward method for interpreting XPS data from core-shell nanoparticles. *J Phys Chem C*. 2012;116(31):16806-16813. doi:10.1021/jp305267d.
124. Tougaard S. QUASES: Software Package for Quantitative XPS/AES of surface Nanostructures by Inelastic Peak Shape Analysis. University of Southern Denmark: Odense, Denmark. http://www.quases.com. Published 2000.
125. Salvat F, Fernández-Varea J, Sempau J. PENELOPE-2011: A code system for Monte Carlo simulation of electron and photon transport. *Work Proc*. 2011:384. doi:10.1.1.78.4492.
126. Werner WSM, Chudzicki M, Smekal W, et al. Interpretation of nanoparticle X-ray photoelectron intensities. *Appl Phys Lett*. 2014;104(24):243106. doi:10.1063/1.4884065.
127. Shipway AN, Katz E, Willner I. Nanoparticle Arrays on Surfaces for Electronic, Optical, and Sensor Applications. *ChemPhysChem*. 2000;1(1):18-52. doi:10.1002/1439-7641(20000804)1:1<18::AID-CPHC18>3.0.CO;2-L.
128. Pankhurst Q a, Connolly J, Jones SK, Dobson J. Applications of magnetic nanoparticles in biomedicine. *J Phys D Appl Phys*. 2003;36(13):R167-R181. doi:10.1088/0022-

3727/36/13/201.
129. Murphy CJ, Sau TK, Gole AM, et al. Anisotropic Metal Nanoparticles: Synthesis, Assembly, and Optical Applications. *J Phys Chem B*. 2005;109(29):13857-13870. doi:10.1021/jp0516846.
130. Thakar R, Chen Y, Snee PT. Efficient emission from core/(Doped) shell nanoparticles: Applications for chemical sensing. *Nano Lett*. 2007;7(11):3429-3432. doi:10.1021/nl0719168.
131. De Jong WH, Borm PJ a. Drug delivery and nanoparticles:applications and hazards. *Int J Nanomedicine*. 2008;3(2):133-149. doi:10.2147/IJN.S596.
132. Powell CJ, Jablonski A. Surface sensitivity of X-ray photoelectron spectroscopy. *Nucl Instruments Methods Phys Res Sect A Accel Spectrometers, Detect Assoc Equip*. 2009;601(1-2):54-65. doi:10.1016/j.nima.2008.12.103.
133. Hansen HS, Tougaard S, Biebuyck H. The adsorption of alkanethiols on gold studied quantitatively by XPS inelastic background analysis. *J Electron Spectros Relat Phenomena*. 1992;58(1-2):141-158. doi:10.1016/0368-2048(92)80013-X.
134. Folkers JP, Laibinis PE, Whitesides GM. Self-Assembled Monolayers of Alkanethiols on Gold: Comparisons of Monolayers Containing Mixtures of Short- and Long-Chain Constituents with CH3 and CH2OH Terminal Groups. *Langmuir*. 1992;8(5):1330-1341. doi:10.1021/la00041a015.
135. Luedtke WD, Landman U. Structure and Thermodynamics of Self-Assembled Monolayers on Gold Nanocrystallites. *J Phys Chem B*. 1998;102(34):6566-6572. doi:10.1021/jp981745i.
136. Daniel M-CCM, Astruc D. Gold Nanoparticles: Assembly, Supramolecular Chemistry, Quantum-Size-Related Properties, and Applications toward Biology, Catalysis, and Nanotechnology. *Chem Rev*. 2004;104(1):293-346. doi:10.1021/cr030698+.
137. Van Hardeveld R, Hartog F. The statistics of surface atoms and surface sites on metal crystals. *Surf Sci*. 1969;15(2):189-230. doi:10.1016/0039-6028(69)90148-4.
138. Schreiber F. Self-assembled monolayers: from simple model systems to biofunctionalized interfaces. *J Phys Condens Matter*. 2004;16(28):R881-R900. doi:10.1088/0953-8984/16/28/R01.
139. Ulman A. Formation and Structure of Self-Assembled Monolayers. *Chem Rev*. 1996;96(4):1533-1554. doi:10.1021/cr9502357.
140. Chechik V, Crooks RM, Stirling CJMM, Chechik BV, Crooks RM, Stirling CJMM. Reactions and reactivity in self-assembled monolayers. *Adv Mater*. 2000;12(16):1161-1171. doi:10.1002/1521-4095(200008)12:16<1161::AID-ADMA1161>3.0.CO;2-C.
141. Samanta D, Sarkar A. Immobilization of bio-macromolecules on self-assembled monolayers: methods and sensor applications. *Chem Soc Rev*. 2011;40(5):2567-2592. doi:10.1039/c0cs00056f.
142. Brust M, Walker M, Bethell D, Schiffrin DJ, Whyman R. Synthesis of thiol-derivatised gold nanoparticles in a two-phase Liquid–Liquid system. *J Chem Soc, Chem Commun*. 1994;0(7):801-802. doi:10.1039/C39940000801.
143. Hu X, Wang T, Wang L, Dong S. Surface-enhanced raman scattering of 4-aminothiophenol self-assembled monolayers in sandwich structure with nanoparticle shape dependence: Off-surface plasmon resonance condition. *J Phys Chem C*. 2007;111(19):6962-6969. doi:10.1021/jp0712194.
144. Orendorff CJ, Gole A, Sau TK, Murphy CJ. Surface-enhanced Raman spectroscopy of

self-assembled monolayers: Sandwich architecture and nanoparticle shape dependence. *Anal Chem*. 2005;77(10):3261-3266. doi:10.1021/ac048176x.

145. Alkilany AM, Murphy CJ. Toxicity and cellular uptake of gold nanoparticles: What we have learned so far? *J Nanoparticle Res*. 2010;12(7):2313-2333. doi:10.1007/s11051-010-9911-8.
146. Porter MD, Bright TB, Allara DL, Chidsey CED. Spontaneously Organized Molecular Assemblies. 4. Structural Characterization of n-Alkyl Thiol Monolayers on Gold by Optical Ellipsometry, Infrared Spectroscopy, and Electrochemistry. *J Am Chem Soc*. 1987;109(12):3559-3568. doi:10.1021/ja00246a011.
147. Nuzzo RG, Korenic EM, Dubois LH. Studies of the temperature-dependent phase behavior of long chain n-alkyl thiol monolayers on gold. *J Chem Phys*. 1990;93(1):767. doi:10.1063/1.459528.
148. Alves CA, Smith EL, Porter MD. Atomic scale imaging of alkanethiolate monolayers at gold surfaces with atomic force microscopy. *J Am Chem Soc*. 1992;114(4):1222-1227. doi:10.1021/ja00030a015.
149. Graham DJ, Ratner BD. Multivariate analysis of TOF-SIMS spectra from dodecanethiol SAM assembly on gold: Spectral interpretation and TOF-SIMS fragmentation processes. *Langmuir*. 2002;18(15):5861-5868. doi:10.1021/la0113062.
150. Ivanov MR, Haes AJ. Anionic functionalized gold nanoparticle continuous full filling separations: Importance of sample concentration. *Anal Chem*. 2012;84(3):1320-1326. doi:10.1021/ac2022376.
151. Lanterna AE, Coronado EA, Granados AM. When nanoparticle size and molecular geometry matter: Analyzing the degree of surface functionalization of gold nanoparticles with sulfur heterocyclic compounds. *J Phys Chem C*. 2012;116(11):6520-6529. doi:10.1021/jp209816g.
152. Ghorai PK, Glotzer SC. Molecular dynamics simulation study of self-assembled monolayers of alkanethiol surfactants on spherical gold nanoparticles. *J Phys Chem C*. 2007;111(43):15857-15862. doi:10.1021/jp0746289.
153. Rafati A, Shard AG, Castner DG. Multitechnique characterization of oligo(ethylene glycol) functionalized gold nanoparticles. *Biointerphases*. 2016;11(4):04B304. doi:10.1116/1.4967216.
154. Himmelhaus M, Eisert F, Buck M, Grunze M. Self-Assembly of *n* -Alkanethiol Monolayers. A Study by IR−Visible Sum Frequency Spectroscopy (SFG). *J Phys Chem B*. 2000;104(3):576-584. doi:10.1021/jp992073e.
155. Zolk M, Eisert F, Pipper J, et al. Solvation of oligo(ethylene glycol)-terminated self-assembled monolayers studied by vibrational sum frequency spectroscopy. *Langmuir*. 2000;16(14):5849-5852. doi:10.1021/la0003239.
156. Zhao X, Leng Y, Cummings PT. Self-assembly of 1,4-benzenedithiolate/tetrahydrofuran on a gold surface: A Monte Carlo simulation study. *Langmuir*. 2006;22(9):4116-4124. doi:10.1021/la0532252.
157. Bain CD, Troughton EB, Tao YT, Evall J, Whitesides GM, Nuzzo RG. Formation of Monolayer Films by the Spontaneous Assembly of Organic Thiols from Solution onto Gold. *J Am Chem Soc*. 1989;111(1):321-335. doi:10.1021/ja00183a049.
158. Baer DR, Gaspar DJ, Nachimuthu P, Techane SD, Castner DG. Application of surface chemical analysis tools for characterization of nanoparticles. *Anal Bioanal Chem*. 2010;396(3):983-1002. doi:10.1007/s00216-009-3360-1.

159. Nel AE, Parak WJ, Chan WCW, et al. Where Are We Heading in Nanotechnology Environmental Health and Safety and Materials Characterization? *ACS Nano*. 2015;9(6):5627-5630. doi:10.1021/acsnano.5b03496.
160. Munusamy P, Wang C, Engelhard MH, et al. Comparison of 20 nm silver nanoparticles synthesized with and without a gold core: Structure, dissolution in cell culture media, and biological impact on macrophages. *Biointerphases*. 2015;10(3):31003. doi:10.1116/1.4926547.
161. Murphy CJ, Gole AM, Stone JW, et al. Gold nanoparticles in biology: Beyond toxicity to cellular imaging. *Acc Chem Res*. 2008;41(12):1721-1730. doi:10.1021/ar800035u.
162. Hassellov M, Readman JW, Ranville JF, Tiede K. Nanoparticle analysis and characterization methodologies in environmental risk assessment of engineered nanoparticles. *Ecotoxicology*. 2008;17(5):344-361. doi:10.1007/s10646-008-0225-x.
163. Zorn G, Dave SR, Gao X, Castner DG. Method for determining the elemental composition and distribution in semiconductor core-shell quantum dots. *Anal Chem*. 2011;83(3):866-873. doi:10.1021/ac102516n.
164. Zorn G, Dave SR, Weidner T, Gao X, Castner DG. Direct characterization of polymer encapsulated CdSe/CdS/ZnS quantum dots. *Surf Sci*. 2016;648:339-344. doi:10.1016/j.susc.2015.10.013.
165. Bell NC, Minelli C, Shard AG. Quantitation of IgG protein adsorption to gold nanoparticles using particle size measurement. *Anal Methods*. 2013;5(18):4591-4601. doi:10.1039/C3AY40771C.
166. Pourcelle V, Devouge S, Garinot M, Préat V, Marchand-Brynaert J. PCL-PEG-based nanoparticles grafted with GRGDS peptide: Preparation and surface analysis by XPS. *Biomacromolecules*. 2007;8(12):3977-3983. doi:10.1021/bm700841y.
167. Shenoy DB, Amiji MM. Poly(ethylene oxide)-modified poly(??-caprolactone) nanoparticles for targeted delivery of tamoxifen in breast cancer. *Int J Pharm*. 2005;293(1-2):261-270. doi:10.1016/j.ijpharm.2004.12.010.
168. Techane SD, Gamble LJ, Castner DG. X-ray photoelectron spectroscopy characterization of gold nanoparticles functionalized with amine-terminated alkanethiols. *Biointerphases*. 2011;6(3):98-104. doi:10.1116/1.3622481.
169. Yang HM, Park CW, Woo MA, et al. HER2/neu antibody conjugated poly(amino acid)-coated iron oxide nanoparticles for breast cancer MR imaging. *Biomacromolecules*. 2010;11(11):2866-2872. doi:10.1021/bm100560m.
170. Gillet JN, Meunier M. General equation for size nanocharacterization of the core-shell nanoparticles by X-ray photoelectron spectroscopy. *J Phys Chem B*. 2005;109(18):8733-8737. doi:10.1021/jp044322r.
171. Yang D-Q, Gillet J-N, Meunier M, Sacher E. Room temperature oxidation kinetics of Si nanoparticles in air, determined by x-ray photoelectron spectroscopy. *J Appl Phys*. 2005;97(2):24303. doi:10.1063/1.1835566.
172. Mohai M. XPS MultiQuant: Multimodel XPS quantification software. *Surf Interface Anal*. 2004;36(8):828-832. doi:10.1002/sia.1775.
173. Mohai M, Bertóti I. Calculation of overlayer thickness on curved surfaces based on XPS intensities. *Surf Interface Anal*. 2004;36(8):805-808. doi:10.1002/sia.1769.
174. Tougaard S. Surface nanostructure determination by x-ray photoemission spectroscopy peak shape analysis. *J Vac Sci Technol A Vacuum, Surfaces, Film*. 1996;14(3):1415-1423. doi:10.1116/1.579963.

175. Becak DP HN, Shannahan JH, Holland NA, et al. Cardiac Ischemia Reperfusion Injury Following Instillation of 20 nm Citrate-capped Nanosilver. *J Nanomed Nanotechnol*. 2015;S6. doi:10.4172/2157-7439.S6-006.
176. Shannahan JH, Lai X, Ke PC, Podila R, Brown JM, Witzmann FA. Silver Nanoparticle Protein Corona Composition in Cell Culture Media. *PLoS One*. 2013;8(9). doi:10.1371/journal.pone.0074001.
177. Wang X, Ji Z, Chang CH, et al. Use of coated silver nanoparticles to understand the relationship of particle dissolution and bioavailability to cell and lung toxicological potential. *Small*. 2014;10(2):385-398. doi:10.1002/smll.201301597.

VITA

Yung-Chen Wang was born in Taipei, Taiwan. He received his B.S. in Bioengineering from the University of California, Merced in 2012. He received his Ph.D. in Bioengineering from the University of Washington in 2017.